Forced Convective Heat Loss from Cavities of Multi-Megawatt Scale Solar Receivers

Erzwungen-konvektiver Wärmeverlust von Cavities von Solarturmsystemen der Multi-Megawatt-Klasse

Von der Fakultät für Maschinenwesen der
Rheinisch-Westfälischen Technischen Hochschule Aachen
zur Erlangung des akademischen Grades eines
Doktors der Ingenieurwissenschaften
genehmigte Dissertation

vorgelegt von

Silvan Anders Siegrist

Berichter:
Universitätsprofessor Dr.-Ing. Bernhard Hoffschmidt
Universitätsprofessor Dr.-Ing. Thomas Wetzel

Tag der mündlichen Prüfung: 31. Oktober 2018

Dedicated to all those people around the globe
who fight for a bright solar future.

Acknowledgments

The present work was accomplished at the Institute of Solar Research of the German Aerospace Center (DLR) with financial support from the Ministry of Innovation, Science and Research of the State of North Rhine-Westphalia (MIWF NRW), Germany under contract 323-2010-006 (Start-SF). Simulations were performed with computing resources granted by RWTH Aachen University under project rwth0251.

My gratitude goes to Univ.-Prof. Dr.-Ing. Bernhard Hoffschmidt for accepting me as a doctoral student and supervising my work. I am especially thankful for the emphasis he put on the bigger picture which helped me to not spend too much time on irrelevant details and to focus on the thread of the thesis.

I also want to thank Univ.-Prof. Dr.-Ing. Thomas Wetzel for acting as second examiner for my thesis and for letting me present and discuss parts of my research at his lab.

Next, I want to express my gratitude to Dr.-Ing. Hannes Stadler for his day-to-day support during the past 3.5 years. In particular, I thank Hannes for the numerous inspiring discussions and his guidance on thorough scientific research, both improved the present work substantially.

Furthermore, my thanks go to Univ.-Prof. Dr.-Ing. Robert Pitz-Paal and Univ.-Prof. Dr.-Ing. Christian Sattler for giving me very helpful advice during the periodical scientific discussions.

I owe special thanks to Dr.-Ing. Reiner Buck, Peter Schwarzbözl, and Ralf Uhlig for their support for and scientific input to this thesis. I would also like to thank Dr.-Ing. Robert Flesch for the fruitful discussions of his and my work.

The wind tunnel experiments and hence this work would not have been possible without the dedication of my DLR colleagues Dr.-Ing. Nils van Hinsberg and Dr. rer. nat. Stefan Koch in Göttingen as well as the HDG wind tunnel team: Dr.-Ing. Markus Jacobs, Dr. rer. nat. Andreas Benkel, Markus Löhr, and Karsten Steiner.

In addition, I express my thanks to Dr.-Ing. Peter Quadbeck from the Fraunhofer Institute for Manufacturing Technology and Advanced Materials (IFAM) in Dresden. In an act of generosity, he offered me the porous metallic foam that was used in parts of the wind tunnel experiment.

Moreover, I send a big thank you to my colleagues in Spain and around the Mediterranean, who provided me with meteorological data from the enerMENA measurement network.

The manuscript has been considerably improved through the rigorous proofreading by Lisa-Marie Mohr. Additionally, it was always a pleasure to discuss and challenge my thoughts with her. Thank you so much for your commitment!

Finally, it remains to say that the working atmosphere at the Institute of Solar Research has always been highly motivating and great fun. This is first and foremost because of my dear fellow doctoral students and my dear colleagues Arne Tiddens, Daniel Maldonado Quinto, Henrik von Storch, Matthias Offergeld, Raffaele Capuano, Robert Flesch, Sebastian Richter, and Simon Dieckmann.

Abstract

Cavity receivers may increase the efficiency of concentrated solar thermal energy (CSTE) systems because they lose less heat via thermal radiation compared to external receivers. For large CSTE cavity receivers on the multi-megawatt scale, the understanding of forced and mixed convection has not advanced enough to predict the heat loss accurately. Hence, this doctoral thesis focuses on investigating (i) the heat transfer in the forced convection limit ($Ri \ll 1$) for large cavity receivers ($Re \geq 10^6$); (ii) the heat transfer in the mixed convection regime ($Ri \approx 1$) for large cavity receivers ($Gr \geq 10^{10}$, $Re \geq 10^6$); and (iii) possible convective heat loss reduction measures.

The forced convective heat loss from 5 geometrical configurations and 3 reduction measures was measured in a high-pressure wind tunnel. All models were scaled and included the relevant part of the tower. The experiment covered a Reynolds number range of between $1.5 \cdot 10^6$ and $6 \cdot 10^6$, based on the cavity diameter. For the measurements, novel ring-like hot-film sensors were designed and mounted on the inside of the cavity. These sensors were operated with a constant-temperature anemometry (CTA) system.

In addition, a numerical model was validated with a selection of the wind tunnel measurement points. The numerical model was then adapted to the original scale for simulations of multi-megawatt cavity receivers in the mixed convection regime.

The measurements showed that the forced convection from a cavity without reduction measures strongly varies with a factor of up to 6.1 depending on the wind speed and its direction. With a reduction measure a reduction of more than 50% of the forced convective heat loss may be achieved for specific wind directions. Further, it was observed that the forced convection in the cavity is governed by the external flow characteristics in direct vicinity of the aperture. The simulated cases revealed that the forced convective heat loss contributes substantially to the mixed convective heat loss. The mixed convective heat loss results to be of the same order of magnitude as the radiative heat loss. Finally, it was deduced that the optimization of the design of a multi-megawatt CSTE cavity receiver with respect to convective heat loss is possible when a specific site is given and its meteorological boundary conditions are well known.

Zusammenfassung

Cavity-Receiver können den Wirkungsgrad von Solarturmsystemen erhöhen, da sie im Vergleich zu externen Receivern weniger Wärme durch Wärmestrahlung verlieren. Für große Cavity-Receiver von Solarturmsystemen der Multi-Megawatt-Klasse ist das Verständnis der erzwungenen und gemischten Konvektion jedoch noch nicht so weit fortgeschritten, dass der konvektive Wärmeverlust präzise bestimmt werden kann. Darum werden in dieser Doktorarbeit folgende Schwerpunkte untersucht: (i) der Wärmeübergang im erzwungen-konvektiven Extremum ($Ri \ll 1$) für große Cavity-Receiver ($Re \geq 10^6$); (ii) der Wärmeübergang im gemischt-konvektiven Regime ($Ri \approx 1$) für große Cavity-Receiver ($Gr \geq 10^{10}$, $Re \geq 10^6$); und (iii) mögliche Maßnahmen zur Reduktion des konvektiven Wärmeverlusts.

Der erzwungen-konvektive Wärmeverlust von 5 geometrischen Konfigurationen und 3 Reduktionsmaßnahmen wurde in einem Hochdruckwindkanal gemessen. Alle Modelle waren skaliert und enthielten den relevanten Teil des Turms. Das Experiment umfasste Reynoldszahlen von $1.5 \cdot 10^6$ bis $6 \cdot 10^6$, basierend auf dem Durchmesser der Cavity. Für die Messungen wurden neuartige, ringförmige Heißfilmsensoren entwickelt und auf der Innenseite der Cavity angebracht. Diese Sensoren wurden mit einem Constant-Temperature Anemometry (CTA) System betrieben.

Zusätzlich wurde ein numerisches Modell anhand einer Auswahl von Windkanalmesspunkten validiert. Das numerische Modell wurde dann angepasst, um auf der Originalskala Simulationen von Cavity-Receivern der Multi-Megawatt-Klasse im gemischt-konvektiven Regime durchzuführen.

Die Messungen ergaben, dass der erzwungen-konvektive Wärmeverlust einer Cavity ohne Reduktionsmaßnahme je nach Windgeschwindigkeit und -richtung mit einem Faktor von bis zu 6.1 variiert. Mit einer Reduktionsmaßnahme kann der erzwungen-konvektive Wärmeverlust für einzelne Windrichtungen um mehr als 50% reduziert werden. Zudem wurde beobachtet, dass die erzwungene Konvektion in der Cavity durch die externe Strömung direkt außerhalb der Apertur bestimmt wird. Die simulierten Fälle zeigten, dass der erzwungen-konvektive Wärmeverlust maßgeblich zum gemischt-konvektiven Wärmeverlust beiträgt. Der gemischt-konvektive Wärmeverlust ist von gleicher Größenordnung wie der Wärmeverlust durch Strahlung. Abschließend wurde gefolgert, dass eine Designoptimierung eines Cavity-Receivers eines Solarturmsystems der Multi-Megawatt-Klasse hinsichtlich des konvektiven Wärmeverlusts möglich ist, wenn der Standort und dessen meteorologischen Randbedingungen hinreichend bekannt sind.

Contents

Lists

Nomenclature

Roman letters

A	Area, m^2
A	Stagnant zone
A	Constant
a	Exponent
B	Convective zone
B	Constant
C	Concentration ratio
C	Constant
c	Speed of sound, $\mathrm{m\,s^{-1}}$
C_f	Skin friction coefficient
C_1, C_2	Radiation constants
$C_{1\varepsilon}, C_{2\varepsilon}$	Turbulence model constants
c_p	Specific heat capacity, $\mathrm{J\,kg^{-1}\,K^{-1}}$
C_geo	Geometrical constant, $\mathrm{m^{-1}}$
D, d	Diameter, thickness m
E	Electric potential, V
E_b	Hemispherical total emissive power of a blackbody, $\mathrm{W\,m^{-2}}$
$E_{\lambda\mathrm{b}}$	Hemispherical spectral emissive power of a blackbody, $\mathrm{W\,m^{-2}\,rad^{-1}}$
e	Euler's number, 2.718
$\mathbf{F}$	Force vector, N
f	Arbitrary function
f	Frequency, Hz
F_b, F_1, F_2	Blending functions
F_{j-k}	View factor from surface j to k
$g, \mathbf{g}$	Standard gravity, standard gravity vector, 9.81 $\mathrm{m\,s^{-2}}$
Gr	Grashof number
H, h	Height, m
h	Heat transfer coefficient, $\mathrm{W\,m^{-2}\,K^{-1}}$
h	Enthalpy, $\mathrm{J\,kg^{-1}}$
I	Intensity, $\mathrm{W\,m^{-2}}$
J	Radiosity, $\mathrm{W\,m^{-2}}$
k	Turbulence kinetic energy, $\mathrm{m^2\,s^{-2}}$
k	Thermal conductivity, $\mathrm{W\,m^{-1}\,K^{-1}}$
k	Gladstone-Dale constant
k_r	Dimensionless pressure drop
k_1, k_2	Porous permeabilites
L, l	Length, m
m	Exponent
Ma	Mach number
n	Exponent
n	Refractive index
$\mathbf{n}$	surface normal vector
Nu	Nusselt number

Roman letters, continued

P	Power, W
P_k	Turbulence kinetic energy production, $\mathrm{kg\,m^{-1}\,s^{-3}}$
p	Pressure, Pa
p_i	Dimensional parameter
Pe	Peclet number
Pr	Prandtl number
px	Pixel
$\dot{Q}$	Thermal energy flow, W
$\dot{q}$	Thermal energy flux, $\mathrm{W\,m^{-2}}$
R	Electric resistance, Ω
R_{spec}	Specific gas constant, $\mathrm{J\,kg^{-1}\,K^{-1}}$
r	Radius, m
Ra	Rayleigh number
Re	Reynolds number
Ri	Richardson number
S	Net source of power, $\mathrm{W\,m^{-3}}$
$\overline{s_{ij}}$	Time-averaged strain rate, $\mathrm{s^{-1}}$
St	Stanton number
Sr	Strouhal number
T	Temperature, K
t	Time, s
$U, \mathbf{U}$	Velocity, velocity vector, $\mathrm{m\,s^{-1}}$
u_τ	Friction velocity, $\mathrm{m\,s^{-1}}$
X	Ratio
$\mathbf{x}$	Position vector, m
x	Cartesian coordinate, m
y	Cartesian coordinate, m
z	Longitudinal coordinate, m
z_0	Surface roughness, m

Greek letters

α	Wind incident angle, °
α	Thermal diffusivity, $\mathrm{m^2\,s^{-1}}$
α	Absorptivity
α_0	Temperature coefficient of resistance, $\mathrm{K^{-1}}$
β	Coefficient of thermal expansion, $\mathrm{K^{-1}}$
β	Angle between sensor normal and flow direction, °
$\beta, \beta^\star$	Turbulence model constant
γ	Cavity inclination angle, °
γ	Turbulence model constant
δ	Boundary layer thickness, m
δ	Displacement, m
δ	Sensor relative incident angle, °
ε	Turbulence kinetic energy dissipation, $\mathrm{m^2\,s^{-3}}$
ϵ	Emissivity
η	Efficiency
θ_{sun}	sun half-angle, 0.27°
κ	von Karman constant, 0.4
λ	Wavelength, m
μ	Dynamic viscosity, $\mathrm{kg\,s^{-1}\,m^{-1}}$
ν	Kinematic viscosity, $\mathrm{m^2\,s^{-1}}$

Greek letters, continued

ξ	Deflection angle, rad
π_j	Nondimensional parameter
ρ	Density, $\mathrm{kg\,m^{-3}}$
ρ	Reflectivity
σ	Standard deviation, 0.682
σ	Stefan-Boltzmann constant, $5.670 \cdot 10^{-8}\ \mathrm{W\,m^{-2}\,K^{-4}}$
$\sigma_k, \sigma_\varepsilon, \sigma_\omega$	Turbulence model constants
τ	stress tensor, $\mathrm{N\,m^{-2}}$
τ	Transmissivity
Φ	Viscous dissipation function, $\mathrm{W\,m^{-3}}$
Φ	Under-relaxation factor
φ	Angular coordinate, rad
ϕ	Arbitrary quantity
χ	Absolute incident angle, °
ω	Sensor angle, °
ω	Specific turbulence kinetic energy dissipation rate, $\mathrm{s^{-1}}$

Superscripts

$\star$	Nondimensionalized
$+$	Nondimensionalized

Subscripts

aa	Area-averaged
air	Air
ap	Aperture
a, b, c	Indices specific to the Clausing model
back	Back
c	Solar collector
calm	Without wind
Carnot	Carnot
cav	Cavity
cond	Conduction
conv	Convection
cr	Critical
cyl	Cylindrical
eff	Effective
el	Electric
ext	Extended model
film	Film
forc	Forced convection
free	Free convection
front	Frontal winds
H	High
helio	Heliostat
i	Interpolated
in	Inner
insul	Insulation
L	Low
lam	Laminar
lat	Lateral winds
lead	Leads

Subscripts, continued

M	Model scale
max	Maximum
mixed	Mixed convection
O	Original scale
oh	Overheat
opt	Optical
out	Outer
rad	Radiation
rec	Receiver
ref	Reference
rel	Relative
rerad	Reradiation
s	Sensor
s	Stagnant-convective interface
s	System
solar	Solar
supp	Support
surf	Surface
T	Thermal
turb	Turbulent
use	Useful
vis	Viscous
vol	Volumetric
w	Wall
wind	With wind
x	x-Direction
∞	Free-stream

Abbreviations

BOS	Background-oriented schlieren
CFD	Computational fluid dynamics
CRS	Central receiver system
CSP	Concentrated solar power
CSTE	Concentrated solar thermal energy
CTA	Constant-temperature anemometry
DLR	Deutsches Zentrum für Luft- und Raumfahrt / German Aerospace Center
DNI	Direct normal irradiance
HDG	Hochdruckwindkanal Göttingen
IEA-SSPS	International Energy Agency's Small Solar Power System
Insolation	Incoming solar radiation
NREL	National Renewable Energy Laboratory
POM	Polyoxymethylene
PV	Photovoltaics
RANS	Reynolds-averaged Navier-Stokes
SCR	Solar central receiver
SERI	Solar Energy Research Institute (now: NREL)
SIMPLE	Semi-implicit method for pressure-linked equations
SST	Shear stress transport
US DOE	United States Department of Energy

List of Figures

List of Tables

Chapter 1

Introduction

This doctoral thesis documents roughly 3.5 years of my research in the field of *convective heat loss* from large *cavities* of *concentrated solar thermal energy (CSTE) systems*. It comprises seven chapters and an appendix.

This introductory chapter first introduces the organization of this thesis. It then gives the reader a brief overview of CSTE systems. After, it continues to present the literature review in the field of convective heat loss from cavities of CSTE systems. The review covers both experimental and numerical works and highlights the relevant findings of previous research. Finally, the gaps in the state-of-the-art are identified and the 3 goals as well as the scope of this thesis are formulated.

1.1 Organization of this Thesis

In the framework of this, thesis a wind tunnel campaign was planned and executed in order to measure the forced convective heat loss from different solar tower cavity receivers. In this campaign a scaled model was used. A selection of measurement points of this scaled model was also simulated with computational fluid dynamics and pure forced convection. For 3 of the geometrical configurations, additional numerical simulations were also performed on the original scale and with mixed convection.

In this work, after the introductory sections, the reader will then find a chapter on the fundamentals or common ground related to solar central cavity receivers, fluid mechanics, and heat transfer. Then, a third chapter provides the detailed methods of the experimental and numerical investigations. In that chapter, I will also present an adapted hot-film sensor design that is suited to measure the forced convective heat transfer. Next, the results are presented in a chapter with plenty of figures and tables which show the experimental and numerical data from various perspectives. In the consecutive chapter, I highlight and discuss a selection of important findings. The sixth chapter presents the conclusions that are based on the discussion in the previous chapter. Finally, the main body of this thesis is completed with an outlook on possible future research. All the documentation that is relevant to this thesis but did not fit in the main body is placed in the appendix.

At this point, I would like to make a note about the system of notation used in this work: (i) quantities in formulas referring to the wind tunnel scale are marked with subscript M to distinguish them from parameters referring to the original scale which are marked with subscript O; (ii) lists of quantities are indicated by square brackets []; (iii) whenever a list has multiple consecutive elements, an ellipsis $[a, \ldots, b]$ marks the omitted elements and means "and so forth"; and (iv) a specific point in coordinate space is specified within round brackets ().

1.2 Overview of Concentrated Solar Thermal Energy Systems

Concentrated solar thermal energy systems are distinct from photovoltaics (PV) by the way they make use of the radiative energy from the sun. A PV system converts the *insolation* (incoming solar radiation) by means of quantum physics directly to an electric potential and an electric current. In contrast, a CSTE system uses the insolation directly to drive various processes (Winter et al. (1991); Lovegrove and Stein (2012)). These processes can for example be (i) thermodynamic cycles such as Rankine, Brayton or Stirling cycles; (ii) thermochemical cycles with 1 or more reaction steps; and (iii) thermal processes such as high-temperature process heat. The way of generating electricity via thermodynamic cycles is also called *concentrated solar power (CSP)*.

Today, we categorize CSTE systems according to the type of concentration principle into (i) *line focus systems* with parabolic trough and linear Fresnel as the 2 main subcategories, and (ii) *point focus systems* with central receiver and dish as the 2 main subcategories (Stieglitz and Heinzel (2012); Stolten and Scherer (2013)). The *central receiver systems (CRS)*, also called *solar central receiver (SCR) systems* or *solar tower systems*, can further be divided according to their receiver design: *external receiver* and *cavity receiver*. Hereafter, the term CSP is used whenever referral to the specific application of generating electricity is intended, the term CRS is used whenever a referral to this specific concentration technology is intended, and for more general statements, the term CSTE is used.

Research on CSTE systems has emerged in the early 1970s, due to the first oil crisis (Winter et al. (1991); Lovegrove and Stein (2012); Stolten and Scherer (2013)). The focus lay on the centralized production of electricity from solar energy as a replacement for oil-fired power plants. As a result, the first commercial CSP plants were built in the mid 1980s in the Mojave Desert, USA. Most of these systems are still under operation and use the parabolic trough concentration principle to heat a fluid which delivers the heat to a steam Rankine cycle. After commissioning plants with a total capacity of 354 MW, the first commercial CSP deployment effort came to a halt. But, since the mid 2000s, when climate change became an important topic on the political agenda, there has been a resurgence in development of CSP resulting in plant constructions all around the world (SolarPACES (2017)).

Beginning in the 1980s, the central receiver concentration principle was demonstrated in larger field experiments like the International Energy Agency's Small Solar Power Systems (IEA-SSPS) project at the Plataforma Solar de Almería, Spain or Solar One in Daggett (CA), USA. The interested reader is referred to Lovegrove and Stein (2012) for a complete list.

At the end of the year 2017, there was a total name plate capacity of 4.9 GW of CSP plants operational globally (SolarPACES (2017)). Of these power plants, approximately 1/8 are point focus systems and approximately 7/8 are line focus systems. In Fig. 1.2.1, the detailed distribution of the different concentration principles and their subcategories is shown. Of the deployed CRS approximately 6/7 have an external receiver and approximately 1/7 have a cavity receiver (SolarPACES (2017)).

For the lower end of the operating temperature range of CRS, this means from around 500 °C to 700 °C, the external receiver design is commonly assumed to be more efficient, simpler, and cheaper. This temperature range is especially important for the generation of electricity from CSTE, hence the large share of external receivers in CSP plants. However, for higher temperatures the reradiation loss increases with the power to the 4 and

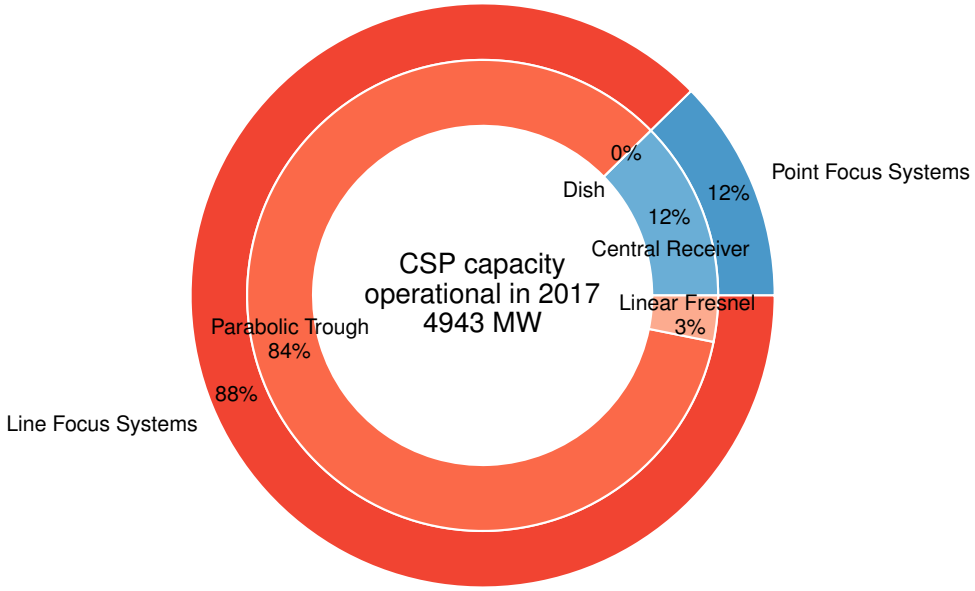

Figure 1.2.1: Global CSP capacity operational at the end of the year 2017 and the shares of the respective concentrating technology (data from SolarPACES (2017)).

consequently, cavity receivers become more efficient because they trap part of the reradiation loss in the cavity (Harris and Lenz (1985); Falcone (1986); Ho (2017)). In Table 1.2.1 a comparison of some of the important aspects regarding the 2 central receiver designs is shown.

Cavities are also well suited for the second category of processes introduced above: the thermochemical processes. Such processes often require very high temperatures up to 1500 °C and often need a reaction chamber that is separated from the ambient air by for example a window (Villafán-Vidales et al. (2017)). This class of processes has shown to be able to split for example water and/or carbon dioxide to hydrogen and oxygen and/or carbon monoxide. Hydrogen and carbon monoxide are also called synthesis gas or syngas. Syngas is a base chemical for all kind of products (fuels, plastics, pharmaceuticals, etc.) of the hydrocarbon industry. Although the world community agreed on capping and reducing the emission of carbon dioxide, it is still increasing worldwide (IPCC (2013)). Thus, the urgency to decarbonize not only the electricity sector, but also other sectors such as consumer goods and transport rises rapidly. As a consequence, thermochemical cycles and the needed high-temperature receivers are gaining increased attention.

Last but not least, cavities are also used for particle receivers. The advantages of a cavity for particle receivers are that it minimizes the loss of particles to the surroundings because the particle stream is protected from the wind and that it maximizes the outlet temperature due to the cavity effect (Ho (2016)).

During the operation of receivers of CSTE systems, be it of cavity or external type, heat is lost mainly due to (i) the partial reflection of the incoming solar radiation on the receiver surface, (ii) the emitted radiation from the hot receiver surfaces to the surroundings, (iii) the conduction to support structures, and (iv) the mixed convection from the hot receiver surfaces to the surroundings. The absolute values of these 4 types of heat loss are changing with different receiver designs and operating parameters. In general, we can simplify this variation due to some important influences as shown in Table 1.2.2.

Some of the influences can be easier quantified than others. For example, the dependency of the reflection and reradiation losses on the surface temperature, surface area, and

Table 1.2.1: Comparison of typical values of selected parameters for external and cavity receiver designs. Data from Falcone (1986) and Ho (2017).

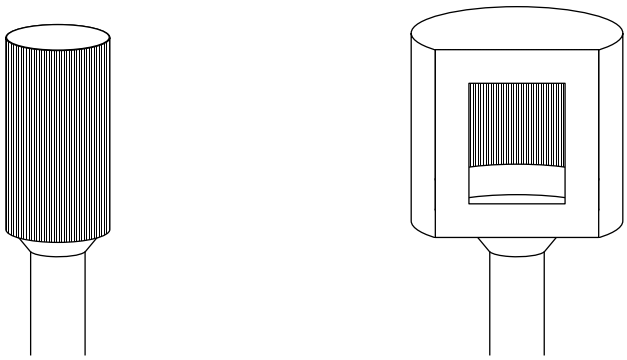

Parameter	External receiver	Cavity receiver
Operating temperature	up to 700 °C	up to 1500 °C
Incident flux	larger†	smaller†
Receiver surface area	smaller†	larger†
Acceptance angle	up to 360°	< 180°
Heliostat field layout	surround field	sector field
Mounting height	lower†	higher†
Heat transfer material	water, molten salts, liquid metals, air	water, molten salts, liquid metals, air, particles

†These values are for a heliostat field of similar power and optical quality.

absorptivity can in many cases be calculated via well known radiative heat transfer methods. The same is true for the dependency of the conduction loss on the surface temperature. In some complicated cases, maybe a numerical method needs to be applied, but a result may still be obtained within reasonable time at a reasonable accuracy. In the case of mixed convective loss there is no easy solution. In the following section, the state-of-knowledge of the convective heat loss from cavities is presented.

1.3 Previous Studies on Convective Heat Loss from Cavity Receivers

The 4 types of heat loss from a CSTE receiver as shown in Table 1.2.2 are applied to the case of a cavity and drawn schematically in Fig. 1.3.1. The reflection and reradiation heat losses are combined into radiative heat loss $\dot{q}_{\mathrm{rad}}$ and indicated by dashed arrows, the conductive heat loss $\dot{q}_{\mathrm{cond}}$ is indicated by straight arrows, and the mixed convective heat loss $\dot{q}_{\mathrm{conv}}$ is indicated by bent arrows. The heat flux available for any subsequent process is indicated by $\dot{q}_{\mathrm{use}}$ with a red arrow.

The mixed convective heat loss from a cavity is a function of the complex flow field inside and outside of the cavity. This complex flow field depends, amongst others, on wind speed and wind direction, which calls for experimental measurements or numerical solutions for each and every relevant combination of receiver design, receiver operating parameters, wind speed, and wind direction (Flesch (2016)). As already reported by Kraabel (1983), the convective heat loss from cavities may be of the same order of magnitude as the radiation heat loss and has therefore to be considered in detail for the design of a cavity

Table 1.2.2: Qualitative behavior of the magnitude of the 4 types of heat loss from a CSTE receiver with respect to a selection of important parameters. A ≈ symbolizes little correlation, a ↑ or ↓ symbolizes a positive or negative correlation, and a ⇑ or ⇓ symbolizes a strong positive or negative correlation.

Parameter	Reflection	Reradiation	Conduction	Mixed convection
Surface temperature	≈	⇑	↑	↑
Surface area	↑	↑	↑	↑
Absorptivity	↓	↑	≈	≈
Incident flux	↑	≈	≈	≈
Wind speed	≈	≈	≈	⇑ or ⇓
Wind direction	≈	≈	≈	⇑ or ⇓

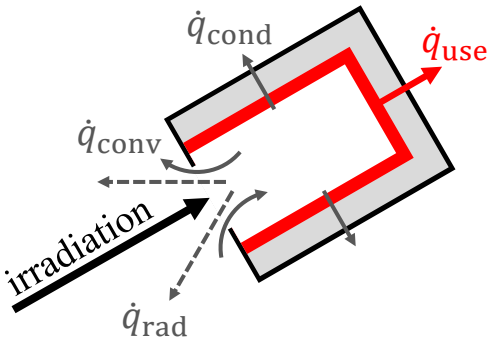

Figure 1.3.1: Schematic drawing of a vertical cross-section through a cavity with the main heat loss modes. Reflection heat loss and reradiation are combined into radiative heat loss indicated by dashed arrows. Indicated by bent arrows is the convective heat loss, by straight arrows the conductive heat loss, and in red the useful heat flux.

receiver. A sufficient explanation and an adequate model for a generalized understanding of convective heat loss have not been published yet. Therefore, research on convective heat loss from CSTE receivers is still an often investigated topic. In the following paragraphs, I summarize the past efforts in the field of mixed, free (or natural), and forced convective heat losses with a focus on CSTE cavity receivers.

1.3.1 First Investigations and the Clausing Model

First investigations on convective heat loss from cavities were done by Tracey et al. (1977), Y. C. Wu and Wen (1978), Eyler (1979) and Clausing (1981).

In the experimental work of Tracey et al. (1977), the convective heat loss could not be measured, but a conservative estimation was done. The heat loss from each of the walls was considered independent of the heat loss from the other walls. Thus, no interactions between the heat losses from different walls were taken into account. The influence of the wind was also neglected. Under these assumptions they found that the convective heat loss has a share of 3% which is roughly equal to the radiative as well as the conductive heat losses.

In their theoretical work, Y. C. Wu and Wen (1978) considered the wind speed, but applied a heat loss correlation to the aperture area, not to the heated walls. They simply added the free and forced convective heat transfer coefficients.

Then, Eyler (1979) investigated the convective heat loss with a 2D numerical model. In

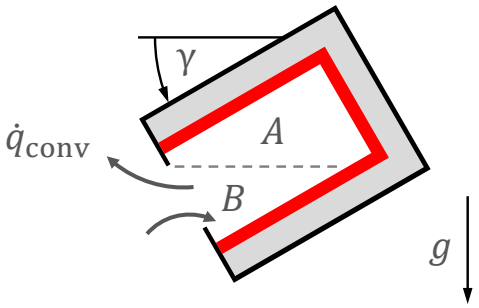

Figure 1.3.2: Stratification and separation of the fluid into a stagnant zone A and a convective zone B. γ is the cavity inclination angle and g is the standard gravity. Surrounding air enters the cavity through the lower part of the aperture and is heated up in the convective zone. Then, the heated air leaves the cavity through the upper part of the aperture.

that work, the wind was also neglected, but it took into account the coupled heat transfer from the different walls. It was found that the fluid stratifies inside the cavity the more the cavity is inclined.

Later, Clausing (1981) developed an analytical model which is applicable to different cavity geometries and also took into account the wind speed. It was reported that the model indicates that the influence of the wind is minimal. Clausing also validated his model in Clausing (1983) with data from Le Quéré et al. (1981) and McMordie (1981). Since this model is the state-of-the-art for the calculation of the convective heat loss from cavities still today, I would like to introduce it here in more detail.

The *Clausing model* is an analytical model based on the assumption that the fluid within the cavity stratifies due to the buoyancy force. Therefore, the fluid in the cavity can be divided into a hot *stagnant (upper) zone* and a cold *convective (lower) zone* as shown in Fig. 1.3.2. It was then further assumed that the convective heat loss from the cavity is dependent on 2 factors: (i) the ability to transfer mass and energy across the aperture and (ii) the ability to heat the fluid inside the cavity. The latter of the 2 factors is the dominant thermal resistance (Clausing (1981)). Consequently, the temperature within the convective zone is only slightly above the ambient air temperature. Clausing represented the heat flows as a thermal resistance network. The convective energy flow $\dot{Q}_{conv}$ out of the cavity can be expressed as

$$\dot{Q}_{conv} = \rho_\infty U_a A_{ap,eff} c_{p,\infty} (T_c - T_\infty) , \tag{1.3.1}$$

where ρ_∞ is the density and $c_{p,\infty}$ the specific heat capacity of the ambient air, U_a the average velocity of the inflow, $A_{ap,eff}$ the area of the aperture through which mass flows in, T_c the temperature of the outflow, and T_∞ the temperature of the ambient air. With these 2 temperatures we can formulate the bulk temperature T_b in the convective zone as

$$T_b = (T_c + T_\infty)/2 . \tag{1.3.2}$$

With L_{ap} as the projected vertical height of the aperture (see Fig. 1.3.3), the fluid accelerates due to the buoyant force to the velocity

$$U_b = \left(g\beta (T_c - T_\infty) L_{ap} \right)^{1/2} , \tag{1.3.3}$$

where g is the standard gravity and β the coefficient of thermal expansion. The velocity in Eq. 1.3.3 may then be combined with the free-stream wind speed U_∞ to the average

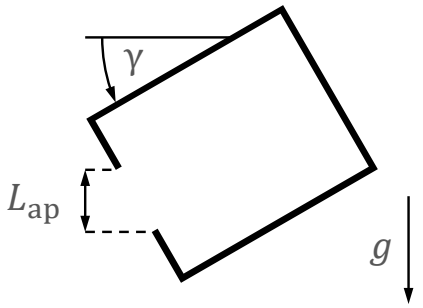

Figure 1.3.3: Definition of the height L_{ap} used in the Clausing model. γ is the cavity inclination angle and g is the standard gravity.

velocity

$$U_a = 0.5\left(U_b^2 + (U_\infty/2)^2\right)^{1/2}. \tag{1.3.4}$$

Balancing the heat loss to the surroundings with the heat added to the fluid from the hot zones inside the cavity gives a solvable system of equations. This heat flow from the hot zones is expressed as

$$\dot{Q}_{conv} = h_w A_w (T_w - T_b) + h_s A_s (T_s - T_b), \tag{1.3.5}$$

where h_w and h_s are the heat transfer coefficients at the hot walls in the convective zone and at the stagnant-convective interface, T_w and T_s are the corresponding temperatures, and A_w and A_s are the corresponding areas.

From the model follows that the more a cavity is facing towards the ground the less will be its convective heat loss.

1.3.2 Experimental Investigations

In the following years, there have been many experimental investigations. In order to have an easy measure for comparison I report the *Grashof number* and the *Reynolds number* of a reference, wherever possible and appropriate. The Grashof number is the ratio of the buoyancy forces to the viscous forces which translates to

$$Gr = \frac{\beta (T_w - T_\infty) L^3 \rho^2 g}{\mu^2}, \tag{1.3.6}$$

where L is a characteristic length, ρ the density, and μ the dynamic viscosity. For the Grashof number, these properties are evaluated at film temperature

$$T_{film} = (T_\infty + T_w)/2. \tag{1.3.7}$$

The Reynolds number is the ratio of the inertial forces to the viscous forces which translates to

$$Re = \frac{\rho U L}{\mu}, \tag{1.3.8}$$

where U is a characteristic velocity. For the Reynolds number, the fluid properties are evaluated at free-stream temperature. By dividing these 2 dimensionless numbers one obtains the Richardson number which is the ratio of the buoyancy forces to the inertial forces

$$Ri = \frac{Gr}{Re^2}. \tag{1.3.9}$$

In 1981, there was a joint workshop of the US DOE, SERI (now NREL), and Sandia National Laboratories titled "Convective Losses from Solar Central Receivers" (Sandia (1981)). The proceedings of this workshop reflect the state-of-knowledge at that time. Many relevant contributions in the field of convective heat loss were presented. For example, Humphrey et al. (1981) performed an experiment of a heated rectangular cavity with flow visualization. They confirmed the stratification reported by Eyler (1979) and later used by Clausing (1981). Another experiment reported in these proceedings was the one of Faust et al. (1981). They investigated a 3-cavity model with a tower in an open wind tunnel. The Grashof number was approximately in the range of between $2.6 \cdot 10^6$ and $5.8 \cdot 10^6$. They found that for higher wind speeds the heat loss varies with the incident angle and peaks at 90°. Though one should keep in mind that the Reynolds numbers were at maximum $2.7 \cdot 10^3$. Further, Le Quéré et al. (1981) presented the experiment that was already mentioned earlier while speaking about the validation of the Clausing model. In that experiment a cubic cavity of 0.6 m edge length was used to study free convection only. They showed that the incoming flow becomes turbulent before reaching the back wall.

Kraabel (1983) reported measurements for pure free convection from a cube with an edge length of 2.2 m with 1 side open to the surroundings. In the experiment Grashof numbers of up to $3.1 \cdot 10^{10}$ were reached when the fluid properties are evaluated based on the film temperature. One of the results was a well fitting correlation for the free convective heat loss

$$Nu_{\text{free}} = 0.088 Gr^{1/3} \left(T_{\text{w}}/T_{\infty}\right)^{0.18} , \tag{1.3.10}$$

where Gr is evaluated based on the ambient temperature. Accidentally, the cavity was exposed to wind speeds up to a few meters per second. But, this wind did not have a significant impact on the measurements.

McMordie (1984) measured the mixed convective heat loss from a cavity receiver on top of a 61 m tower. The absorber panel had a height of 3.5 m. The standard deviation of the results was approximately 30%. Because there was no distinguishable effect of the wind speed, it was concluded that the effects of wind speed were smaller than the measurement uncertainty. The Grashof number for this experiment was $2.7 \cdot 10^{11}$ and the Reynolds numbers ranged from $1.4 \cdot 10^5$ to $7.1 \cdot 10^5$.

Siebers and Kraabel (1984) suggested a method for an estimation of the convective heat loss from external and cavity type receivers. They recommended to add the forced and free convective heat transfer coefficients h_{forc} and h_{free} raised to an exponent a to obtain the heat transfer coefficient for mixed convection

$$h_{\text{mixed}} = \left(h_{\text{forc}}^a + h_{\text{free}}^a\right)^{1/a} , \tag{1.3.11}$$

where $a \approx 3.2$ in the case of an external cylinder and $a \approx 1$ in the case of a cavity. Further, they combined previous experimental data to obtain a general heat loss correlation for external cylinders. They stated that the general heat loss mechanisms of a heated external cylinder and a heated cavity are very similar, except when it comes to the influence of the geometry on the flow pattern. The cavity geometry generates complex flow structures in the cavity, and hence adds complexity to the heat transfer. They also emphasized the finding by Mirenayat (1981) and Kraabel (1983) that the heat transfer coefficient due to free convection is independent of the length scale of the cavity. In addition, it was suggested that the heat transfer coefficient is sufficiently independent of specific geometry and thus Eq. 1.3.10 should be valid for cavity receivers consisting of combinations of simple geometries. Further, they noted that there was contradictory evidence in literature whether wind influences the convective heat loss or not. Since there was no deeper knowledge at

that point in time on this aspect, they treated the forced convective heat loss as the heat loss caused by a flat plate of the size of the aperture at the temperature of the inner cavity walls. Last but not least, they stated that there is a need for correlations for forced convective heat loss from a cavity.

Hess and Henze (1984) used a water tank to increase the Grashof number. Due to a transparent side of the cavity it was possible to investigate flow patterns within the cavity. They reported amongst other points a stable stratification of the stagnant zone and a reduction in heat loss by reducing the size of the aperture.

Next to increasing the density and changing the fluid properties, as for example in a water tank, one could additionally adjust the temperature and the pressure. In this aspect, cryogenic wind tunnels are very well suited for measurements of convective heat loss in large Grashof number and large Reynolds number experiments. This was demonstrated by Clausing (1979). Depending on the cryogenic facility one can obtain Reynolds numbers of about 1 order of magnitude higher and Grashof numbers of more than 2 orders of magnitude higher compared to conventional facilities. This technique was used in Clausing et al. (1987) for a study on the free convection from cavities with Grashof numbers of up to about $2.1 \cdot 10^{10}$. Different aperture sizes and geometries were tested. One of their findings was that the stagnant-convective interface is nearly adiabatic. In a subsequent study in the same cryogenic wind tunnel, Clausing et al. (1989) measured the mixed convective heat loss for Richardson numbers of between 0.01 and ∞. From that experiment it was concluded that for $Ri < 0.04$ the hot air in the stagnant zone is mixed with the cold entering air and leads to substantial increase in heat loss. They also found that moderate wind speeds may reduce the mixed convective heat loss.

Pavlovic and Penot (1991) performed measurements for different aperture configurations of a cubic cavity with 0.6 m height. These experiments were performed in a Richardson number range from 0.71 to 19 and showed a strong influence of the forced convection.

In 2014, W. Wu et al. (2014) investigated the influence of rotation on the convection from a rotating cavity. They concluded that the rotation has a very small effect on the convective heat loss. The Grashof numbers ranged from $1.0 \cdot 10^7$ to $2.3 \cdot 10^7$.

In Flesch et al. (2015) a recent experiment is presented which is also described in a doctoral thesis (Flesch (2016)). A cylindrical cavity with an inner diameter of 0.66 m and a depth of 0.73 m was used to measure the free and mixed convective heat losses in a cryogenic wind tunnel. The Grashof number was about $3.9 \cdot 10^{10}$ and the Reynolds numbers were varied in the range of 0 to $5.2 \cdot 10^5$. By using a similitude approach, the results of this experiment can be used for cavities with a diameter of up to 2.4 m. The cavity was inclined in 4 steps from the horizon to the ground and rotated in 6 steps from frontal to backward winds. The main finding was that wind has a substantial influence on the size of the stagnation zone, both for increasing and reducing it. Consequently, the wind may enhance or reduce the heat transfer significantly. Based on the measurements an extension to the Clausing model was proposed which incorporates the forced convection more appropriately. In this *extended Clausing model*, the stagnant-convective interface is allowed to displace upwards depending on the wind direction and speed. This vertical displacement δ_{ext} is depicted in Fig. 1.3.4 and defined as

$$\delta_{\text{ext}} = \delta_{\text{front}} F_{\text{b}} + (1 - F_{\text{b}}) \delta_{\text{lat}}, \tag{1.3.12}$$

where δ_{front} is the displacement due to frontal winds, δ_{lat} is the displacement due to lateral winds, and F_{b} is a blending function defined as

$$F_{\text{b}}(\chi) = 0.5 + 0.5 \tanh\left(\frac{75° - \chi}{5°}\right), \tag{1.3.13}$$

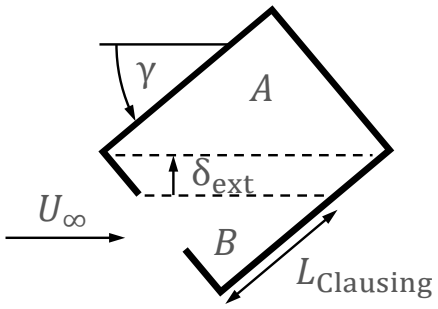

Figure 1.3.4: Vertical displacement δ_{ext} of the stagnant-convective interface in a cavity. γ is the cavity inclination angle and L_{Clausing} is the length along the cavity walls from the bottom to the stagnant zone. With increasing wind speed U_∞ the stagnant zone A shrinks and the convective zone B extends upwards. This exposes more of the hot walls to the moving fluid in the convective zone.

where χ is the absolute incident angle as defined in Fig. 3.2.1b. The displacements due to frontal and lateral winds are calculated via

$$\delta_{\text{front}} = \max\left(0, \left(C_{\text{front}} U_\infty - L_{\text{Clausing}}\right) \sin(\gamma)\right) \tag{1.3.14}$$

$$\delta_{\text{lat}} = \max\left(\delta_{\text{lat},z}, \delta_{\text{lat},r}\right), \tag{1.3.15}$$

where the contribution $\delta_{\text{lat},z}$ in cylinder axis direction and the contribution $\delta_{\text{lat},r}$ normal to the cylinder axis are

$$\delta_{\text{lat},z} = \max\left(0, \sin(\gamma)\, C_{\text{lat},z} U_\infty - \cos(\gamma)\, d_{\text{ap}}/2\right) \tag{1.3.16}$$

$$\delta_{\text{lat},r} = \max\left(0, \cos(\gamma)\left(C_{\text{lat},r} U_\infty - d_{\text{ap}}/2\right)\right), \tag{1.3.17}$$

where γ is the cavity inclination angle as defined in Fig. 3.2.1b, L_{Clausing} is the length along the cavity walls from the bottom to the stagnant zone, and C_{front}, $C_{\text{lat},z}$, and $C_{\text{lat},r}$ are empirical constants found to equal $C_i = 0.1\,\text{s}$. The extended Clausing model was found by Flesch (2016) to fit the experimental data better than the Clausing model.

So far, the mentioned contributions were intended to foster the understanding of the convective heat loss from large cavities which are mounted on top of a solar tower and receive the energy from many heliostats. There has also been much research that used cavities in CSTE dish systems. These receivers are typically sized 2 orders of magnitude smaller than their counterparts in tower systems. Thus, in the following paragraphs I mention only those that may also be relevant to larger cavities.

One relevant study was performed by Stine and McDonald (1989). They reported measurements of free convective heat loss from a cylindrical cavity of 0.66 m in diameter with a conical end section. The Grashof number was about $2{\cdot}10^9$. They found a strong dependency of the heat loss on the aperture size. They also found that this effect is more pronounced for smaller apertures. For completely inclined cavities facing the ground, they did not measure a relevant heat loss. This was in good agreement with previous investigations. The same cavity was used in a series of experiments reported by Ma (1993). Additionally, the influence of wind speed and wind direction were investigated. It was found that higher wind speeds increase the mixed convective heat loss throughout all measured sets of parameters. Therefore, it was concluded that the forced convection enhances the mixed convection. And hence, the free convection and forced convection contributions may be summed according

to a correlation which is different for head-on or side-on wind. The Grashof number was the same as in Stine and McDonald (1989) and the Reynolds numbers ranged from 0 to $2.4 \cdot 10^5$.

Leibfried and Ortjohann (1995) investigated the mixed convective heat loss from a spherical and a hemispherical cavity with diameters of 0.4 m. They performed measurements and visualizations for Grashof numbers of between $2.4 \cdot 10^8$ and $4.4 \cdot 10^8$. The influence of wind was investigated roughly and only for an upward-facing cavity. They found that wind reduces the heat loss under these circumstances.

Taumoefolau et al. (2004) measured the free convective heat loss from a cylindrical cavity receiver with a diameter of 0.07 m. They found that the Clausing model (Clausing (1981)) fits the data well. In addition, they also visualized the flow out of the cavity by the synthetic schlieren imaging method. The Grashof numbers were approximately $2 \cdot 10^6$.

J. K. Kim et al. (2007) reported an experiment with a cubic cavity with an edge length of 0.4 m and different inclination angles. The Richardson numbers ranged from 0.025 to ∞. It was found that wind influences the heat loss only for cavities that are inclined more than 20°.

Prakash et al. (2009) performed measurements of the free and mixed convective heat losses. The cavity studied was a cylinder of 0.3 m in diameter and 0.5 m depth. In general, the measured convective heat losses with wind were substantially higher than without wind. The Grashof numbers ranged in between $9.2 \cdot 10^7$ and $1.4 \cdot 10^8$ and the highest Reynolds number was $5.4 \cdot 10^4$.

1.3.3 Numerical Investigations

Next to the wealth of experimental investigations, there have been a comparable number of numerical investigations, especially in more recent years. This might be due to 2 effects: (i) the high costs and complexity of adequate experimental setups and (ii) the ever increasing power, accuracy, and usability of computational fluid dynamics (CFD). Possibly the earliest CFD study on the free convective heat loss from a cavity was the one by Eyler (1979). In that study, it was shown that the fluid stratifies in the upper part of the cavity, as depicted in Fig. 1.3.2. Very similar findings were reproduced with an adapted numerical code for buoyant flows with mixed convection which was reported in Humphrey et al. (1982).

A research group at the Australian National University has published several studies on the convective heat loss from dish cavity receivers (Paitoonsurikarn and Lovegrove (2002); Paitoonsurikarn et al. (2004); Paitoonsurikarn et al. (2011)). The modeled geometries were cylindrical or conical cavities with diameters of between 0.07 m and 0.66 m. They investigated free convection with a Grashof number of about $1 \cdot 10^9$ (Paitoonsurikarn and Lovegrove (2002); Paitoonsurikarn et al. (2011)) and found good agreement with existing correlations and experiments. Nonetheless, they proposed a new correlation which is based on an ensemble length scale taking into account the geometry and inclination of the cavity. They also investigated forced convection (Paitoonsurikarn et al. (2004)) and found that the forced convection dominates the heat loss for $Ri < 0.02$. Richardson numbers ranged from $1 \cdot 10^{-3}$ to ∞.

Chen et al. (2006) simulated a cubic cavity with edge lengths ranging from 0.4 m to 2 m. The calculations were on pure free convection with $2 \cdot 10^8 < Gr < 1.5 \cdot 10^{10}$, but they added an estimation based on the Clausing model which suggests that the external wind speed exceeds the wind speed in the cavity caused by free convection and thus, the forced convection will have a considerable impact.

Reducing the convection from cavities with solid particles is especially important because with each volume of hot air also some particles may be lost. Tan et al. (2009) studied

this for a cavity with a width of 2 m and a height of 3 m. Richardson numbers lay in the range of 0.2 to ∞. Their conclusions were that wind reduces the cavity efficiency drastically and that under special wind conditions an aerowindow is formed and increases the cavity efficiency.

Fang et al. (2011) analyzed a cavity of approximately 8 m in height on a tower at 100 m. With the considered wind speed this gives $0.3 < Ri < \infty$. Their results showed that the wind has a substantial effect and heat loss peaks when the wind comes laterally from about 60° to 90°.

J. S. Kim et al. (2012) and Liovic et al. (2014) took wind into account and found that the convective heat loss from their hexagonal cavity more than tripled under certain wind conditions. The Richardson numbers were in the range of between 0.2 to ∞.

Xiao et al. (2012) investigated a dish cavity with an inner diameter of 0.07 m and considered also the wind speed. Richardson numbers ranged from 0.007 to ∞. They found a strong influence of the wind speed and wind direction for almost all combinations.

A simple cylindrical geometry with a diameter of 0.1 m was used in the numerical study of S.-Y. Wu et al. (2014). They included radiation, conduction, and free convection in their 3D model. They applied a uniform and constant flux at the heated walls which matched well with experimental values. The related Grashof numbers ranged from $6.1 \cdot 10^6$ to $8.4 \cdot 10^6$.

Also in 2014, Flesch et al. (2014) published a numerical analysis of the influence of inclination angle, wind speed, and wind direction on the convective heat loss of cavity receivers. They concluded that wind generally reduces the stagnant zone and therefore increases the convective heat loss. But, for some measurement points with wind the convective heat loss is reduced to values below the free convective heat loss. Their numerical model was later validated with the experiments of Flesch et al. (2015) which was published in Flesch (2016) and Flesch et al. (2016). It was found that the numerical model underpredicts the convective heat loss by approximately 20%. The numerical study was done with the same Grashof number of about $3.9 \cdot 10^{10}$ and the same Reynolds numbers in the range of 0 to $5.2 \cdot 10^5$.

Yuan et al. (2015) compared 2 commercial CFD software and came to the conclusion that they underestimate the free convective heat loss by 30% to 45% when validated against experimental values. The corresponding Grashof numbers were $1.2 \cdot 10^6$ up to $3.1 \cdot 10^{10}$.

J. K. Kim et al. (2015) simulated 4 types of both external and cavity receivers under the influence of wind. Based on their results they proposed a single correlation for the fraction of convective heat loss for all receiver types. Considering the diversity of the different receivers being put into 1 single equation, they concluded that the correlation matches experimental and numerical values well. The Richardson numbers simulated were in the range of 0.17 to 63.

Reddy et al. (2016) studied a hemispherical dish cavity with a diameter of 0.3 m. They also included wind speed and direction and designed the simulation to be in the Richardson number range of 0.02 to ∞. In almost all conditions, the wind had a strong enhancing effect on the mixed convective heat loss. They also showed that by reducing the aperture the convective heat loss may be reduced, but the wind has still a comparable impact.

1.3.4 Reduction Measures

In addition to the contributions that tried to shed light on the complicated topic of convection mechanisms, there have been a handful of publications that dealt with the reduction of the convective heat loss. In Uhlig et al. (2014) many ideas are given, but only the segmented full window was closer investigated. Such a full window would reduce the convective heat loss completely. Unfortunately, it is at the moment hardly possible to manufacture trans-

parent materials in the size of several tens of meters to cover a large cavity which can also withstand the operating conditions and thermal stresses of large scale cavities. But, as shown by Flesch et al. (2016) a partial window on the upper side could reduce the convective heat loss already by 10% to 30%.

Two of the previously mentioned papers (Tan et al. (2009); Flesch et al. (2016)) included a reduction measure called aerowindow. It was shown that if the free or machine-induced wind approaches the cavity under certain conditions the mixed convective heat loss may be reduced substantially. A reduction potential of up to 50% was reported.

Next to an aerowindow, Hughes et al. (2016) proposed an adapted temperature distribution with lower temperatures near the aperture. Such a temperature distribution could for example be reached by having the inlet of the cold fluid near the aperture. The hot air leaving the cavity will heat the cold fluid and the convective heat loss is recuperated partially.

1.3.5 Scientific Review Articles

In 1987, Boehm compiled all available data concerning measurements of convective heat loss from receivers in a publication (Boehm (1987)). Next to the aforementioned studies, he also included measurements from the cavity of the IEA-SSPS project. These data showed a significant increase of convective heat loss with increased wind speed.

An overview of the correlations and models existing in 1995 for the calculation of convective heat loss is given in McDonald (1995). Of great interest is the comparison of the performance of the different models.

An overview of the state-of-knowledge in 2010 was given by S.-Y. Wu et al. (2010). That contribution documented the different efforts to find a more applicable and unified model for the convective heat loss from cavity receivers. Unfortunately, no information is given on the performance of each of the correlations.

In the doctoral thesis of Flesch (2016) the reader will find an excellent overview of the research concerning convective heat loss from cavities up to 2016 (in English there are short versions in Flesch et al. (2014) and Flesch et al. (2015)).

1.3.6 Summary of the State-Of-The-Art

The literature reviewed in the previous sections is summarized in Fig. 1.3.5. The figure shows both numerical (orange with italic font) and experimental works (blue with roman font) on a Grashof number versus Reynolds number plot. The data which are added in the framework of this thesis are shown in dark blue and dark orange (Sie18b, Sie18c). Sie18c refers to those contents of this thesis that have not been published previously. To indicate equality of the buoyant and inertial forces ($Ri = 1$) a dark grey diagonal line is shown together with a grey band which represents $0.1 < Ri < 10$. The typical operating regime of large central receiver systems is indicated by the red horizontal band. Contributions which were performed in the pure free or pure forced convection regime are plotted on 2 separate axes to the left and to the bottom, respectively. It is emphasized that the straight lines only represent the shortest connection between the minima of Gr and Re and their respective maxima, for the detailed Gr-Re-regime, the reader is referred to the sources. The sources are indicated by the first 3 letters of the author's last name and the 2 last digits of the year of publication.

It can be noted that few research has been done for $Gr > 10^{10}$, especially in the cases where $Re^2 \geq 10^{12}$.

The literature review presented here is based on a selection of the relevant investigations during the past 40 years of cavity convection research. I tried to cover both the

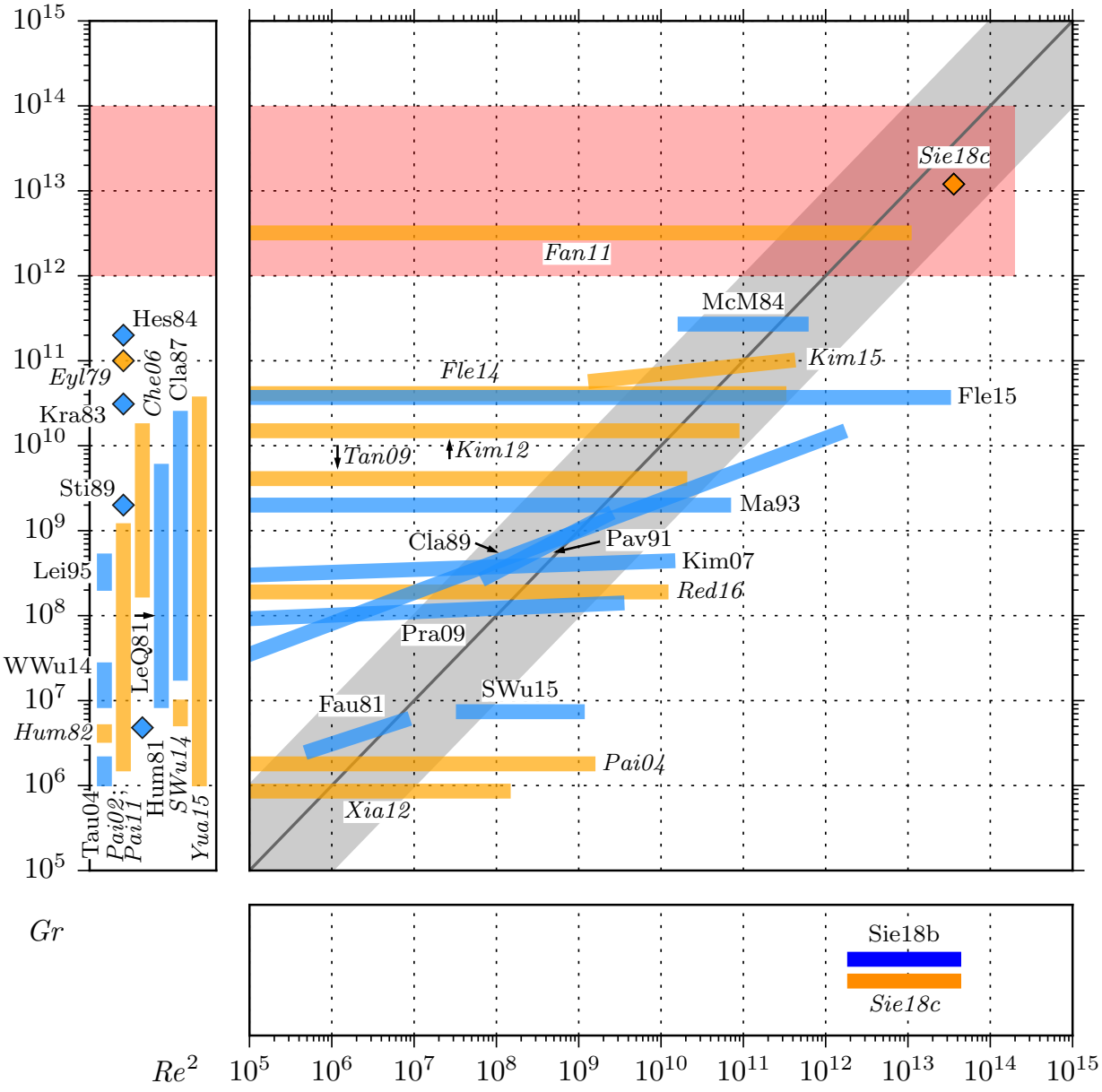

Figure 1.3.5: Overview of the literature for convective heat loss from cavities. Contributions which were performed in the pure free or pure forced convection regime are plotted on 2 separate axes to the left and to the bottom, respectively. Blue with roman font are experiments, orange with italic font are numerical simulations, and the new data contributed in the framework of this thesis are marked with dark blue and dark orange (Sie18b, Sie18c). The dark grey diagonal line indicates $Ri = 1$ and the grey band indicates $0.1 < Ri < 10$. The red horizontal band represents the typical operating regime of large central receiver systems. The 5 characters refer to the first 3 letters of the author's last name and the 2 last numbers of the year of publication.

breadth and depth which represents today's state-of-knowledge adequately. To emphasize the 2 flow regimes where the free convection and the forced convection have negligible influence on each other the terms *forced convection limit* ($Ri \ll 1$) and *free convection limit* ($Ri \gg 1$) are used. The following points are a short aggregation of the findings in the past research efforts:

- There has been a wealth of theoretical, experimental, and numerical research on convective heat loss.
- The understanding of free (or natural) convective heat loss has advanced so far that one can predict accurately the convective heat loss from cavity receivers with different geometry at the free convection limit ($Ri \gg 1$).
- The understanding of forced convective heat loss for complicated geometries like cavities has not advanced enough to reliably predict the convective heat loss from cavity receivers at the forced convection limit ($Ri \ll 1$).
- The understanding of mixed (combined) convective heat loss at $Ri \approx 1$ and $Gr < 10^{10}$ (which represent small cavities, such as for dishes) has advanced enough to predict the mixed convective heat loss from cavities with a variety of geometries.
- The understanding of mixed (combined) convective heat loss at $Ri \approx 1$ and $Gr \geq 10^{10}$ (which represent large cavities, such as on towers) has not advanced enough to predict the mixed convective heat loss from cavities satisfactorily.
- So far, the understanding of the mixed convective heat loss is that wind may reduce the mixed convective heat loss from cavities, even below free convection values, when it forms an aerowindow. In all other cases, the wind enhances the mixed convective heat loss. Both applies to flows with $Ri < 1$.
- Only very few researchers have investigated the cavity mounted on a tower. Thus, the effects of the tower on the convective heat loss are mostly unknown.
- Many active and passive reduction measures have been proposed. But only a few of them were investigated in detail.

1.4 Goals and Scope of this Work

As pointed out by Siebers and Kraabel (1984), and this is still true today, there are very little data on the forced convection limit ($Ri \ll 1$) for cavities. Additionally, as shown in the presented literature review in the previous sections, data on the mixed convection for very large Reynolds and Grashof numbers are also rare. Both points can also be seen in Fig. 1.3.5. And last but not least, there is still a lack of knowledge on how to reduce the convective heat loss effectively. Therefore, I have formulated the following 3 goals for this work :

1. To shed light on the heat transfer in the forced convection limit ($Ri \ll 1$) for large scale cavities ($Re \geq 10^6$).
2. To enhance the understanding of the heat transfer in the mixed convection regime ($Ri \approx 1$) for large scale cavities ($Gr \geq 10^{10}$, $Re \geq 10^6$).
3. To analyze possible convective heat loss reduction measures.

These 3 goals have been addressed in this work by:

- Wind tunnel measurements in order to determine the convective heat loss characteristics in the limit of pure forced convection ($Ri \ll 1$). This has been done for models of solar central cavity receivers including the relevant part of the tower. The measured models had 3 different cavity inclinations at 1 aperture opening ratio and 3 different aperture opening ratios at 1 cavity inclination.
- Wind tunnel measurements of the forced convective heat loss of 3 passive reduction measures in the same wind tunnel campaign. The 3 selected reduction measures were a solid porch, a porous porch, and an aerodynamic optimized porch.
- Numerical simulations of the wind tunnel models. This has been done for a small selection of the wind tunnel measurement points in order to validate the numerical model in the forced convection limit ($Ri \ll 1$).
- Numerical simulations of the original scale ($Gr \geq 10^{10}$, $Re \geq 10^{6}$) in the mixed convection regime ($Ri \approx 1$). This has been done for 3 cavity inclinations at 1 aperture opening ratio.

Chapter 2

Fundamentals

In this chapter, the common ground for CSTE systems is set by introducing the relevant principles and equations from physics and mathematics such as the maximum theoretical system efficiency, fluid mechanics, heat transfer, dimensional analysis, boundary layer theory, Reynolds analogy and computational fluid dynamics. Even though the reader might be familiar with all of these topics, it is recommended to at least quickly scan through this chapter to get acquainted to the notation introduced here and used in the later chapters.

2.1 Maximum Theoretical System Efficiency

Duffie and Beckman (2013) give a good introduction into the field of concentrated solar thermal energy engineering. In the following, I will reproduce from their book the most important topics relevant to central receiver systems and add to it from other relevant sources. By using a field of heliostats we are able to collect the incoming solar radiation and redirect it on a receiver. By redirecting all of the insolation on to a common area on the receiver we overlay the solar radiation from each heliostat. Hereby, the solar energy is concentrated. This concentration can be given as a *concentration ratio C* based on the area of all heliostats A_{helio} and the area of the receiver A_{rec}

$$C = \frac{A_{\text{helio}}}{A_{\text{rec}}}. \tag{2.1.1}$$

Through the combination of the second law of thermodynamics and geometrical considerations, we can formulate the upper limit of the concentration ratio in the case of point focus systems as

$$C_{\text{max}} = \frac{1}{\sin(\theta_{\text{sun}})^2}, \tag{2.1.2}$$

which gives roughly 45000 in the case of a sun half-angle θ_{sun} of 0.27°.

Following the derivation of Fletcher and Moen (1977), we continue to find the *maximum theoretical system efficiency* for a CSTE system. The idealized efficiency to generate useful work from a heat source is known as the *Carnot efficiency*

$$\eta_{\text{Carnot}} = \frac{T_{\text{H}} - T_{\text{L}}}{T_{\text{H}}}, \tag{2.1.3}$$

where T_{H} is the temperature of the heat source and T_{L} the temperature of the heat sink. The system efficiency is then calculated as the product of the Carnot efficiency and the *solar collection efficiency*

$$\eta_{\text{s}} = \eta_{\text{Carnot}} \eta_{\text{c}}. \tag{2.1.4}$$

The energy that is absorbed by the receiver is

$$\dot{Q}_{\text{rec}} = I A_{\text{helio}} \eta_{\text{opt}} \alpha, \tag{2.1.5}$$

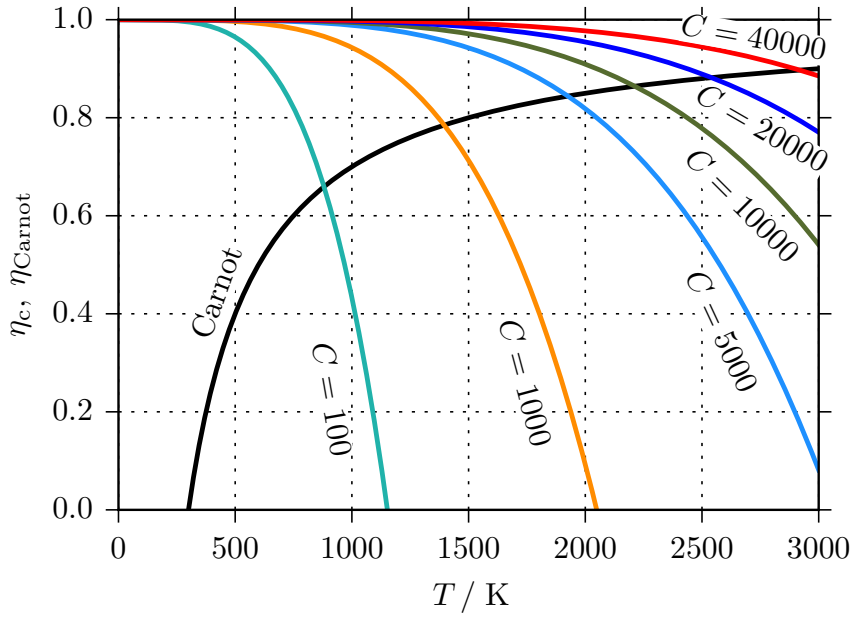

Figure 2.1.1: Idealized solar collection efficiency η_c and Carnot efficiency η_{Carnot} versus temperature T. C indicates the concentration ratio. Assumptions: $I = 1000\,\mathrm{W\,m^{-2}}$, $T_L = 300\,\mathrm{K}$.

where I is the intensity of the solar radiation, η_{opt} the optical efficiency of the heliostat field, and α the effective absorptivity of the receiver. By subtracting the reemitted radiative heat loss $A_{rec}\epsilon\sigma T_H^4$, the convective heat loss $hA_{rec}(T_H - T_L)$, and the conductive heat loss $k_{insul}A_{rec}(T_H - T_L)/d_{insul}$ and dividing all terms by the incoming solar energy we obtain the solar collection efficiency

$$\eta_c = \frac{\overbrace{IA_{helio}\eta_{opt}\alpha}^{\dot{Q}_{rec}} - \overbrace{A_{rec}\epsilon\sigma T_H^4}^{\dot{Q}_{rerad}} - \overbrace{hA_{rec}(T_H - T_L)}^{\dot{Q}_{conv}} - \overbrace{k_{insul}A_{rec}(T_H - T_L)/d_{insul}}^{\dot{Q}_{cond}}}{\underbrace{IA_{helio}}_{\dot{Q}_{solar}}}, \tag{2.1.6}$$

where ϵ is the effective emissivity of the receiver, σ the Stefan-Boltzmann constant, h the heat transfer coefficient from the hot receiver walls to the surroundings, and k_{insul} and d_{insul} the effective thermal conductivity and thickness of the insulation, respectively. For the further analysis we assume that the receiver is perfectly insulated and no heat is lost by convection. We then set $\eta_{opt} = \alpha = \epsilon = 1$, divide all terms by A_{rec}, and use the concentration ratio instead of the areas. This gives us an idealized solar collection efficiency of

$$\eta_c = \frac{IC - \sigma T_H^4}{IC}. \tag{2.1.7}$$

It becomes clear that the solar collection efficiency reduces with the fourth order proportional to the receiver temperature. This relation is shown together with the Carnot efficiency in Fig. 2.1.1.

The maximum theoretical efficiency of the conversion of solar energy to useful energy can then be obtained by Eq. 2.1.4 which gives

$$\eta_s = \left(\frac{T_H - T_L}{T_H}\right)\left(\frac{IC - \sigma T_H^4}{IC}\right). \tag{2.1.8}$$

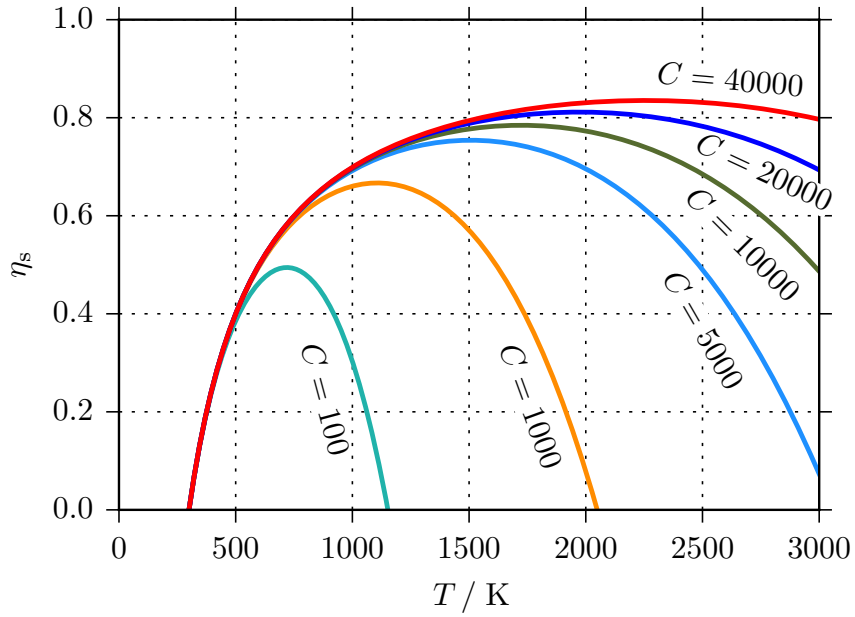

Figure 2.1.2: Maximum theoretical system efficiency η_s of the conversion of solar thermal energy to useful energy. To reach the optimum system efficiency for an increased temperature T it is required to increase the concentration ratio C, too. Assumptions: $I = 1000\,\mathrm{W\,m^{-2}}$, $T_L = 300\,\mathrm{K}$.

This maximum theoretical system efficiency is plotted in Fig. 2.1.2 for different concentration ratios. From this figure we can deduce that we need to increase the concentration ratio if we want to reach higher temperatures in our downstream process. An interesting fact is that this applies universally to all mentioned solar processes in Section 1.2, such as thermodynamic, thermochemical or thermal processes.

2.2 Fluid Dynamics

We are neither able to create nor destroy matter or energy and except for quantum physics we are not able to convert matter and energy into each other. Consequently, we have to balance mass, momentum, thermal energy, species, and many other quantities which can take the form of scalars, vectors or tensors. In general, we can balance the relevant quantities in a fluid control volume as shown in the following equation

$$\begin{bmatrix} \text{rate of} \\ \text{accumulation} \end{bmatrix} = \begin{bmatrix} \text{rate of} \\ \text{advection} \end{bmatrix} + \begin{bmatrix} \text{rate of} \\ \text{diffusion} \end{bmatrix} + \begin{bmatrix} \text{rate of} \\ \text{conversion} \end{bmatrix}. \tag{2.2.1}$$

All of the terms can be positive, which means they add some amount of the quantity to the control volume, or negative which means they subtract some amount of the quantity from the control volume.

Normally, we start with the easiest of these balances, the *conservation of mass* or *continuity equation*. Mass is not transported by diffusion and cannot be created or destroyed. Therefore, the last 2 terms in Eq. 2.2.1 cancel and we end up with the partial differential equation in conservation form

$$\frac{\partial}{\partial t}\rho = -\nabla \cdot (\rho \mathbf{U}), \tag{2.2.2}$$

where ρ is the density of the fluid and $\mathbf{U}$ the velocity vector field.

The second balance we need to solve for real flows is the *conservation of momentum* which can be derived from Newton's second law of motion. In its shortest form it is

$$\rho \frac{D}{Dt}\mathbf{U} = \mathbf{F}_{\text{surf}} + \mathbf{F}_{\text{vol}}\,, \tag{2.2.3}$$

where $D/(Dt)$ is the total derivative, $\mathbf{F}_{\text{surf}}$ the forces acting on surfaces, and $\mathbf{F}_{\text{vol}}$ the forces acting on the volume. When explicitly writing the surface forces due to pressure p and shear stress tensor τ the equation expands to

$$\rho \frac{D}{Dt}\mathbf{U} = -\nabla p + \nabla \cdot \tau + \mathbf{F}_{\text{vol}}\,. \tag{2.2.4}$$

By further introducing the relation between the shear stress and strain rate and using the Stokes hypothesis we finally end up with the *Navier-Stokes equation*

$$\rho \frac{D}{Dt}\mathbf{U} = -\nabla p + \mu \mathbf{\Delta U} + \mathbf{F}_{\text{vol}}\,, \tag{2.2.5}$$

where μ is the dynamic viscosity. In the case of incompressible flows, we now have together with the conservation of mass (Eq. 2.2.2) a closed system of equations which can be solved for the pressure and velocity fields.

In the case of compressible flows, we have to establish a balance for the total energy, based on the first law of thermodynamics. Again, we can derive this equation by balancing the total energy in a control volume according to Eq. 2.2.1. To do so we take enthalpy h as our quantity of interest and formulate the *conservation of energy* as

$$\rho \frac{D}{Dt}h = \nabla \cdot (k \nabla T) + \frac{D}{Dt}p + \Phi + S_h\,, \tag{2.2.6}$$

where k is the thermal conductivity, S_h the net source of enthalpy, and Φ the viscous dissipation function. In this system, we now have a varying density and need an appropriate *equation of state* to relate density, pressure, and temperature. As equation of state we often choose the well-known ideal gas law

$$\rho = \frac{p}{R_{\text{spec}} T}\,, \tag{2.2.7}$$

where R_{spec} is the specific gas constant. The last equation needed to close the system is the relationship between enthalpy and temperature

$$dh = c_{\text{p}}\, dT\,, \tag{2.2.8}$$

where c_{p} is the specific heat capacity. This gives a closed system of equations again and we can solve it for the pressure, temperature, enthalpy, density, and velocity fields.

2.3 Heat Transfer

Thermal energy can be transferred by the 3 basic modes of heat transfer: (i) radiation, (ii) conduction (or diffusion), and (iii) convection. For high temperature applications, such as CSTE, the radiative heat transfer is very often dominant. But, as we have seen in the literature overview in Chapter 1, the convection can also be a highly important form of heat transfer. Conduction on the other hand, normally plays a less important role and can be easier controlled than the other 2 modes of heat transfer.

In academia, there is an ongoing discussion on the number of modes of heat transfer. More precisely, it was proposed already by Nusselt that there are only 2 basic modes of heat transfer: radiation and conduction (see Martin (2014) and von Böckh and Wetzel (2017) for more details). I support this reasoning because as shown below, the fundamental physics that underlie convection are thermal conduction and advective transport through bulk motion. So, thermal convection is actually a hybrid description that uses the physics of heat transfer (conduction) and the physics of fluid dynamics (advective transport). Nonetheless, I see the practicability to add convection as the third heat transfer mode because it allows for the introduction of the concept of heat transfer coefficient. Consequently, in this work I use the conventional 3 modes of heat transfer.

In **thermal radiation** the energy is transferred by the quantum of light, the photon. The photon is known to behave either like an electromagnetic wave or like a particle depending on the situation. This is called the wave-particle duality. However, for engineering problems on a macroscopic scale this normally does not cause troubles. Every material at $T > 0\,\mathrm{K}$ emits energy via radiation (Howell et al. (2011)). This emission depends in the most general form on material temperature, material properties, emission direction, emission wavelength λ, and refractive index n of the surrounding material. To simplify we assume a perfect absorber and emitter which absorbs all incident radiation and emits the maximum amount of energy in all directions and at each wavelength. Such a perfect absorber-emitter is called a blackbody. The amount of power emitted by such a blackbody per wavelength and integrated over a hemisphere as a function of temperature is called *hemispherical spectral emissive power* of a blackbody $E_{\lambda\mathrm{b}}$ and is calculated via *Planck's law* as

$$E_{\lambda\mathrm{b}} = \frac{2\pi C_1}{n^2\lambda^5\left[\exp\left(\frac{C_2}{n\lambda T}\right)-1\right]}, \tag{2.3.1}$$

where C_1 and C_2 are 2 auxiliary radiation constants based on the speed of light, Planck's constant, and Boltzmann's constant. Integrating this equation over the full wavelength spectrum gives the *hemispherical total emissive power* of a blackbody E_b which is also called the *Stefan-Boltzmann law*

$$E_\mathrm{b} = n^2\sigma T^4, \tag{2.3.2}$$

where σ is the Stefan-Boltzmann constant. For the further analysis we assume $n = 1$ which is the case for vacuum and is also close enough for air under normal conditions.

At an interface, the radiation is either absorbed, reflected or transmitted. This is taken into account by introducing the absorptivity α, the reflectivity ρ, and the transmissivity τ. In addition, we also introduce the emissivity ϵ. The first 3 properties are defined as the fraction of the incident energy that is absorbed, reflected or transmitted at an interface, respectively. The emissivity is the ratio of the emitted energy to the energy emitted by a blackbody at the same temperature. In Table 2.3.1 these definitions are defined briefly.

The absorptivity and emissivity are related to each other via *Kirchhoff's law*

$$\alpha(T) = \epsilon(T). \tag{2.3.3}$$

And again, also here applies the first law of thermodynamics and we can write the sum of all the energy fractions at an interface as

$$\alpha + \rho + \tau = 1. \tag{2.3.4}$$

In the above paragraphs we already assumed that these properties are independent of the wavelength and the direction. These assumptions are called gray and diffuse, respectively.

Table 2.3.1: The 4 properties at radiation interfaces: absorptivity, reflectivity, transmissivity, and emissivity.

Property	Definition
Absorptivity α	Absorbed fraction of the incident energy
Reflectivity ρ	Reflected fraction of the incident energy
Transmissivity τ	Transmitted fraction of the incident energy
Emissivity ϵ	Ratio of the emitted energy compared to a blackbody

When calculating the radiative heat transfer between surfaces at different but isothermal temperatures in a transparent medium it is helpful to make use of a quantity that indicates how much of the emitted energy at 1 surface reaches the other surface. This fraction is called *view factor* or *configuration factor* and is symbolized by F_{j-k} where j and k are indices of the respective surfaces. These factors can be calculated based on the geometrical relations of the different surfaces and are listed for many geometrical configurations in many sources, for example online on Howell (2018).

Now, we are able to calculate the net radiative flux between 2 surfaces by using for example the *radiosity method* which gives 1 equation per surface based on the following equation

$$J_k + \frac{1-\epsilon_k}{\epsilon_k} \sum_{j=1}^{N} \left(J_k - J_j\right) F_{k-j} = \sigma T_k^4 , \tag{2.3.5}$$

where J is the radiosity or net radiative energy leaving surface j or k, which is the sum of the emitted and reflected energy.

Thermal conduction describes the diffusion of thermal energy in solids and fluids. The driving force is the gradient of the temperature field. If we add an additional energy source term S_{vol} and plug in the right parameters to the general diffusion equation we get the *heat equation*

$$\rho c_{\text{p}} \frac{\partial}{\partial t} T = \nabla \cdot (k \nabla T) + S_{\text{vol}} , \tag{2.3.6}$$

where k is the thermal conductivity. For steady-state, 1D in direction n, and without source terms this simplifies to *Fourier's law*

$$\dot{q}_{\text{cond}} = -k \frac{d}{dn} T . \tag{2.3.7}$$

Thermal convection is the process of transferring heat within fluids and between fluids and solids. The governing equations (Eqs. 2.2.2, 2.2.5, and 2.2.6) which describe the flow and therefore also the convection were introduced in Section 2.2. It may help to understand the process of transferring heat from a solid to a fluid when seeing it as a 2-step process: (i) conduct heat through the stagnant layer of fluid at the surface (no-slip condition) to the near-wall fluid particles and (ii) transport the near-wall fluid particles which have been heated away by advection. In step (i) we need to define the temperature gradient at the wall to compute the conducted heat to the fluid according to Eq. 2.3.7. Step (ii) is already much more complicated and we have to solve the governing equations to know how much of the heat is transported away by the macroscopic fluid motion. Thus, a *heat transfer coefficient* h is introduced to simplify the calculation of heat transferred by convection. The related equation is also called *Newton's law of cooling*

$$\dot{q}_{\text{conv}} = h (T_\infty - T_{\text{w}}) , \tag{2.3.8}$$

where T_∞ and T_w symbolize the temperature in the bulk and of the wall, respectively. The explanation developed can analogously be used to understand the transfer of heat from the fluid to the solid.

In the introduction, the concept of *free convection* or *natural convection* and the concept of *forced convection* were already used. Free convection occurs when there are density gradients near the surface that drive the flow. If the fluid is blown past the surface because of a naturally or mechanically generated pressure gradient, and hence wind speed, we talk about forced convection. The heat transfer coefficient h is typically not uniform across a surface and depends heavily on the flow conditions, thermophysical properties, and geometry and dimensions of the surface (Kakaç et al. (2014)). Forced convective heat transfer coefficients can be more than 1 order of magnitude higher than free convective heat transfer coefficients. For simpler geometries one can look up correlations for *Nusselt numbers*, for example in the VDI Heat Atlas (VDI (2010)), and calculate the heat transfer coefficient from the definition of the Nusselt number Nu

$$Nu = \frac{hL}{k}. \tag{2.3.9}$$

In the most general form, the Nusselt number (see Eq. 2.3.10) is a function of the Grashof number, Reynolds number, Prandtl number $Pr = \mu/(\rho\alpha)$, geometry, and the direction of the heat flux which is expressed by the temperature ratio T/T_w.

$$Nu = f\,(Gr, Re, Pr, \text{geometry}, T/T_w) \tag{2.3.10}$$

In the case of mixed convection, it is possible to add the forced and free heat transfer coefficient as already introduced in Eq. 1.3.11. According to VDI (2010), this procedure is considered proven only where gravity and forced wind speed vectors are perpendicular.

2.4 Dimensional Analysis and Method of Similitude

To reduce the number of parameters in a physical equation we can make use of the *dimensional analysis* which lets us calculate a reduced number of *nondimensional parameters*. By expressing the equation with these nondimensional parameters we are also able to generalize the equation. This allows for example to design scaled experiments based on the method of similitude (Kline (1986)).

Let us start with a brief definition of dimensional analysis which is often called interchangeably *π theorem* or *Buckingham π theorem*. The number of dimensional parameters p_i shall be m. Then, we can formulate the physical equation as

$$f\,(p_1, p_2, \ldots, p_m) = 0. \tag{2.4.1}$$

In this equation, we will find k primary quantities (or dimensions). Subtracting the number of primary quantities from the number of dimensional parameters we get $n = m - k$ nondimensional parameters π_j. Each nondimensional parameter π_j is then a product of the primary quantities raised to an exponent $a_i \in \mathbb{R}$

$$\pi_j = \prod_{i=1}^{m} p_i^{a_i} \quad | \; j = 1, \ldots, n. \tag{2.4.2}$$

One of the simplest form of a nondimensional parameter is the nondimensional length $x^* = x/L$. By using this approach, the remaining parameters in the Navier-Stokes equation

(Eq. 2.2.5) can be nondimensionalized with $u_x^* = u_x/U_\infty$, $t^* = tU_\infty/L$, and $p^* = p/(\rho U_\infty^2)$. We then neglect volumetric forces and write the incompressible Navier-Stokes in 1D as

$$\frac{\partial}{\partial t^*}u_x^* + u_x^*\frac{\partial}{\partial x^*}u_x^* = -\frac{\partial}{\partial x^*}p^* + \frac{\mu}{\rho U_\infty L}\frac{\partial^2}{\partial x^{*2}}u_x^*. \tag{2.4.3}$$

The factor before the viscous term (last derivative term) is $1/Re$ which is the inverse of Eq. 1.3.8. We can continue with this procedure on other equations such as the energy equation and find more nondimensional parameters. For the sake of brevity, a selection of nondimensional parameters that are relevant to this work are listed in Table 2.4.1.

Now, we have set the necessary groundwork to advance to the *method of similitude*. This method is based on the idea of similarity of force ratios (Kline (1986)). It was postulated that 2 systems will exhibit similar behavior if (i) geometric, (ii) kinematic, and (iii) dynamic similarity are all guaranteed. This is somewhat simplified and only takes into account fluid dynamics. No heat transfer system or system which involves electrical charge can be modeled based on this postulate. Therefore, this postulate was expanded by Kline (1986) to: If 2 systems obey the same set of governing equations and conditions and if the values of all parameters in these equations and conditions are made the same, then 2 systems must exhibit similar behavior provided only that a unique solution to the set of equations and conditions exist. In other words, in the beginning of a design of an experiment we have to define the relevant governing equations and nondimensional parameters which include force ratios, energy ratios, material property ratios, and so on. These ratios have to be kept equal in order to maintain similarity.

2.5 Boundary Layer Theory

Many flows or flow regions, especially those far from any immersed bodies or walls, can be approximated as ideal, inviscid flows (Schlichting and Gersten (1997)). Such flows are characterized by $Re \to \infty$. But, inviscid flows do not adhere to the no-slip condition and therefore exhibit unphysical flow phenomena close to walls. This problem cannot be solved by only applying a no-slip condition at the walls because the fluid would not decelerate to zero without a force. This force is called viscous force and is introduced through the viscosity and the resulting shear stress. To solve this the *boundary layer theory* introduces a thin zone adjacent to a wall, the *boundary layer*. In this boundary layer the governing equations also incorporate the viscous forces. Outside of this boundary layer the viscosity can still be neglected with good accuracy.

Such a boundary layer typically starts as a *laminar boundary layer*, passes a transition region, and finally evolves to a *turbulent boundary layer*. Such growth of the boundary layer on a flat plate is schematically drawn in Fig. 2.5.1. As the boundary layer starts to become turbulent in the transition region at the critical length x_{cr}, the laminar boundary layer is squeezed beneath the turbulent zone, which is indicated by the dashed line, and constitutes the lowest part of the turbulent boundary layer.

Let us start with the understanding of the laminar boundary layer on a flat plate. On the flat plate we apply a no-slip condition. As soon as the flow touches the flat plate the velocity of the wall-adjacent fluid particles is zero. Then, the viscosity forces the velocity profile to smoothly adapt the velocity from zero to the free-stream velocity U_∞. The height over which this change takes place is called the boundary layer thickness δ. This situation is depicted in Fig. 2.5.2. Since there is no sharp border between the boundary layer and the free-stream the limit of the thickness is defined for example at the height where the velocity

Table 2.4.1: A selection of nondimensional parameters that are relevant to this work.

Nondimensional parameter	Equation	Definition
Reynolds number	$Re = \frac{\rho U L}{\mu}$	$\frac{\text{inertial forces}}{\text{viscous forces}}$
Grashof number	$Gr = \frac{\beta (T_w - T_\infty) L^3 \rho^2 g}{\mu^2}$	$\frac{\text{buoyancy forces}}{\text{viscous forces}}$
Richardson number	$Ri = \frac{Gr}{Re^2}$	$\frac{\text{buoyancy forces}}{\text{inertial forces}}$
Prandtl number	$Pr = \frac{\mu}{\alpha \rho}$	$\frac{\text{momentum diffusivity}}{\text{thermal diffusivity}}$
Rayleigh number	$Ra = GrPr$	$\frac{\text{buoyancy forces}}{\text{viscous forces}}$
Nusselt number	$Nu = \frac{hL}{k}$	$\frac{\text{convection}}{\text{conduction}}$
Stanton number	$St = \frac{Nu}{RePr}$	modified Nusselt number
Strouhal number	$Sr = \frac{fL}{U}$	nondimensional frequency of oscillation
Mach number	$Ma = \frac{U}{c}$	$\frac{\text{flow velocity}}{\text{speed of sound}}$
Peclet number	$Pe = RePr$	$\frac{\text{advective transport}}{\text{diffusive transport}}$
Colburn j factor	$j = StPr^{2/3}$	nondimensional heat transfer coefficient
Drag coefficient	$C_d = \frac{F_d}{\frac{1}{2}\rho U^2 DL}$	$\frac{\text{drag forces}}{\text{inertial forces}}$
Skin friction coefficient	$C_f = \frac{\tau_w}{\frac{1}{2}\rho U^2}$	$\frac{\text{wall shear stress}}{\text{dynamic pressure}}$

is 99% of the free-stream value. The thickness at location x can be calculated according to

$$\delta_{\text{lam}}(x) \approx 5\left(\frac{\mu x}{\rho U_\infty}\right)^{1/2} \tag{2.5.1}$$

or in nondimensional form

$$\frac{\delta_{\text{lam}}(x)}{x} \approx \frac{5}{Re_x^{1/2}}. \tag{2.5.2}$$

Remarkable here is that with increasing Reynolds number the nondimensional thickness of the laminar boundary layer decreases.

It was shown empirically that for $Re_x > Re_{\text{cr}} \approx 5 \cdot 10^5$ the laminar boundary layer has evolved into a fully turbulent boundary layer. The turbulent nondimensional boundary layer thickness is then calculated as

$$\frac{\delta_{\text{turb}}(x)}{x} \approx \frac{0.385}{Re_x^{1/5}}. \tag{2.5.3}$$

As mentioned earlier, the turbulent boundary layer is not uniform but consists of different layers. The thin layer next to the wall is called the viscous sublayer or laminar sublayer. In this layer the viscous forces are dominant and the gradients are steeper than in the laminar layer or the external layers of the turbulent layer. This is shown schematically in Fig. 2.5.3. The thickness of the viscous sublayer can be calculated with the following formula:

$$\delta_{\text{vis}} \approx \frac{5\mu}{u_\tau \rho} = \frac{5\mu}{\rho U_\infty}\left(\frac{0.0594}{2Re_x^{1/5}}\right)^{-1/2}, \tag{2.5.4}$$

where u_τ is the friction velocity defined as

$$u_\tau = \left(\frac{\tau_{\text{w}}}{\rho}\right)^{1/2}. \tag{2.5.5}$$

All the concepts introduced above also apply analogously to the thermal boundary layer of the temperature field of a flow. Based on the Prandtl number we can predict whether the thermal boundary layer is of a similar or different thickness. If the momentum diffusivity is larger than the thermal diffusivity it follows that also the velocity boundary layer thickness δ is larger than the thermal boundary layer thickness δ_{T}. This can be summarized as

$$\frac{\delta}{\delta_{\text{T}}} = Pr^{1/3} \quad \Longrightarrow \quad \begin{cases} \delta < \delta_{\text{T}} & \text{if } Pr < 1\,. \\ \delta = \delta_{\text{T}} & \text{if } Pr = 1\,. \\ \delta > \delta_{\text{T}} & \text{if } Pr > 1\,. \end{cases} \tag{2.5.6}$$

To get a feeling of the thickness for the different boundary layers the interested reader may find thicknesses for some examples in Table 2.5.1. These values relate to a boundary layer at the end of a slightly heated plate of 1 m length which is immersed into air at 300 K. Because the Reynolds number is kept constant the values are not expected to change by increasing the pressure. The small discrepancy between the thermal boundary layers is due to a minor change in Prandtl number at higher pressure.

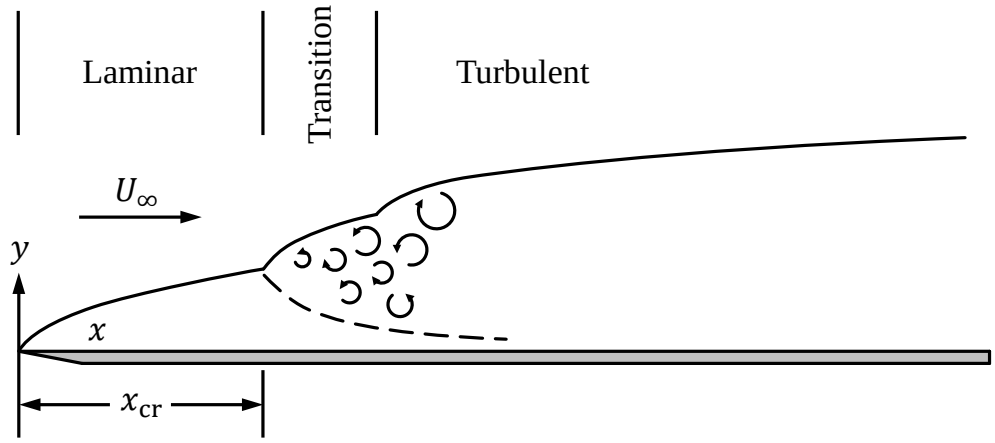

Figure 2.5.1: The growth of a typical boundary layer on a flat plate. In the transition region, which starts at the critical length x_{cr}, the laminar boundary layer is reduced in thickness and forms the lowest part of the turbulent boundary layer.

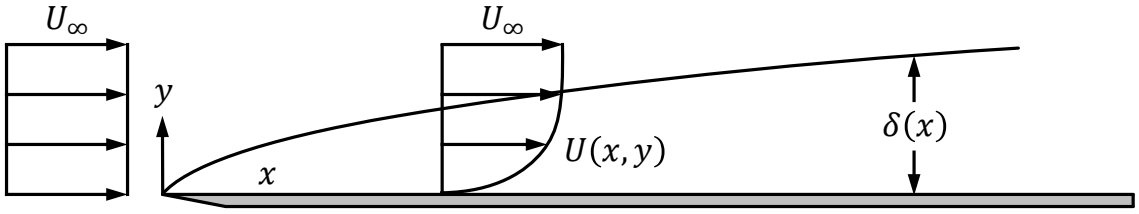

Figure 2.5.2: The laminar boundary layer on a flat plate. The uniform velocity profile changes due to the no-slip condition at the wall. The thickness $\delta(x)$ grows as the flow passes the plate.

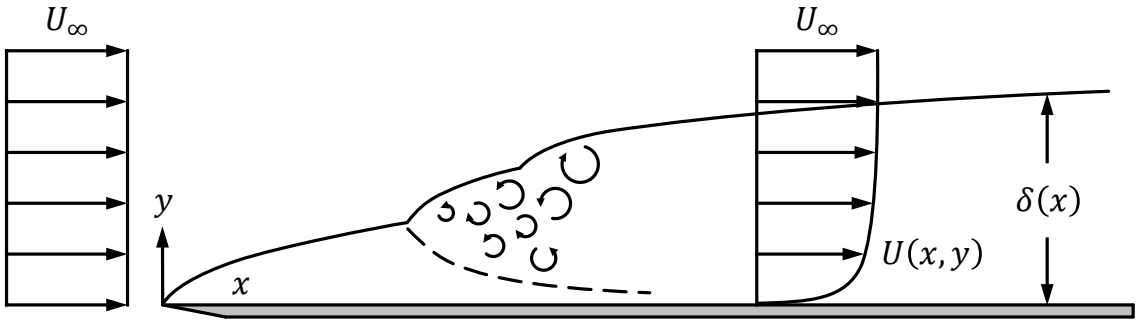

Figure 2.5.3: The turbulent boundary layer on a flat plate. The velocity profile develops while flowing along the wall. The thickness $\delta(x)$ is larger than in the case of a laminar boundary layer.

Table 2.5.1: Some examples of the thickness of different boundary layer types on a flat plate†. Noteworthy is that at the 2 different pressures the thicknesses remain the same because Re is kept constant. The small discrepancy between the thermal boundary layer thicknesses is due to a slightly altered Pr.

	Laminar $Re = 10^5$		Turbulent $Re = 10^6$	
	δ_{lam} / m	δ_{T} / m	δ_{turb} / m	δ_{vis} / m
1 bar	$1.58 \cdot 10^{-2}$	$1.78 \cdot 10^{-2}$	$2.43 \cdot 10^{-2}$	$1.16 \cdot 10^{-4}$
60 bar	$1.58 \cdot 10^{-2}$	$1.74 \cdot 10^{-2}$	$2.43 \cdot 10^{-2}$	$1.16 \cdot 10^{-4}$

†The flat plate is assumed to have a length of 1 m and is immersed in air at 300 K.

2.6 Reynolds Analogy and Colburn Analogy

The analogy between momentum and heat transfer dates back to Reynolds (Kakaç et al. (2014)). He discovered that in turbulent flows close to the wall the shear stress and the heat flux can be written as

$$\frac{\tau}{\rho} = (\nu + \varepsilon)\frac{du}{dy} \tag{2.6.1}$$

$$\frac{\dot{q}}{\rho c_{\mathrm{p}}} = (\alpha + \varepsilon)\frac{dT}{dy}, \tag{2.6.2}$$

where $\tau = \mu \partial u/\partial y$ is the shear stress, ν is the kinematic viscosity $\nu = \mu/\rho$ and ε is the turbulence kinetic energy dissipation. From these equations it follows that if (i) ν and α are negligible compared to ε or (ii) $\nu \approx \alpha$ then direct proportionality of momentum transport and heat transfer can be expected. From condition (ii) we see directly that this analogy applies to fluids with $Pr \approx 1$. By integrating Eqs. 2.6.1 and 2.6.2 and combining the result with Newton's law of cooling (Eq. 2.3.8) and the definition of the skin friction coefficient C_{f} (see Table 2.4.1) we obtain the *Reynolds analogy*

$$St = \frac{C_{\mathrm{f}}}{2}, \tag{2.6.3}$$

where St is the Stanton number.

Colburn found empirically that by introducing a correction term in the Reynolds analogy we allow for $Pr \neq 1$. The *Colburn analogy* is

$$StPr^{2/3} = \frac{C_{\mathrm{f}}}{2}. \tag{2.6.4}$$

This nondimensional number is also called the *Colburn j factor*.

Such analogies are helpful because they allow for investigating just 1 of the 2 transport mechanisms and deduce values or the behavior for the other. It is thus often sufficient to measure for example the heat transfer from a surface and deduce the wall shear stress from the obtained data via 1 of the above analogies.

2.7 Computational Fluid Dynamics

Computational fluid dynamics is the process of numerically solving the governing fluid dynamic equations and hereby simulating a physical system. This process consists of 5 major steps (Haselbacher (2017)):

1. Modeling: Obtain a well-posed mathematical problem by choosing the relevant governing equations, simplifying the equations and applying the appropriate boundary conditions.

2. Discretization: Obtain a discretized numerical model by applying the appropriate discretization schemes.

3. Programming: Obtain a computational model by implementing/choosing the appropriate numerical routines.

4. Execution: Obtain an approximate solution by executing the code.

5. Interpretation: Obtain a human-readable format of the results. Produce an answer or enhance insights. Validate with experimental data and verificate with exact solution if existent.

Each of these steps may introduce uncertainty and errors. These can for example be: modeling errors by simplifying the physical model, discretization errors by the chosen discretization schemes, programming mistakes, and rounding and iteration errors during execution.

Step 1 was initiated by the mathematical modeling in Sections 2.2-2.6. We now continue with modeling the turbulence. The concept of laminar and turbulent flow regimes does not only apply to the boundary layer, it does apply to all real flows. This means that also in a flow without any walls we will encounter turbulence at some point. Therefore, we have to expand the governing Eqs. 2.2.2, 2.2.5, and 2.2.6 and take into account the chaotic or random nature of turbulence (Versteeg and Malalasekera (2007); Ferziger and Peric (2002)). Let us start by defining a quantity $\phi(t)$ which has a time average component $\overline{\phi}$ and a time varying fluctuating component $\phi'(t)$ as

$$\phi(t) = \overline{\phi} + \phi'(t). \tag{2.7.1}$$

This is also called the *Reynolds decomposition*. Then the time average $\overline{\phi}$ is defined as

$$\overline{\phi} = \frac{1}{\Delta t} \int_0^{\Delta t} \phi(t) dt \tag{2.7.2}$$

and the time average of the fluctuating component is zero by definition

$$\overline{\phi'} = \frac{1}{\Delta t} \int_0^{\Delta t} \phi'(t) dt = 0. \tag{2.7.3}$$

Finally, the variance is calculated via

$$\overline{(\phi')^2} = \frac{1}{\Delta t} \int_0^{\Delta t} (\phi'(t))^2 \, dt. \tag{2.7.4}$$

Until now, we said that shear stress can only be found in boundary layers. This is true for external flows that are laminar. In the case of a turbulent external flow the turbulent eddies generate additional shear stresses also within the free stream. The entirety of shear stresses is calculated via the Reynolds stress tensor. Analogously, the turbulent transport also affects the species flux and the heat flux. By plugging in the time average and fluctuating values as defined above we obtain an adapted set of Navier-Stokes equations. These are

called the *Reynolds-averaged Navier-Stokes (RANS) equations*. The conservation of momentum in x-direction for an incompressible fluid without volumetric forces is shown here as an example (this is done analogously for the y-direction, z-direction, conservation of mass, and conservation of energy):

$$\begin{aligned}\rho\frac{\partial}{\partial t}\overline{u_x} = &-\rho\frac{\partial}{\partial x}(\overline{u_x}\,\overline{u_x}) - \rho\frac{\partial}{\partial y}(\overline{u_x}\,\overline{u_y}) - \rho\frac{\partial}{\partial z}(\overline{u_x}\,\overline{u_z}) \\ &+ 2\mu\frac{\partial}{\partial x}\left(\frac{\partial}{\partial x}\overline{u_x}\right) + \mu\frac{\partial}{\partial y}\left(\frac{\partial}{\partial y}\overline{u_x} + \frac{\partial}{\partial x}\overline{u_y}\right) + \mu\frac{\partial}{\partial z}\left(\frac{\partial}{\partial z}\overline{u_x} + \frac{\partial}{\partial x}\overline{u_z}\right) \\ &- \frac{\partial}{\partial x}\overline{p} \\ &- \rho\frac{\partial}{\partial x}\left(\overline{u_x'u_x'}\right) - \rho\frac{\partial}{\partial y}\left(\overline{u_x'u_y'}\right) - \rho\frac{\partial}{\partial z}\left(\overline{u_x'u_z'}\right). \end{aligned} \tag{2.7.5}$$

Comparing this equation with the original Navier-Stokes equation (Eq. 2.2.5) reveals an additional group of terms at the end of the RANS equation which is made up of the fluctuating terms. These extra stress terms are the Reynolds stresses. Since this group adds unknowns to the set of equations, we obtain a system of equations which is not closed. Therefore, we introduce new equations to close the RANS system of equations. This procedure is called the *turbulence closure*. Various models have been proposed, ranging from simple algebraic equations to multiple partial differential equations. Of relevance in this work are only 2-equation models since they offer a good trade-off between accuracy and computational cost. The 2 new quantities introduced are the turbulence kinetic energy k and its dissipation ε defined as

$$k = \frac{1}{2}\left(\overline{u_x'u_x'} + \overline{u_y'u_y'} + \overline{u_z'u_z'}\right) \tag{2.7.6}$$

$$\varepsilon \approx \frac{k^{3/2}}{L}, \tag{2.7.7}$$

where L is the turbulence length scale. Together with the *Boussinesq assumption of isotropic turbulence* we can write (with the indices i and j indicating the Einstein notation) the transport equations for the 2 new quantities as

$$\frac{D}{Dt}(\rho k) = \nabla\cdot\left(\frac{\mu_\mathrm{t}}{\sigma_k}\nabla k\right) + 2\mu_\mathrm{t}\overline{s_{ij}}\,\overline{s_{ij}} - \rho\varepsilon \tag{2.7.8}$$

$$\frac{D}{Dt}(\rho\varepsilon) = \nabla\cdot\left(\frac{\mu_\mathrm{t}}{\sigma_\varepsilon}\nabla\varepsilon\right) + C_{1\varepsilon}\frac{\varepsilon}{k}2\mu_\mathrm{t}\overline{s_{ij}}\,\overline{s_{ij}} - C_{2\varepsilon}\rho\frac{\varepsilon^2}{k}, \tag{2.7.9}$$

where $\mu_\mathrm{t} = \rho C_\mu k^2/\varepsilon$ is the eddy viscosity, $\overline{s_{ij}}$ the time-averaged strain rate, and σ_k, σ_ε, $C_{1\varepsilon}$, $C_{2\varepsilon}$, and C_μ 5 constants. This is the *k-ε model*. There are a variety of related 2-equation turbulence models. In the following, only the equations for the *shear stress transport (SST) k-ω model* (Menter (1994)) are presented, because it is the model used in this work (see reasoning in Section 3.3.2). The equation for k is slightly altered to

$$\frac{D}{Dt}(\rho k) = \nabla\cdot\left(\left(\mu + \frac{\mu_\mathrm{t}}{\sigma_k}\right)\nabla k\right) + P_k - \beta^\star\rho k\omega, \tag{2.7.10}$$

where P_k is the turbulence kinetic energy production and $\beta^\star$ a constant. The equation for the specific turbulence kinetic energy dissipation ω is

$$\begin{aligned}\frac{D}{Dt}(\rho\omega) =& \nabla\cdot\left(\left(\mu+\frac{\mu_\mathrm{t}}{\sigma_\omega}\right)\nabla\omega\right)+\frac{\gamma\rho}{\mu_\mathrm{t}}P_k-\beta\rho\omega^2 \\ &+2(1-F_1)\frac{\rho\sigma_{\omega,2}}{\omega}\frac{\partial}{\partial x_j}k\frac{\partial}{\partial x_j}\omega,\end{aligned} \tag{2.7.11}$$

where F_1 is a blending function and σ_ω, $\sigma_{\omega,2}$, γ, and β are 4 constants. The advantages of the SST k-ω model are that (i) it is actually a hybrid model of a k-ω model near the wall and a k-ε model in the far-field and (ii) it has limiters built in for the eddy viscosity μ_t and the production of k. To guarantee a smooth transition between the k-ε and k-ω models across the boundary layer the blending function F_1 was incorporated. More details on this turbulence model and its constants are given in Appendix B. With this turbulence closure we have closed our system of equations again and can model the flow transient and compressible with turbulent fluctuations averaged over a very short time.

To finalize the modeling we need to apply the appropriate boundary conditions. Consequently, we refine the turbulent boundary layer model which was explained in Section 2.5. The laminar sublayer was already mentioned and is the innermost part of the turbulent boundary layer. In the laminar sublayer or viscous sublayer the viscous forces dominate. Therefore, we can assume that the shear stress is approximately constant throughout this sublayer and we first nondimensionalize the velocity as

$$u^+ = \frac{u_x}{u_\tau} \tag{2.7.12}$$

and then nondimensionalize the wall normal coordinate as

$$y^+ = \frac{y u_\tau}{\nu}. \tag{2.7.13}$$

From the definition of the wall shear stress the following relationship which is valid for $y^+ < 5$ can be obtained

$$u^+ = y^+. \tag{2.7.14}$$

In the buffer layer ($5 < y^+ < 30$) the viscous and turbulent stresses are of similar magnitude. When the turbulent stresses start to dominate for approximately $y^+ > 30$ we can formulate another relationship which is often called the *log-law*

$$u^+ = \frac{1}{\kappa}\ln\left(Ay^+\right), \tag{2.7.15}$$

where κ is the von Karman constant (≈ 0.4) and A another constant depending on the surface roughness. Further out in the boundary layer the turbulent stresses reduce and the inertial forces start to dominate. This is called the outer layer ($y^+ > 500$) and we can formulate a relationship which is often termed the *velocity-defect law*

$$\frac{U_\infty - u_x}{u_\tau} = -\frac{1}{\kappa}\ln\left(\frac{y}{\delta}\right)+B, \tag{2.7.16}$$

where B is a constant. A graphical summary of this refined turbulent boundary layer can be seen in Fig. 2.7.1.

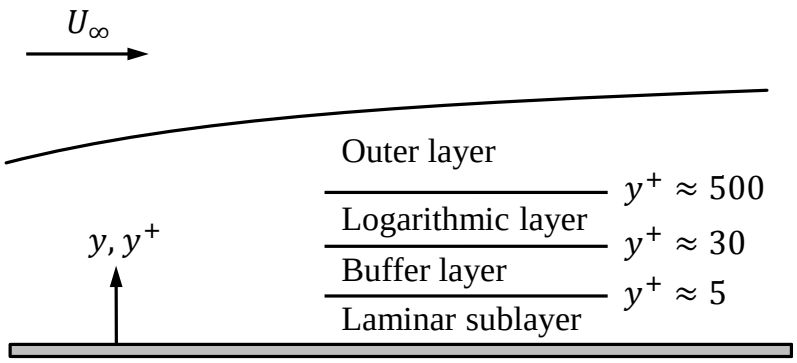

Figure 2.7.1: Different sublayers in the turbulent boundary layer. y^+ is the nondimensional distance from the wall.

Step 2 of CFD simulations involves the discretization of the physical domain. After carefully selecting the relevant regions upstream and downstream as well as to the sides, top and bottom, we split the physical domain in a certain number of discrete elements which is called grid or mesh. The smaller these elements are, the smaller are the physical phenomena we can capture with a specific mesh. The size of the mesh elements is also constrained by the boundary layer modeling and hence the validity regions of Eqs. 2.7.14, 2.7.15, and 2.7.16. We can consequently distinguish 2 different modeling approaches for the near-wall region: (i) with a fine near-wall resolution and (ii) with a coarse near-wall resolution. Models that are able to work with the first approach are also called *low-Re turbulence models*, those that can work with the second approach are called *high-Re turbulence models*. It is important to note that this Reynolds number is not based on the free-stream properties but on the turbulent properties within the boundary layer $Re_t = U_t L_t/\nu$. This turbulent Reynolds number is being reduced while coming closer to the wall and finally vanishes at the wall. Consequently, the turbulent Reynolds number is low in the viscous sublayer and turbulence models which are able to resolve the viscous sublayer are therefore called low-Re turbulence models. It follows if we want to resolve the viscous sublayer ($y^+ < 5$) we need to have a first grid point within $y^+ < 5$ and apply a boundary condition like Eq. 2.7.12. On the other hand, when using a grid with a first grid point in the range $30 < y^+ < 500$ we can apply the log-law (Eq. 2.7.15). These boundary conditions are in fact *fixed value* boundary conditions or Dirichlet boundary conditions. Another common boundary condition type prescribes a *fixed gradient* and is called Neumann boundary condition. Together with the boundary conditions, either in Dirichlet or in Neumann form, for the remaining quantities such as temperature or pressure we obtain a well-posed mathematical problem.

Thereafter, we have to integrate the governing equations (if in derivative form) to obtain the integral form of the governing equation. This is done with the *divergence theorem*:

$$\int_V \nabla \cdot \phi dV = \int_A \phi \cdot \mathbf{n} dA, \tag{2.7.17}$$

where ϕ is a vector quantity and n is the surface normal of the infinitesimal surface dA. This allows us now to discretize the physical domain and calculate the finite volume balances on the basis of the fluxes through the bounding faces. This process is called the *finite volume method* and is the most-widely used method in CFD. To discretize the governing mathematical equations on the mesh we may chose amongst a large variety of discretization schemes. The chosen scheme should be:

- Conservative: The flux of quantity ϕ out of 1 face of a finite volume must equal the flux into the adjacent face of the neighbouring finite volume.
- Bounded: In the absence of sources, the value of quantity ϕ in the domain should not exceed the boundary values.
- Transportive: The direction of the flow (if $Pe \gg 1$) has to be incorporated in the scheme in order to correctly weigh the influence of the upstream and downstream values of a node.
- Accurate: The leading Taylor series truncation error and thus the order of the discretization scheme should be at least of second order.

Through the discretization we obtain a system of algebraic equations which can be solved by a range of algebraic solvers. Since these solvers mostly work on the basis of iterative algorithms, we additionally need initial conditions for the whole domain including the boundaries. Such an initial guess maybe obtained from an educated guess, a known starting point or a previous simulation such as a potential flow solution. In Section 3.3.7 the used discretization schemes, initial conditions, and solvers are introduced.

The coding of the solution procedure (**Step 3**) is very often not done by the users themselves, but by a company or institution. This work relies on a third-party open-source software package. Therefore, the interested reader is referred to the online documentation (OpenFOAM (2018a)).

The needed steps to execute the numerical model (**Step 4**) is covered in-depth in Section 3.3. What deserves to be mentioned here are the concepts of residuals and convergence. The residual at iteration i is the remainder of the difference between the exact solution and the iterative solution at iteration i. Since the exact solution is not known, often an arbitrary initial residual is used to normalize the consecutive residuals. It is important to mention here that the residuals alone are not a good measure of convergence because they are summed or averaged over all grid points. Therefore, one also needs to monitor the convergence of other quantities. In the best case, appropriate integral quantities are monitored, too.

And last but not least, in **Step 5** the CFD simulations need to be checked for plausibility and the approximate solution needs to be interpreted to obtain a human-readable result. Both are presented in detail in Chapters 4 to 6.

Chapter 3

Methods

This chapter focuses on the detailed description of the methods used for both the experimental and numerical works of the thesis. It starts off with the definition of the CSTE system. It then continues to introduce the details of the experimental campaign, including the wind tunnel setup, the wind tunnel models, the measurement system, and the data processing. A special emphasis is laid on the explanation of the novel ringlike design of hot-film sensors and the implications for the measurements. Thereafter, the section on numerical methods covers relevant aspects such as for example the turbulence modeling, the boundary and initial conditions, the meshing, the discretization, and the selected solver. Wherever the numerical methods on the wind tunnel scale and on the original scale differ, this is given in the respective section, too.

3.1 Definition of the CSTE System

In the Introduction, the need for investigation of large CSTE systems with a cavity receiver was shown. Here, the detailed settings and boundary conditions for such a system are given. We need to define for example the form and size of the cavity, its temperature, its height, the tower geometry or the wind speed and wind direction at the chosen site. First, the technical boundary conditions are given. Then, the external boundary conditions set by the meteorology are presented. Finally, the combination of all these boundary conditions leads to a set of nondimensional numbers which describe the investigated system and may be used to establish the link between the wind tunnel scale and the original scale. These nondimensional boundary conditions also help to relate to other research.

3.1.1 Technical Boundary Conditions

The studied CSTE system is a central receiver system with a cavity receiver. The intercept power entering the aperture was defined to be 100 MW. Since the results shall be applicable as generally as possible, the investigation shall be independent of a heat transfer medium. Therefore, a heat transfer medium was not included in this work. In addition, the geometry shall be as general as possible. This led to the selection of a circular cylinder both for the cavity and for the tower. The cavity had a diameter-to-length ratio of 1 and an inner diameter of 15 m. The basic aperture ratio, this means *aperture-diameter-to-inner-cavity-diameter ratio* X_{ap}, was 0.8 which is an approximation of typical values found in real cavity receivers such as PS20 in Spain or Khi Solar One in South Africa. To generalize the results additional aperture ratios X_{ap} of 0.6 and 1 were included in this study. The height of the tower was 200 m and was optimized with the heliostat field layout software HFLCAL (Schwarzbözl et al. (2009)). The diameter of the tower is chosen to be 20 m which is a typical diameter for towers of this height. Real cavity receivers, for example PS20 in Spain or THEMIS in France, have only small *cavity inclination angles* γ of approximately 0° to 20°, and thus face the horizon or slightly towards the ground. Therefore, cavity inclination angles of 0° and 30° were chosen as well as 1 additional inclination of 60° to generalize the results and for better comparability to previous studies such as Paitoonsurikarn et al. (2004) or Flesch et

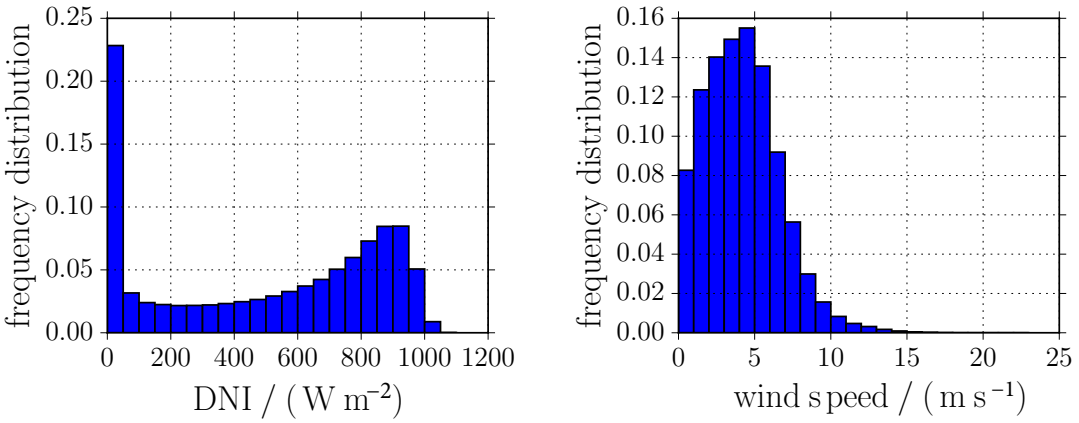

Figure 3.1.1: Frequency distribution of the DNI and the wind speed measured daytime on the Plataforma Solar de Almería, Spain. The bins of the DNI and wind speed are $50\,\mathrm{W\,m^{-2}}$ and $1\,\mathrm{m\,s^{-1}}$, respectively.

al. (2015). The temperature at the walls of receivers typically reach 800 K to 1000 K (Ho (2017)). In this study, a value of 900 K was chosen for the original scale CFD simulations.

3.1.2 Meteorological Boundary Conditions

The economics of a CSTE system is heavily dependent on the selected site and its meteorological conditions such as the *direct normal irradiance (DNI)* (IRENA (2012)). As shown in the introduction, the wind speed and its direction influence the overall heat loss of a receiver which then influences the receiver efficiency and economics of the plant. Consequently, these 2 variables are also of importance for a CSTE system. In the following, measurements from 3 sites are compared to each other in terms of DNI and wind speed characteristics. The first site is located on the Plataforma Solar de Almería in Spain, the second is near Missour in Morocco (Schüler et al. (2016)), and the third one is located inland from Alexander Bay in South Africa (SAURAN (2017)). The following wind speeds were measured at these 3 sites at a height of 10 m over several years.

When considering wind speed and wind direction we can neglect the values at night. By only considering the daytime values of wind speed we may plot the frequency distribution of the DNI and the wind speed in a histogram as in Fig. 3.1.1. The bins of the DNI and wind speed are $50\,\mathrm{W\,m^{-2}}$ and $1\,\mathrm{m\,s^{-1}}$, respectively.

By correlating the wind speed and the solar energy we can plot the direct normal solar energy fraction at wind speeds up to a certain value. This is shown in Fig. 3.1.2. On the Plataforma Solar de Almería (see Fig. 3.1.2a), 80% of the direct normal solar energy reaches the station while winds of equal or less than about $6.5\,\mathrm{m\,s^{-1}}$ are blowing. All direct normal solar energy comes in at equal or less than about $10\,\mathrm{m\,s^{-1}}$. In Fig. 3.1.2b this is plotted for the site near Missour and in Fig. 3.1.2c it is plotted for the site near Alexander Bay. In the case of the Moroccon station 80% and 100% of the solar energy reaches ground at winds of equal or less than about $5\,\mathrm{m\,s^{-1}}$ and $12\,\mathrm{m\,s^{-1}}$, respectively. In the case of the South African station the wind speeds for the same ratios are equal or less than about $9\,\mathrm{m\,s^{-1}}$ and $13\,\mathrm{m\,s^{-1}}$.

The upper limit of the wind speed where a CSTE system can still operate is determined by the mechanical stability of the heliostats. Emes et al. (2015) showed for different locations that it is economically beneficial to choose a design wind speed of the heliostats of roughly $10\,\mathrm{m\,s^{-1}}$. By comparing Figs. 3.1.2a to 3.1.2c for a system with a design wind speed of $10\,\mathrm{m\,s^{-1}}$ we find that almost all of the solar energy is collected for speeds below

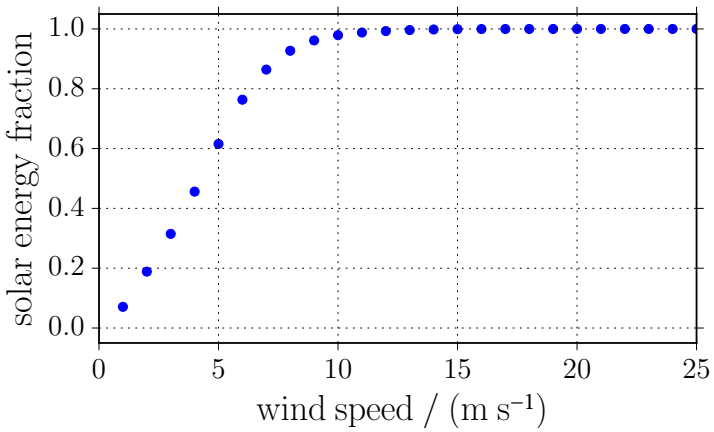

(a) Plataforma Solar de Almería, Spain.

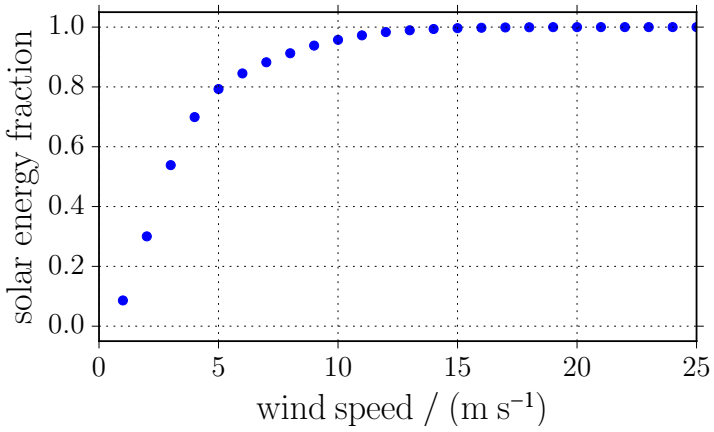

(b) A site close to Missour, Morocco.

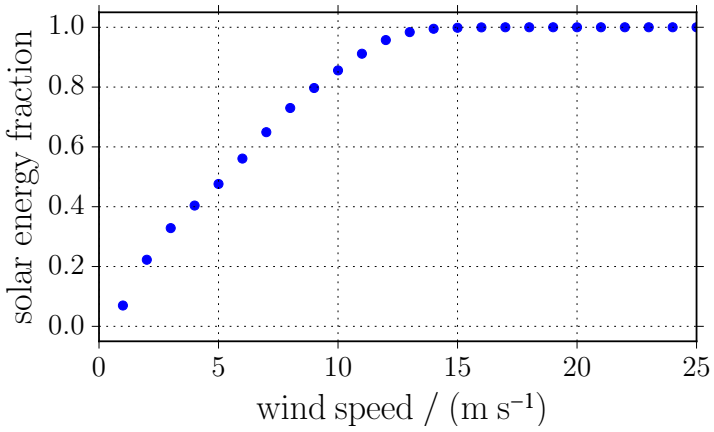

(c) A site inland from Alexander Bay, South Africa.

Figure 3.1.2: Fraction of direct normal solar energy which reaches ground at wind speeds up to a specific value. These data were measured daytime at 3 sites.

this value.

Let us now scale the values measured at a reference height h_{ref} of 10 m to the relevant height h for our cavity receiver. This can be done by using either of the 2 following equations (Emeis (2013))

$$\frac{U_h}{U_{\text{ref}}} = \frac{\ln(h/z_0)}{\ln(h_{\text{ref}}/z_0)} \tag{3.1.1}$$

$$\frac{U_h}{U_{\text{ref}}} = \left(\frac{h}{h_{\text{ref}}}\right)^a, \tag{3.1.2}$$

where z_0 is the surface roughness and a is a constant exponent which is sometimes also dependent on the surface roughness but usually chosen to be 1/7. The first equation is called the logarithmic wind speed profile and the second is called the power-law wind speed profile. The logarithmic profile is more accurate for lower heights up to around 100 m. The power-law profile is more accurate to extrapolate to heights above 100 m but should not be used to scale to heights below roughly 30 m (Emeis (2013)). Thus, we extrapolate the wind speed from 10 m to the lower edge of the cavity at 176 m by the power-law. This gives a factor of 1.53 with which we have to multiply the values at 10 m. This limits the maximum relevant wind speed to about 15 m s^{-1} at the height of the cavity.

In addition to the magnitude, the direction of the wind speed is also of interest because it has been shown that the direction has an influence on the convective heat loss, too (see Section 1.3). For each of the sites in Spain, Morocco, and South Africa, a windrose of the daytime values is plotted in Figs. 3.1.3a, 3.1.3b, and 3.1.3c, respectively. Noteworthy is that each site has only 1 or 2 predominant directions.

3.1.3 Nondimensional Boundary Conditions

With the boundary conditions given in the previous sections and the nondimensional parameters given in Table 2.4.1 we can calculate the relevant nondimensional parameters in Eqs. 3.1.3 to 3.1.5. The Reynolds number represents the inertial forces best when based on the external flow characteristics and the internal diameter of the cavity. The Grashof number represents the buoyancy forces best when based on the internal flow characteristics in the cavity, the film temperature, and the cavity dimensions. Both definitions follow previous publications (see for example Flesch et al. (2015)).

$$Gr \approx 1.2 \cdot 10^{13} \tag{3.1.3}$$

$$Re \approx \left[0, \ldots, 1.4 \cdot 10^{7}\right] \tag{3.1.4}$$

$$Ri \approx \left[6.1 \cdot 10^{-2}, \ldots, \infty\right] \tag{3.1.5}$$

From the nondimensional boundary conditions we obtain the information that the buoyant flow within the cavity is clearly in the fully turbulent regime (Kakaç et al. (2014)). Also the incident flow is turbulent, because it is an atmospheric boundary layer which is in fact a very large boundary layer with $Re \to \infty$ (Kaimal and Finnigan (1994)). Also the boundary layer on the tower and the wake after it are turbulent (Zdravkovich (1997)). It is interesting to note that the heat loss from the cavity is expected to be in the mostly free convection regime for low wind speeds and in the mostly forced convection regime for high wind speeds. This means that each site has its own convective heat loss characteristics depending on its nondimensional boundary conditions.

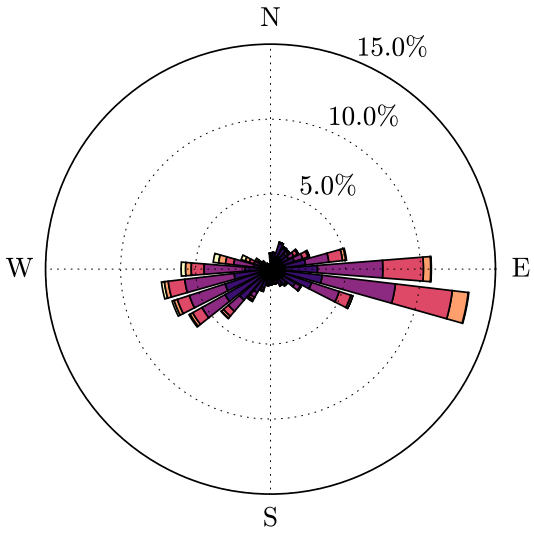

(a) Plataforma Solar de Almería, Spain.

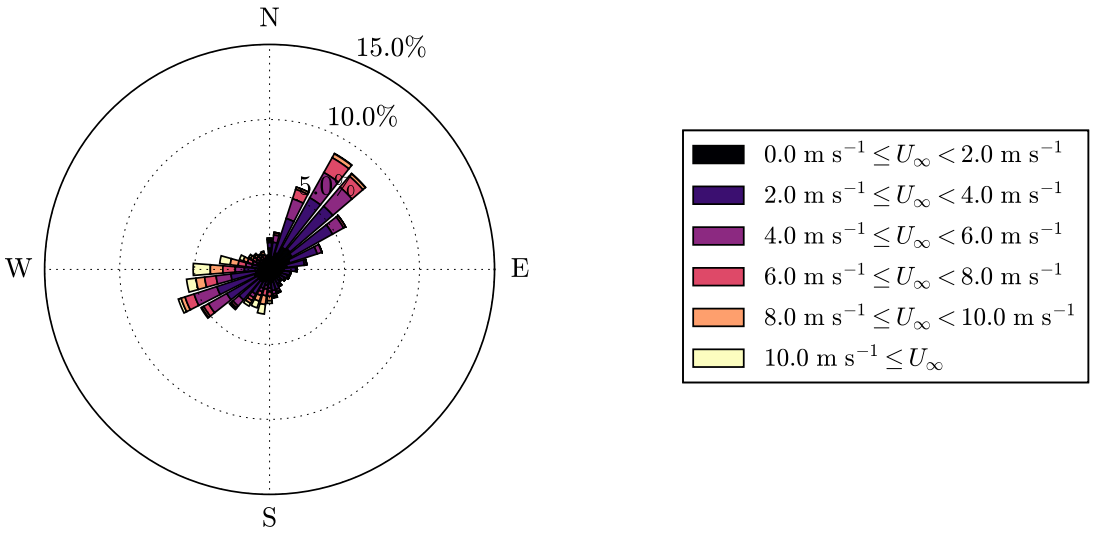

(b) A site close to Missour, Morocco.

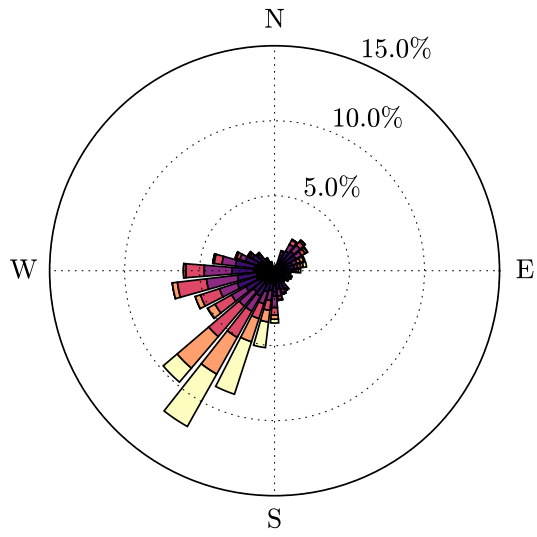

(c) A site inland from Alexander Bay, South Africa.

Figure 3.1.3: Frequency distribution of direction and wind speed measured daytime at 3 sites.

Table 3.2.1: Comparison of the Reynolds numbers in the wind tunnel, the corresponding wind tunnel wind speeds and the scaled wind speeds on the original scale.

Reynolds number	Wind tunnel U_∞ / (m s^{-1})	Original scale U_∞ / (m s^{-1})
$1.5 \cdot 10^6$	6.7	1.6
$3.0 \cdot 10^6$	13.6	3.2
$4.5 \cdot 10^6$	20.5	4.8
$6.0 \cdot 10^6$	27.4	6.4

3.2 Experimental Methods

As stated in Chapter 1, 1 of the goals of this work is to shed light on the heat loss from cavities in the limit of pure forced convection. For this reason, a wind tunnel experiment was designed with a flow regime dominated by forced convection which is true if the following condition holds:

$$Ri = \frac{Gr}{Re^2} \ll 1\,. \tag{3.2.1}$$

By applying the method of similitude, introduced in Section 2.4, we can reduce the length scale for example by a factor in the order of 100. To match the Reynolds number of the model with the real scale we could increase the density and/or the velocity. This can be done simultaneously in a high-pressure wind tunnel. In the following paragraphs the setup of this work in a high-pressure wind tunnel is described. This includes the different geometries and also the reduction measures. The use of *hot-film sensors* in *constant-temperature anemometry (CTA)* mode is justified and explained in Section 3.2.1.1. In the same section, a ringlike design of a hot-film sensor is presented. I adapted the hot-film design to make the sensors more independent of the direction. The section thereafter is on how to capture the flow field around the cavity and tower with a background-oriented schlieren imaging apparatus. Finally, it is described how the data were processed and how their uncertainty was estimated.

A large share of the experimental methods described in this chapter were already published previously by the author and colleagues. This includes a patent application (Siegrist (2016)), 3 conference presentations (Siegrist et al. (2017); Siegrist et al. (2018a); Stadler and Siegrist (2018)), and 2 journal articles (Stadler et al. (2017); Siegrist et al. (2018b)).

3.2.1 Experimental Setup

The experiment was conducted in the high-pressure wind tunnel Göttingen (HDG) at 6 MPa and at temperatures between 293 K and 305 K. Four different Reynolds numbers $Re = [1.5 \cdot 10^6, 3.0 \cdot 10^6, 4.5 \cdot 10^6, 6.0 \cdot 10^6]$ were covered. These numbers are calculated with respect to the cavity dimensions and the properties of the free stream. Translating these Reynolds numbers into wind tunnel wind speed gives $U_\infty \approx [6.7\,\mathrm{m\,s^{-1}}, 13.6\,\mathrm{m\,s^{-1}}, 20.5\,\mathrm{m\,s^{-1}}, 27.4\,\mathrm{m\,s^{-1}}]$. The measurements were performed with Mach numbers $Ma < 0.1$. In Table 3.2.1, the wind tunnel Reynolds numbers, the respective wind speeds, and the scaled wind speeds on the original scale are shown. The upper limit of the wind speed and hence of the Reynolds number was determined by the operating limits of the wind tunnel.

The free-stream turbulence intensity of the HDG was determined previously by Schewe (1983) to be 0.4% and by van Hinsberg et al. (2017) to be 0.8%.

The model represented approximately the upper half of a central receiver system and

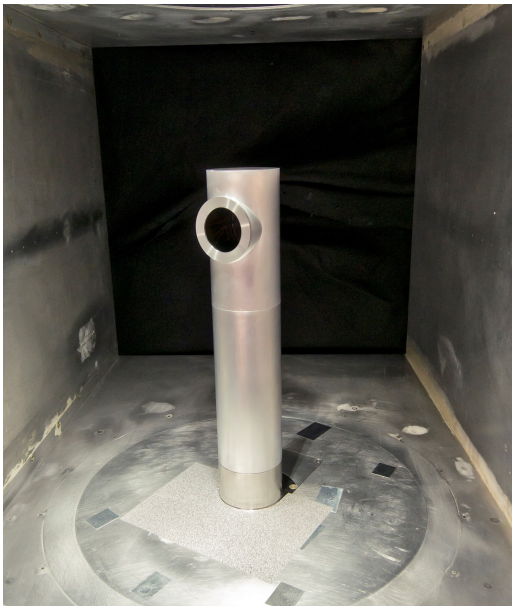

(a) Wind tunnel model with $\gamma = 0°$ mounted on a rotary table in the test section.

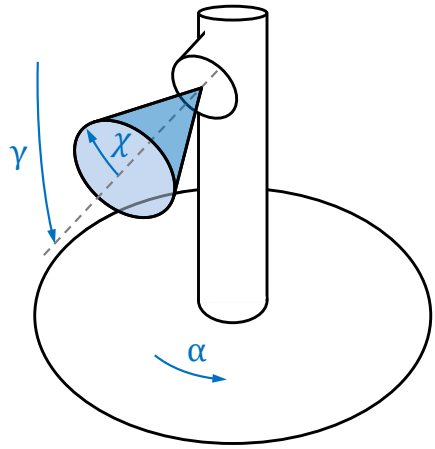

(b) Schematic drawing of a wind tunnel model with relevant coordinates. α is the wind incident angle, γ the cavity inclination angle, and χ the absolute incident angle.

Figure 3.2.1: Wind tunnel model in the test section and definition of the related coordinate system.

had a length scale of 1:250. The tower part that was exposed to the flow in the wind tunnel test section was 0.4 m high and had a diameter of 0.08 m. A piezoelectric force balance was used to attach the model to a rotary table. This force balance allowed for high frequency measurements of the fluctuating forces on the model.

The model was rotated along the *wind incident angle* α in steps of 10°. The rotary table started at $\alpha = 0°$, representing frontal winds, and rotated to $\alpha = 180°$, representing backward winds. Fig. 3.2.1a shows a picture of 1 of the geometrical configurations mounted in the test section. In Fig. 3.2.1b the definition of the used coordinate system is given. The cavity inclination angle γ is measured from the horizontal plane. The *absolute incident angle* χ is the cone angle between the incident flow and the cavity axis (grey dashed line in Fig. 3.2.1b). The test section had a cross section of $0.6\,\text{m} \cdot 0.6\,\text{m}$.

The hot-film sensors were placed on the inside of the cavity in a repeating pattern (see Section 3.2.1.1 for more details on hot-film sensors). To have a good spatial resolution and some redundancy in case of broken sensors a total of 32 sensors were placed in this regular pattern, which is shown in Fig. 3.2.2 together with the coordinate system for the cavity inside. Coordinate φ is the *azimuth coordinate* or *angular coordinate* with its origin at the top and z is the *longitudinal coordinate* starting at the inside of the aperture. Of the 32 sensors, 8 were unusable right after the installation, mainly due to installation and fabrication problems related to the limited and hardly accessible space inside the wind tunnel model. During operation no more sensors broke. The location of the working and broken sensors is shown in Fig. 3.2.2b.

An in-house CTA system was used to adjust and control the sensor heating. The absolute temperature of each sensor was adjusted in the beginning of each test day and has then been kept constant during the following test series. After adjustment of the CTA system, the system including the sensors reached a maximum cut-off frequency of around 35 kHz (see the definition of the cut-off frequency in Section 3.2.1.1). The CTA system returned an

(a) The cylindrical coordinate system in the cavity. φ is the angular and z the longitudinal coordinate.

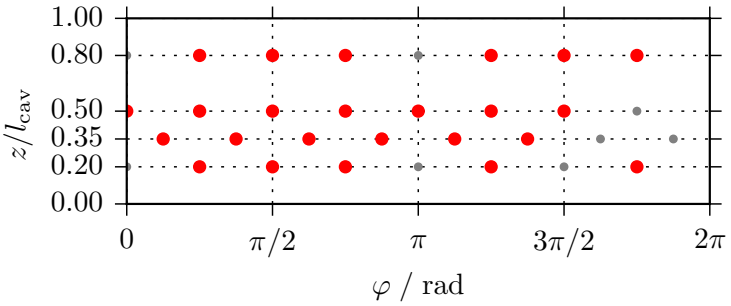

(b) Pattern of the hot-film sensors mounted on the inside of the cavity. Red large dots mark the spots of working sensors, smaller and in grey are the sensors which failed. φ and z as defined in the left subfigure.

Figure 3.2.2: Coordinate system inside the cavity and pattern of the hot-film sensors.

instantaneous voltage signal for each sensor. At each measurement point, the voltage of the CTA system was sampled for 30 s with a sample rate of 10 kHz. Flow frequencies, e.g. due to vortex shedding, were expected to be in the order of 100 Hz. Thus, the sample rate was well above the Nyquist rate.

The recorded voltage data were then converted to time- and area-averaged Nusselt numbers $Nu_{\mathrm{i,aa}}$ at a specific Reynolds number, geometric configuration, and incident angle α, see Section 3.2.2 for details.

To determine the temperature change of the wind tunnel fluid an additional measurement at $\alpha = 0°$ after the completion of each incident angle series was taken. In addition, measurements without wind before and after each test series were taken to calculate the heat loss of the sensors without flow.

To check the repeatability of the measurements some configurations were measured repeatedly. These repetitions delivered the same qualitative and quantitative behavior of the data. Hence, the measurements are assumed to be repeatable.

Another check was to estimate the ratio defined in Eq. 3.2.1. The most conservative estimation of this ratio for this experiment was obtained by assuming a uniformly heated inside at sensor temperature and the lowest Reynolds number. The result of this estimation was $Gr/Re^2 < 3 \cdot 10^{-3}$.

Since the CTA system is based on the temperatures of the sensors and of the fluid it was necessary to verify that the exchange of the fluid inside the cavity to the free stream was sufficient to guarantee that

$$T_{\mathrm{cav}} = T_{\infty}. \tag{3.2.2}$$

If this condition does not hold, the exchange would not be sufficient and the energy transferred from the sensors to the fluid would heat up the fluid inside the cavity. Consequently, the sensors would measure values related to this higher, possibly unknown, cavity bulk temperature. In this work, the sufficient exchange was checked with theoretical estimations and numerical simulations. A cross-section through the flow in and around a horizontal cavity at $\alpha = 70°$ and $Re = 6 \cdot 10^6$ obtained with a CFD simulation is shown in Fig. 3.2.3. The velocity vectors and their magnitudes are indicated by arrows and colored contours, respectively. The velocity magnitude scale is limited to 20 m s^{-1} to emphasize the flow inside the cavity. It is clearly visible that there is exchange from the cavity at the up-

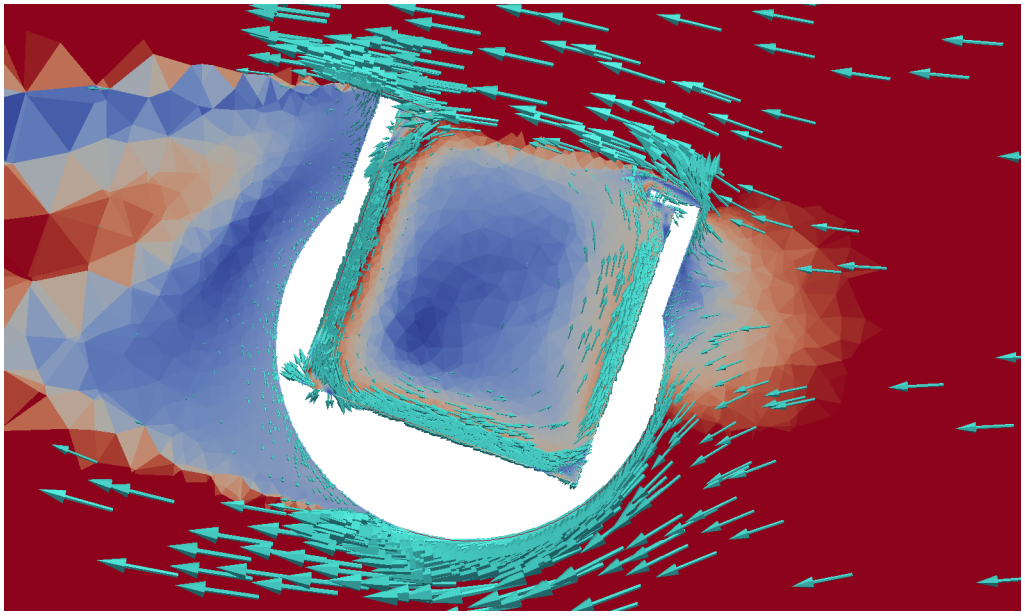

Figure 3.2.3: Horizontal cross-section through the flow in a cavity obtained with CFD. The simulated model is ($\gamma = 0°, \alpha = 70°$) at $Re = 6 \cdot 10^6$. Shown are the magnitude of the velocity in color and the velocity vectors. The velocity magnitude scale is limited to 20 m s^{-1} to emphasize the flow inside the cavity. Clearly visible is the flow out of the cavity to the surroundings at the upstream end of the aperture and the flow into the cavity at the downstream end of the aperture.

stream end of the aperture to the surroundings and to the cavity inside at the downstream end of the aperture. This suggests that there is sufficient exchange. In addition, the time series of the output voltage of the CTA was checked for drift, which could mean that the fluid temperature in the cavity had built up. No such drift was found in the measured data. Thus, it can be assumed that $T_{cav} = T_\infty$ hereafter. A second consequence of insufficient exchange could be that the sensors measure heat loss but the heat is taken up by the unheated parts of the cavity walls. This could mean that the fluid spins inside the cavity, transferring heat from the sensors via the fluid to the unheated wall parts ad infinitum. In this case, one would measure a heat loss that does not leave the cavity, which would question the transferability of the results to original scale receivers. Next to the tests already described earlier, it has to be mentioned that the cavity inside is made of an insulating plastic. This reduces the amount of heat that is transferred to the unheated parts of the cavity walls.

3.2.1.1 Ringlike Wall-Mounted Hot-Film Sensors

Hot-wire anemometry, which includes both hot-wires and hot-films, is a proven measurement technique (Bellhouse and Schultz (1966); Comte-Bellot (1976); Lomas (1986)). The basic principle is that a thin elongated metal piece gets heated by Joule heating and thus transfers heat to the surrounding fluid. With a control unit the amount of heating can be adjusted and the transferred heat can be determined. This technique is most often used for measuring fluid velocity or wall shear stress. But, it can also be used to measure the wall heat flux. Wall-mounted hot-film sensors have been used to measure the local time-resolved heat flux in several experiments, see the work of O'Donovan et al. (2011) for a thorough summary.

In hot-wire anemometry, the correlation of resistance R and temperature T is assumed to be linear, which is true under reasonable assumptions (Lomas (1986)). This correlation

can then be written as

$$R(T_w) = R(T_{ref})(1 + \alpha_0(T_w - T_{ref})), \tag{3.2.3}$$

where α_0 is the *temperature coefficient of resistance*. It follows that if R and α_0 are known the temperature can be calculated. The temperature coefficients in this work were measured for each sensor individually, as described in Section 3.2.1.2.

By knowing the resistance of the sensor at a reference temperature and under operating conditions, we can obtain an important relation, called the *overheat ratio*

$$X_{oh} = \frac{R(T_w)}{R(T_{ref})}. \tag{3.2.4}$$

In this work, the overheat ratio was kept constant at $X_{oh} = 1.3$, which gives a temperature difference between the fluid and the sensor of roughly 100 K.

All hot-wire anemometry systems work with sensors connected in a Wheatstone bridge. Depending on which of the 3 possible operational modes (constant temperature, constant current, constant voltage) is applied, this Wheatstone bridge is controlled differently. Here, the constant temperature mode was used. In CTA, the electronic control unit senses the differential voltage across the 2 branches of the Wheatstone bridge and adjusts the current with a feedback amplifier. If the fluid flows faster and therefore takes up more heat the amplifier injects a higher current to keep the resistance constant. The bridge voltage, which is the output quantity of a CTA, rises accordingly.

A typical hot-wire sensor is approximately 1 mm long and a few micrometers thick. A typical hot-film sensor is of the same length but is 1 or 2 orders of magnitude thicker if produced in cylindrical form. If the hot-film sensor is produced on a flat surface it has typically a similar length, a length-to-width ratio of 10 and a thickness of approximately 0.2 µm. It becomes clear, that the thermal inertia of such small sensors is very low. Together with the fast electronic control circuitry cut-off frequencies of up to 100 kHz can be reached. The cut-off frequency is defined as the inverse of the time the bridge voltage needs to adjust to $1/e \approx 0.368$ of the peak value after a square-wave stimulation.

The advantages of a hot-film anemometry setup can be generalized to: (i) the high spatial resolution and (ii) the high temporal resolution. The first allows for a local resolved heat flux map and the second allows for fluctuation analysis and fast experimental measurements. Therefore, in this work wall-mounted hot-film sensors were used to measure the local time-resolved heat flux.

On a heated element on a surface we can balance the energy provided to the element by the control circuit with the total dissipated energy. In other words, the heat dissipated in a sensor $\dot{Q}_s$ equals the electrical power of a sensor $P_{s,el}$, which is a function of the sensor voltage E_s and the sensor resistance at operating temperature $R(T_w)$, see Lomas (1986):

$$\begin{aligned} \dot{Q}_s = P_{s,el} &= \frac{E_s^2}{R(T_w)} \\ &= \dot{Q}_{s,conv,mix} + \dot{Q}_{s,rad} + \dot{Q}_{s,cond\to supp} + \dot{Q}_{s,cond\to lead}. \end{aligned} \tag{3.2.5}$$

Under any conditions, this power is the sum of the mixed convective heat loss $\dot{Q}_{s,conv,mix}$, the radiative heat loss $\dot{Q}_{s,rad}$, the conductive heat loss to the support material $\dot{Q}_{s,cond\to supp}$ and the conductive heat loss to the leads $\dot{Q}_{s,cond\to lead}$. The latter 3 remain constant for a constant sensor temperature and under steady-state operation. When not in the mixed convection regime, $\dot{Q}_{s,conv,mix}$ is either dominated by the free convective heat flow $\dot{Q}_{s,conv,free}$ if

$Gr \gg Re^2$ or by the forced convective heat flow $\dot{Q}_{\mathrm{s,conv,forc}}$ if $Gr \ll Re^2$. This fact is formalized in the following equation

$$\dot{Q}_{\mathrm{s,conv,mix}} = \begin{cases} \dot{Q}_{\mathrm{s,conv,free}} & \text{if } Ri \gg 1\,. \\ \dot{Q}_{\mathrm{s,conv,forc}} & \text{if } Ri \ll 1\,. \end{cases} \tag{3.2.6}$$

The terms in Eq. 3.2.5 were calculated with conservative estimations, see Appendix E. The outcome is the following relation

$$\dot{Q}_{\mathrm{s,cond\to supp}} \approx 0.05\,\mathrm{W} \gg \dot{Q}_{\mathrm{s,conv,free}} \gg \dot{Q}_{\mathrm{s,rad}} \gg \dot{Q}_{\mathrm{s,cond\to lead}}\,. \tag{3.2.7}$$

The heat dissipated to the support material matched roughly the typical power measured in a sensor under no-wind conditions which was $P_{\mathrm{s,el,calm}} \approx 0.07\,\mathrm{W}$. Thus, it was deduced that the estimated orders of magnitude for the terms in Eq. 3.2.5 may be taken as correct. With wind, the typical power $P_{\mathrm{s,el,wind}}$ was roughly 0.01 W to 0.2 W higher than $P_{\mathrm{s,el,calm}}$. A consequence of Eq. 3.2.7 is $\dot{Q}_{\mathrm{s,conv,free}} \ll \dot{Q}_{\mathrm{s,cond\to supp}}$. Considering also the consequence of Eq. 3.2.1 that $\dot{Q}_{\mathrm{s,conv,forc}} \gg \dot{Q}_{\mathrm{s,conv,free}}$, it can be stated that the additional heat loss that occurs with wind is only due to forced convection. Therefore, the forced convective heat loss $\dot{Q}_{\mathrm{s,conv,forc}}$ can be obtained by taking the difference of the power at a measurement point with wind and the power at a measurement point without wind, see Section 3.2.2 for more details.

The energy balance in Eq. 3.2.5 can also be written in a nondimensional form as (McCroskey and Durbin (1972))

$$Nu_{\mathrm{s}} = A + BPr^{m}Re^{n}\,, \tag{3.2.8}$$

where A is a constant that incorporates $\dot{Q}_{\mathrm{s,conv,free}}$, $\dot{Q}_{\mathrm{s,rad}}$, $\dot{Q}_{\mathrm{s,cond\to supp}}$, and $\dot{Q}_{\mathrm{s,cond\to lead}}$. B is another constant. In order to obtain accurate absolute values an in-situ calibration has to be made to find these 2 empirical constants. The exponents m and n are defined as 1/3 and 2/3 respectively. In this formula the Reynolds number is based on the friction velocity. All fluid properties are evaluated at the film temperature.

Let us now consider only the additional contribution to Nu_{s} due to forced convection

$$Nu_{\mathrm{s,conv,forc}} = BPr^{1/3}Re^{2/3} = BPr^{1/3}\left(\frac{\rho u_\tau l}{\mu}\right)^{2/3}\,. \tag{3.2.9}$$

In short, we can approximate the relationship between the additional forced convective heat transfer and the only varying quantity u_τ, or τ_{w} after using the definition of the friction velocity in Eq. 2.5.5, as

$$Nu_{\mathrm{s,conv,forc}} \propto \tau_{\mathrm{w}}^{1/3}\,. \tag{3.2.10}$$

Conventional hot-film sensors are of straight design. This makes them heavily dependent on the incident angle of the flow (Lomas (1986); Tropea et al. (2007)). This dependency can be analyzed via the cosine law (Eq. 3.2.11), which states that only the sensor-normal component is effective in transferring thermal energy from the sensor to the fluid.

$$U_{\mathrm{eff}} = U_\infty \cos(\beta) \quad \text{or} \quad \tau_{\mathrm{w,eff}} = \tau_{\mathrm{w}} \cos(\beta)\,, \tag{3.2.11}$$

where β is the angle between the sensor normal and the flow direction. The underlying assumption is that the sensor length is much larger than the sensor width and therefore the width vanishes. As McCroskey and Durbin (1972) showed, we can plug this in Eq. 3.2.10 and obtain the dependency of the sensor on the main flow direction β

$$Nu_{\mathrm{s,conv,forc}}(\beta) \propto \cos(\beta)^{1/3}\,. \tag{3.2.12}$$

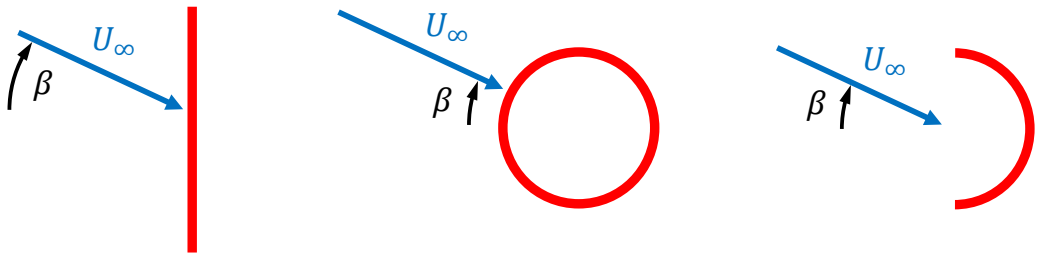

Figure 3.2.4: Top view of schematic drawings of a conventional straight hot-film sensor and 2 new design proposals that could reduce the dependency on the flow direction: a perfect ringlike sensor (center) and a half-open ringlike sensor (right). The main flow direction is indicated by the velocity vector (blue arrow) and β.

From this relation follows that the sensor output voltage varies between the maximum value at perpendicular flows and zero when the flow direction is aligned with the sensor. Normally, this is not a big issue because the main flow direction is known and the sensors are aligned accordingly, for example in a flow across a wing profile or a bluff body. However, in complex flows such as internal flows in a cavity the main flow direction cannot be known a priori.

By considerations of symmetry, based on the above cosine law, it can be deduced that for a perfect *ringlike sensor* the direction dependency should disappear. This should also apply to a ringlike sensor in the form of a half-ring. These 2 new designs are drawn schematically in Fig. 3.2.4 together with a conventional straight sensor.

Until now, the considerations were based on the assumption that the sensor width can be neglected. In this case, one would opt for the half-open ringlike sensor because it is very easy to connect the leads to such a sensor. For a real sensor, one also has to take into account that due to the heat dissipation into the substrate the effective sensor area may be larger than the actual sensor area (Beasley and Figliola (1988)). This effect favors the perfect ringlike sensor because the effective sensor area forms a more symmetric shape which maintains the direction independency.

Consequently, a ringlike wall-mounted hot-film sensor was designed to reduce the angular dependency in this work. The design and parts of the methodology were already published by the author in Siegrist (2016) and Siegrist et al. (2017). To demonstrate the benefits of this new design the direction dependency stated in Eq. 3.2.12 was quantified for different sensor designs. To do this the sensor was discretized in infinitesimal parts, as depicted in Fig. 3.2.5, and for each of the infinitesimal pieces the contribution to the total heat transfer was calculated to be

$$dNu_{\mathrm{s,conv,forc}}(\delta) = dNu_{\mathrm{s,conv,forc}}(\beta - \omega') = \left| C \cos\left(\beta - \omega'\right)^{1/3} \right| d\omega', \tag{3.2.13}$$

where C is a constant for a given velocity that lumps all quantities which are not dependent on the main flow angle and $\delta = \beta - \omega'$ is the relative incident angle on an infinitesimal length, depending on the angular location ω'. A numerical integration with the trapezoidal rule and $\mp\omega/2$ as the boundaries was carried out to obtain the integral for each sensor. The sensor angle ω describes the angle of the ringlike part of the sensor and is indicated by the red arc in Fig. 3.2.5. The integrations for a selection of main flow directions β between a half-ring ($\omega = \pi$) and a full-ring ($\omega = 2\pi$) are shown in Fig. 3.2.6.

It is evident that the half-open and the perfect ringlike sensors perform best and that the straight sensor performs worst in terms of directional sensitivity. The difference in

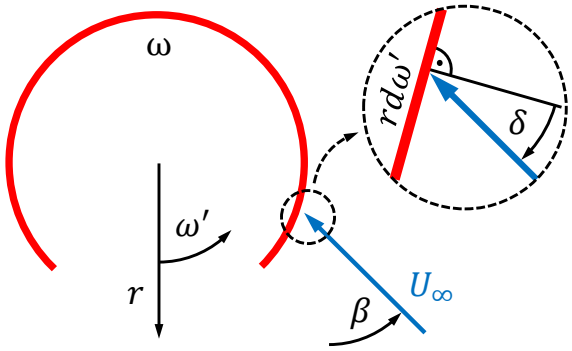

Figure 3.2.5: Infinitesimal contribution dNu_s to the total forced convective heat transfer. ω is the sensor angle indicated by the red arc, ω' the angular coordinate, δ the relative incident angle between the arc normal and the flow direction (blue arrow), and β the main flow direction.

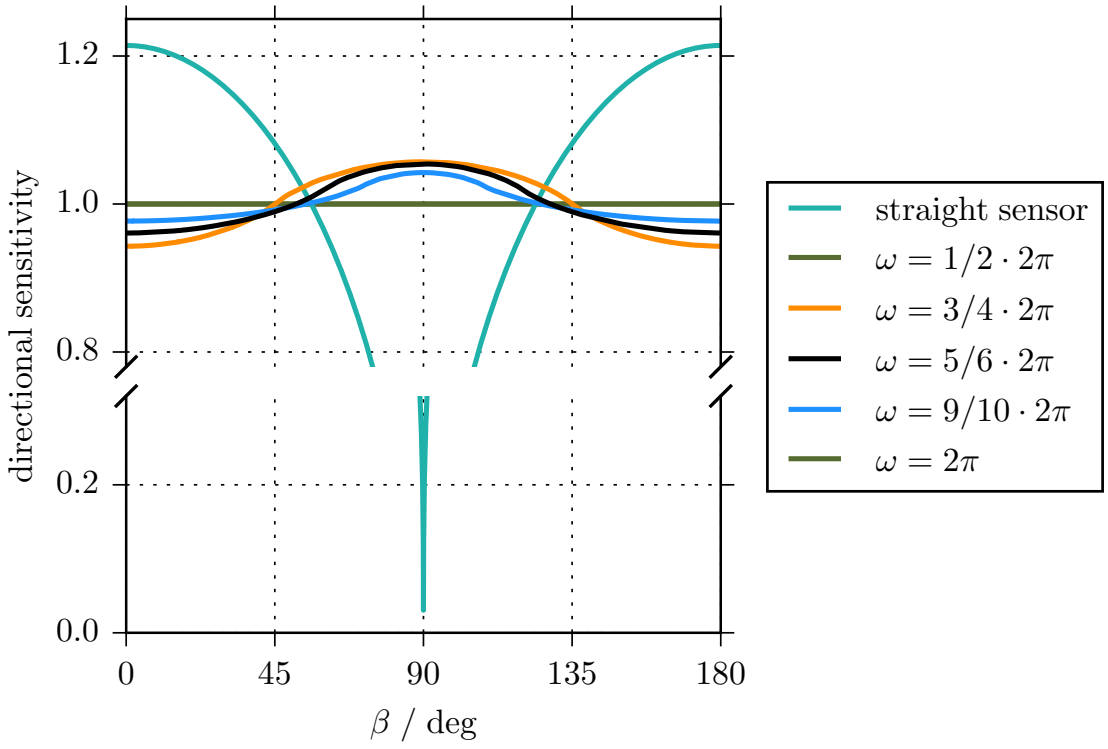

Figure 3.2.6: Directional sensitivity plotted versus main flow direction β. In this work the sensor angle ω is $5/6 \cdot 2\pi$. Each curve is scaled to have its average at 1. Perfect directional independency is achieved for sensors with half-open ($\omega = \pi$) and perfect ($\omega = 2\pi$) ringlike shapes, which are both plotted in green.

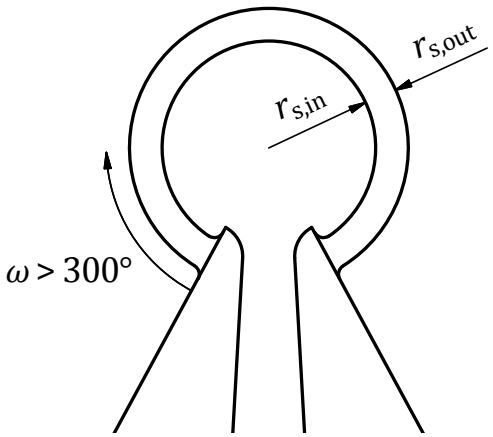

Figure 3.2.7: Top view of the final design of the ringlike wall-mounted hot-film sensor used in this work. The tapered objects reaching from below are the 2 leads. The relative dimensions are to scale.

sensitivity for the sensors between a half-ring and full-ring becomes smaller the larger ω becomes. Due to the heat conduction in real sensors it is expected that this comparison will be blurred out somewhat depending on the sensor temperature and the conductivity of the substrate. The sensor design used in the present experiment has a sensor angle of approximately $5/6 \cdot 2\pi$ which is represented by the black line in Fig. 3.2.6. This angle was the maximum permitted by the fabrication process.

The final design of the ringlike sensor is presented in Fig. 3.2.7. The inner and outer radii were 0.327 mm and 0.427 mm, respectively, which give a path length of 2 mm at the centerline. The sensing element was made of electron beam deposited nickel with a thickness of 0.20 µm. The leads, which can be seen in the bottom of Fig. 3.2.7, were made of copper and had a width of 0.508 mm and a thickness of 12.7 µm. Multiple sensors were fabricated in a pattern on a thin polyimide film of 50 µm thickness. These sensor arrays were then glued on the inside of the cavity to a base of 2 mm thick polyoxymethylene (POM). The regular pattern produced by this procedure is shown in Fig.3.2.2b.

After production, the sensors had a resistance in the range of 9.1 Ω to 9.7 Ω. The sensor leads were led through slits in the back of the cavity. The slits were sealed with isolating epoxy resin to close the back of the cavity. Figure 3.2.8a shows the mounted sensor arrays in the cavity. On the outside of the back of the cavity, which is still inside the tower, the sensor leads were soldered to shielded twisted pair cables that led to the air lock door of the wind tunnel. From there, a standard coaxial cable was used to connect to the CTA system. In Fig. 3.2.8b the soldered leads and twisted pair cables are shown after they have been fixated by a thick layer of epoxy resin.

3.2.1.2 Temperature Coefficient of Resistance

The values of the temperature coefficient of resistance α_0 were determined by a separate measurement with the actual sensors after the wind tunnel tests. All sensors including the cavity were placed in a drying cabinet. The temperature was raised in steps of maximum 5 K from 297 K up to 333 K. Once thermal equilibrium was reached at each step, the resistances were measured. Thereafter, the data were fitted by a linear regression to obtain α_0 for each sensor. In Table 3.2.2 the resulting temperature coefficients of resistance for all working sensors are listed together with their corresponding sensor positions.

The median value of the temperature coefficient of resistance of $3.281 \cdot 10^{-3}\mathrm{K}^{-1}$ is in the

Table 3.2.2: Measured temperature coefficient of resistance α_0 for each of the working sensors.

Sensor position		Temperature coefficient of resistance
φ / °	z / l_{cav}	α_0 / (10^{-3} K^{-1})
0	0.5	3.645
22.5	0.35	3.163
45	0.2	3.578
45	0.5	3.538
45	0.8	3.578
67.5	0.35	3.408
90	0.2	3.421
90	0.5	2.919
90	0.8	3.424
112.5	0.35	3.178
135	0.2	3.289
135	0.5	3.175
135	0.8	2.832
157.5	0.35	2.765
180	0.5	3.110
202.5	0.35	3.084
225	0.2	3.230
225	0.5	3.317
225	0.8	3.239
247.5	0.35	3.565
270	0.5	2.634
270	0.8	3.272
315	0.2	3.417
315	0.8	3.300
Median		3.281

(a) The 32 sensors sit at the visible end of the thick coppery leads of the sensors, which are leading out through thin slits in the back of the cavity.

(b) Backside of the cavity. The 64 sensor leads are soldered to twisted pair cables and fixated by epoxy resin.

Figure 3.2.8: The cavity with the mounted sensors (left) and their connections to the signal cables at the back of the cavity (right).

range that was confirmed by private communication with the manufacturer (Tao Systems (2016)). The values are almost half of those for bulk nickel. This is due to the different material properties when Nickel is electron beam deposited. Another manufacturer of hot-film sensors report values for sputtered nickel in the range of 60% to 80% of the tabulated value for bulk material (DANTEC (2018)). The temperature coefficients of resistance for the sensors in the present work are therefore similar to the values for standard, straight sensors.

3.2.1.3 Geometrical Configurations

To perform the measurements in a short time and to change the geometry easily a modular model was designed. Two geometrical parameters, the cavity inclination angle γ and the aperture ratio X_{ap}, were varied. Three cavity inclination angles $\gamma = [0°, 30°, 60°]$ and 3 aperture ratios $X_{\mathrm{ap}} = [1.0, 0.8, 0.6]$ were tested. Both, the inclination angles and the aperture ratios were chosen based on typical values of large commercial cavities and previous studies, see Section 3.1 for details. The 3 aperture ratios were tested with an inclination $\gamma = 30°$ in order to be comparable to a previous study by Flesch et al. (2015). The 3 inclination angles were tested with an aperture ratio $X_{\mathrm{ap}} = 0.8$. See Fig. 3.2.9 and Fig. 3.2.10 for images of the tested geometrical configurations, respectively. The geometrical configurations in Fig. 3.2.9b and Fig. 3.2.10b are identical. In Appendix A detailed drawings of important parts of the wind tunnel models are shown.

(a) $\gamma = 0°$ **(b)** $\gamma = 30°$ **(c)** $\gamma = 60°$

Figure 3.2.9: Wind tunnel model with 3 cavity inclination angles γ and an aperture ratio $X_{ap} = 0.8$.

(a) $X_{ap} = 1.0$ **(b)** $X_{ap} = 0.8$ **(c)** $X_{ap} = 0.6$

Figure 3.2.10: Wind tunnel model with 3 aperture ratios X_{ap} and a cavity inclination angle $\gamma = 30°$.

The cavity with the hot-film sensors was reused for all geometrical configurations. It had an inner diameter $d_{cav} = 0.06\,m$ and a length-to-diameter ratio $l_{cav}/d_{cav} = 1$.

The tower and the outer parts of the cavity were made of aluminium. Inside the tower there was space to guide the cables from the back of the cavity out of the model. The model was kept in place by a long screw inside the tower which was turned in the head part of the model.

From the geometrical data a solid blockage of between 8.8% and 10.0% was calculated. According to the best practice published in Barlow et al. (1999), the solid blockage should be at maximum 10%.

3.2.1.4 Reduction Measures

One of the 3 goals of this work is to analyze convective heat loss reduction measures. In the framework of a previous doctoral thesis (Flesch (2016)), a DLR-internal workshop on reduction measures was conducted to gather a wealth of reduction measures. Such reduction measures can for example be active measures, such as an aerowindow induced by an air jet or suction and injection of hot or cold air inside the cavity. They can also be passive measures, such as porches in front of the cavity or quartz windows. The instrumentation for active measures was too complex in the setting of a high-pressure wind tunnel. Therefore, only passive measures were considered. These passive measures can either be applied in front of the aperture to influence the flow locally or at or around the tower to influence the flow more globally. The first measurements showed a very high dependency of the forced convective heat loss for wind incident angles $\alpha \leq 90°$. Thus, measures at the tower were not expected to deliver any remarkable reduction. As a consequence, the reduction measures were focused on passive measures in vicinity of the aperture.

Three reduction measures were designed, each having a different means of reducing the convective heat loss:

- Solid porch with the intention to block the momentum of the flow in front of the aperture.
- Porous porch with the intention to reduce the momentum in the flow in front of the aperture.
- Aerodynamic porch with the intention to deflect the flow in parallel to the aperture.

These reduction measures were built for the cavity with an aperture ratio $X_{ap} = 0.8$ and were tested with a cavity inclination angle $\gamma = 0°$. In Fig. 3.2.11, the 3 tested reduction measures are presented.

The solid porch was made of aluminium, had a cone angle of 45°, and protruded the aperture by 11 mm. The porous porch was made of a porous steel foam with the same outer dimensions as the solid porch. It was glued onto the aperture. The aerodynamic porch, or more correct the aerodynamically shaped porch, was made of aluminium. The shape is a curved wing profile which is rotated around the cavity cylinder axis and has small passages at the base. The outer dimensions were similar to the other 2 porches.

In the case of the porous porch, an in-depth design was done in order to establish similarity of the porous model (subscript M) with the original scale (subscript O). To achieve this the dimensionless pressure drop or resistance coefficient k_r (McNaughton (1988); Liu et al. (2014)) across the porous structure has to be maintained

$$k_{r,M} = k_{r,O} \quad \Longrightarrow \quad \frac{\Delta p_M}{1/2 \rho_M U_M^2} = \frac{\Delta p_O}{1/2 \rho_O U_O^2}\,. \tag{3.2.14}$$

(**a**) Solid porch (**b**) Porous porch (**c**) Aerodynamic porch

Figure 3.2.11: Wind tunnel model with the 3 tested reduction measures. The aperture ratio was $X_{ap} = 0.8$ and the cavity inclination was $\gamma = 0°$.

By an order of magnitude analysis for the case under investigation it was found that

$$\frac{\Delta p_{\mathrm{M}}}{\Delta p_{\mathrm{O}}} = \mathcal{O}\left(10^3\right). \tag{3.2.15}$$

In Wilson (1987) and Heisler and DeWalle (1988) the most effective range of the resistance coefficient is given as $k_{\mathrm{r}} \approx [2,\ldots,5]$. With this we can calculate the absolute pressure drop from Eq. 3.2.14 and plug it in the *Forchheimer's equation* (Scheffler and Colombo (2005))

$$-\frac{dp}{dx} = \frac{\mu}{k_1} U_{\mathrm{s}} + \frac{\rho}{k_2} U_{\mathrm{s}}^2, \tag{3.2.16}$$

where k_1 is the Darcian permeability, k_2 the non-Darcian permeability, and U_{s} the superficial velocity. $1/k_2$ is also called the *Forchheimer coefficient*. In this work k_{r} was chosen to be 2. This results in a desired Forchheimer coefficient of roughly $200\,\mathrm{m}^{-1}$. The experimentally determined Forchheimer coefficient of the used metallic foam was approximately $400\,\mathrm{m}^{-1}$ which is deemed satisfactory, regarding the further unknowns such as the influence of pore geometry or pore density.

3.2.1.5 Background-Oriented Schlieren Imaging

In order to obtain more information on the flow field around the cavity of the model, a *background-oriented schlieren (BOS)* imaging setup was applied. With a BOS imaging setup one may visualize density gradients in a transparent fluid by comparing the instantaneous background pattern to a reference background pattern. The measurement principle bases on the correlation of the index of refraction n with density as formulated by the *simplified Gladstone-Dale relationship*

$$n - 1 = k\rho, \tag{3.2.17}$$

where k is the Gladstone-Dale constant. This means if the density changes the index of refraction changes, too. This leads to a deflection angle ξ in direction x_i which can be found by integration along the line of sight l

$$\xi_{x_i} = \frac{k}{n}\frac{\partial}{\partial x_i}\int dl. \tag{3.2.18}$$

For every measurement point, that is a given combination of Reynolds number, wind incident angle α, and geometrical configuration, a series of 500 images has been taken at a sampling rate of 150 Hz which is about 1.5 times the expected vortex shedding frequency of the cylindrical section of the model. However, within a previous study (Stadler et al. (2017)) no periodic fluctuations could be identified in the BOS analysis, thus for the current investigation no influence of the vortex street was expected.

In general, the BOS method may deliver qualitative and quantitative results. The theory, setup and data processing for an infinite cylinder in a high-pressure and low *Ma* environment were first introduced by Stadler et al. (2017). In the present work, the method was adapted to a finite cylinder with a cavity. A selection of results was published by Stadler and Siegrist (2018).

3.2.2 Data Processing

Equation 3.2.5 shows the relation between the electrical power delivered instantaneously to the sensor and the total heat dissipated. As reasoned in Section 3.2.1.1, the difference of power, which is needed to keep a sensor at the desired operating temperature with wind

$P_{s,el,wind}$ and to keep the same temperature but without wind $P_{s,el,calm}$, equals the additional instantaneous power transported away from the sensor by forced convection $\dot{Q}_{s,conv,forc}$ as

$$\Delta P_{s,el} = P_{s,el,wind} - P_{s,el,calm} = \dot{Q}_{s,conv,forc}\,. \tag{3.2.19}$$

The instantaneous power values were then averaged over the whole sample period to give the average additional power $\overline{\Delta P_{s,el}}$. If the condition given in Eq. 3.2.2 holds, the average power can be nondimensionalized via the following Nusselt number expression

$$Nu_s = C_{geo}\frac{\overline{\Delta P_{s,el}}}{k_{air}\Delta T}\,, \tag{3.2.20}$$

where C_{geo} is a constant which incorporates characteristic geometrical parameters from both sensor and cavity, ΔT the temperature difference between sensor operating temperature T_w and cavity bulk temperature T_{cav}, and k_{air} the thermal conductivity of air at film temperature T_{film}. The geometrical constant is expressed as

$$C_{geo} = \frac{L}{A_s} = \frac{2L}{\omega(r_{s,out}^2 - r_{s,in}^2)}\,, \tag{3.2.21}$$

where $L = l_{cav}$ is the characteristic length of the cavity, A_s the characteristic sensor surface area, ω the sensor angle, and $r_{s,out}$ and $r_{s,in}$ the outer and inner radii of the sensor, respectively.

Here, the representation of measured data by the Nusselt number is convenient because it already incorporates temperature changes of the fluid during measurements (Eq. 3.2.20). Thus, a separate correction for fluid temperature changes becomes obsolete.

In the second to last step, the Nusselt numbers of all sensors were interpolated on the inner cylindrical surface to give an interpolated Nusselt number $Nu_i(\varphi, z)$. It was assumed that in the corner between the aperture and the cylindrical surface as well as in the corner between the back of the cavity and the cylindrical surface no convective heat transfer takes place. This is a reasonable assumption because in the corners the velocity gradient normal to the surface vanishes and so does the advective heat transport. Due to this assumption, the interpolation can also be carried out on the cylindrical surface with $0 < z < 0.2$ and $0.8 < z < 1$. A cubic spline interpolation was used.

As shown in Fig. 3.2.2b, the sensors were only mounted on the cylindrical part of the cavity, no sensors were mounted on the back of the cavity. This introduces an uncertainty if one wants to draw conclusions about the forced convective heat loss from the measured data for the case of a cavity where the back is also heated. The uncertainty can be estimated on the basis of CFD simulations, see Section 3.3.9 for more details.

The last step of the data processing was to area-average the interpolated values to give 1 integral value $Nu_{i,aa}$ per combination of Reynolds number, geometrical configuration, and incident angle.

This interpolation process is demonstrated in Figs. 3.2.12a and 3.2.12b. The first figure shows the iteration-averaged local Nusselt number that was obtained from CFD simulations of the geometrical configuration ($\gamma = 0°, X_{ap} = 0.8, \alpha = 70°$) at $Re = 6 \cdot 10^6$. This figure represents the locally resolved flow which is a priori unknown in this work. The second figure represents the interpolation of the measurements on the cylindrical surface of the cavity, as it was done in this work. It is clearly visible that the data processing method captures the main qualitative flow effects well. To validate this process quantitatively probes of the iteration-averaged local Nusselt number, obtained with CFD, were taken at the locations of the working sensors and were then interpolated with a cubic spline method on the

Table 3.2.3: The uncertainty of a selection of quantities evaluated with the procedure proposed in the GUM:1995 (ISO (2008)). In the second column it is indicated whether the uncertainty is given in absolute (Abs) or relative (Rel) form. The uncertainty is stated as standard uncertainty.

Factor of uncertainty	Symbol	Form	Standard uncertainty
Wind speed	U_∞	Rel	max. $1.96 \cdot 10^{-3}$
Fluid temperature	T_∞	Rel	max. $4.04 \cdot 10^{-4}$
Fluid pressure	p_∞	Rel	max. $2.31 \cdot 10^{-4}$
Fluid thermal conductivity	k_{air}	Rel	$1.50 \cdot 10^{-2}$
Reynolds number	Re	Rel	max. $3.06 \cdot 10^{-3}$
Wind incident angle	α	Abs	0.294°
Model dimensions	l_{cav}, d_{cav}	Abs	max. $3.88 \cdot 10^{-5}$ m
Sensor dimensions	r_{s}, ω	Abs	max. $7.76 \cdot 10^{-10}$ m
Sensor location	φ, z	Abs	1.16°
Temperature coefficient of resistance	α_0	Rel	max. $2.35 \cdot 10^{-2}$
Sensor resistance at reference	$R(T_{\text{ref}})$	Rel	$1.73 \cdot 10^{-2}$
Cable resistance at reference		Rel	$2.89 \cdot 10^{-2}$
Wheatstone resistance	R_1	Rel	$5.77 \cdot 10^{-3}$
CTA output voltage	E_{s}	Rel	max. $3.65 \cdot 10^{-4}$
Sensor direction dependency		Rel	$1.90 \cdot 10^{-2}$

cylindrical part of the cavity, see Fig. 3.2.12b. Finally, the local Nusselt numbers were area-averaged to give 1 integral value each for the locally resolved data from CFD simulations (Nu_{aa}) and the interpolated data based on point values from CFD simulations ($Nu_{\text{i,aa}}$). The ratio $Nu_{\text{i,aa}}/Nu_{\text{aa}}$ was calculated for the 3 interpolation methods nearest, linear, and cubic which resulted in 0.70, 0.68, and 0.75, respectively. The difference between these values and the "correct" value is explained due to the limited number of sensors and hence the discrete spatial resolution of the sensor array, which limits the ability to capture the gradients at $z \approx 0$ and $z \approx 1$ correctly. Since the cubic interpolation comes closest to the "correct" value, this interpolation method is chosen for this work.

3.2.3 Uncertainty Estimation

The uncertainty for the presented wind tunnel measurements was evaluated with the procedure proposed in the GUM:1995 (ISO (2008)). This means that for every quantity that introduces uncertainty in the measurements a standard uncertainty was calculated. In Table 3.2.3, the standard uncertainty of a selection of quantities is shown. The relevant standard uncertainties were then combined and expanded by a coverage factor of 3 to give the reported *expanded uncertainty* at the 3σ level.

In Section 4.1, the detailed expanded uncertainty is presented. The maximum relative uncertainty of the dimensionless forced convective heat loss is 8.2%. This helps to relate the order of magnitude of the standard uncertainty reported in Table 3.2.3. Of the tabulated absolute uncertainty, the model and sensor dimensions have a very small uncertainty and are therefore not considered in the combined uncertainty.

Although, the absolute uncertainty of the wind incident angle might appear considerable at first sight, it is expected that it does not contribute considerably to the final measurement uncertainty. This is because the expanded uncertainty of the wind incident angle is still more than 1 order of magnitude below the selected increments in α between 2 measurement points, see Section 3.2.1. Where relevant, the expanded uncertainty of the wind

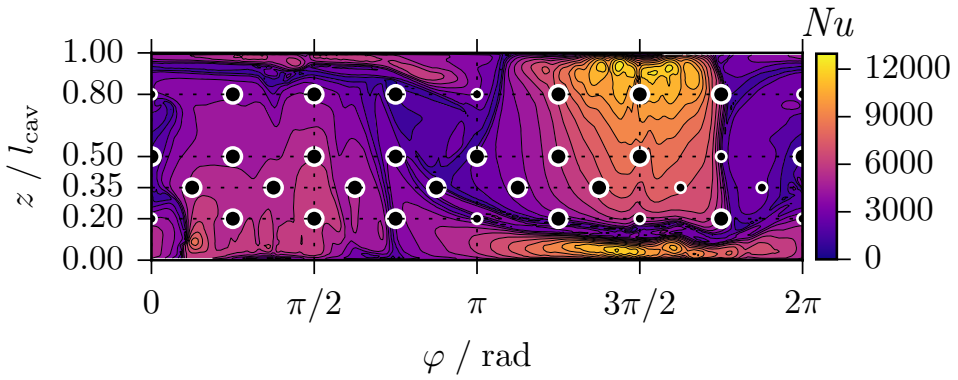

(a) Iteration-averaged locally resolved *Nu* on the cylindrical surface of the cavity calculated with CFD.

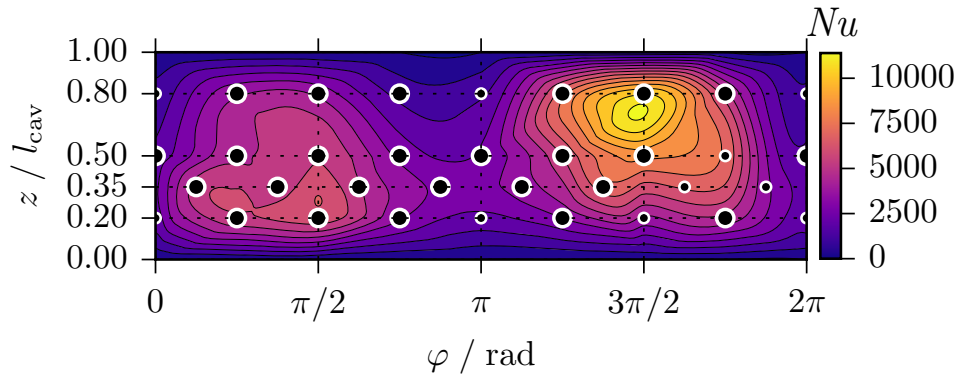

(b) Interpolated *Nu* on the cylindrical surface of the cavity. The values of the CFD simulation at the working sensor locations were taken and interpolated with a cubic spline method.

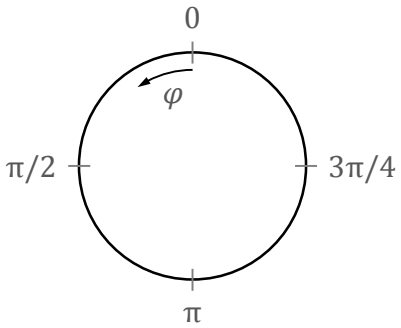

(c) Front view of the cavity and the relevant angular coordinate φ.

Figure 3.2.12: Comparison of (a) the actual local Nusselt number *Nu* calculated with CFD and (b) the interpolated local *Nu* on the basis of the point values at the working sensor locations. The simulated configuration is ($\gamma = 0°, X_{ap} = 0.8, \alpha = 70°, Re = 6 \cdot 10^6$). Large dots represent the working sensors, small dots represent the broken sensors. Subfigure (c) indicates the angular coordinate φ.

incident angle is indicated when presenting the results throughout Chapter 4.

The sensor location is actually not an uncertainty, but a systematic error of the setup, because it is measured and remains constant for all geometric configurations. During the present investigation, there was no means to quantify the effect of this location error on the final results. Hence, it was impossible to correct the measurements for this error. But, CFD simulations show that the spatial fluctuations are such that they can still be captured with the present sensor location error, see Fig. 3.2.12a. Consequently, the effect of this error is neglected.

The relative uncertainty can be classified according to its order of magnitude. In Table 3.2.3, the uncertainty ranges in between of $\mathcal{O}(10^{-4})$ to $\mathcal{O}(10^{-2})$. The importance is directly indicated by the order of magnitude. Thus, the uncertainty of the fluid pressure, of the fluid temperature, and of the CTA output voltage are least affecting the final measurement uncertainty. An intermediate role play the uncertainty of the wind speed, of the Reynolds number, and of the Wheatstone resistance. The most important group of uncertainty includes the thermal conductivity of the fluid, the temperature coefficient of resistance, the sensor resistance at reference, the cable resistance at reference, and the sensor direction dependency.

3.3 Numerical Methods

The most relevant fundamentals concerning a numerical solution of the investigated model were introduced in Section 2.7. Hereafter, more hands-on topics are answered: How large shall the computational domain be? What turbulence model suits this case best? What boundary and initial conditions shall be chosen? Which mesh is accurate enough but has still a good computational performance? How shall the data be processed to obtain the relevant information?

In this work, the open-source CFD code OpenFOAM v4.1 (OpenFOAM (2018a)) was used. Flesch (2016) showed that this code performs well for buoyant internal and external flows.

The full Navier-Stokes equations are solved because the Boussinesq approximation for the density variation cannot be used in these simulations. This approximation is only valid for $\Delta T \lesssim 28\,\mathrm{K}$ in air (Gray and Giorgini (1976)).

3.3.1 Computational Domain

Typically, *computational domains* are given in multiples of the characteristic dimensions of the model, such as its height H or its diameter D. A schematic drawing of the computational domain with the names of the boundaries is shown in Fig. 3.3.1.

The computational domain in the case of the wind tunnel model is modeled in width and height according to the real test section which was $1.5H \cdot 1.5H$ with $H = 0.4\,\mathrm{m}$. The upstream part was chosen to be $2H$ which is needed to let the flow develop before it hits the model. The downstream part was chosen to be $5H$ which is needed to let the flow vortices relax enough to prevent backflow at the outlet. This resulted in the same solid blockage as for the experiment, this means at maximum 10%, see Section 3.2.1.3.

In the case of the original scale model, the domain was chosen to be $6H$ wide and $4H$ high. It had an upstream domain length of $3H$ and a downstream domain length of $7H$ with $H = 80\,\mathrm{m}$. This enlarged domain was needed to reduce the effects of the lateral bounds. The solid blockage was hereby reduced to about 1%.

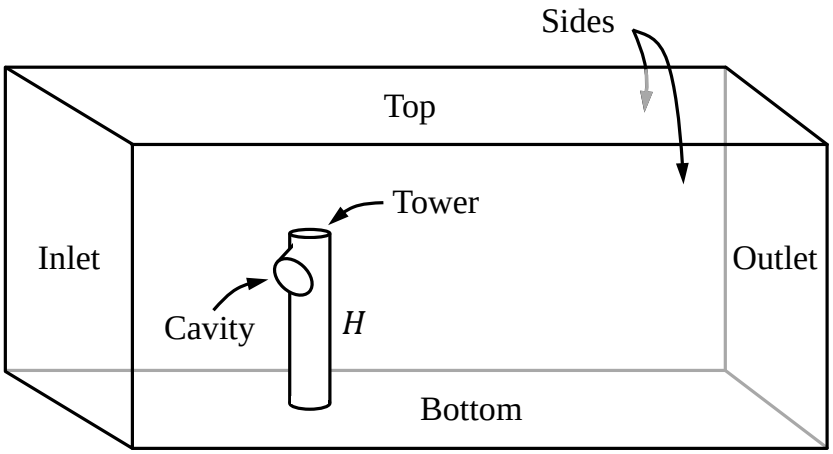

Figure 3.3.1: Schematic drawing of the computational domain including the names of the boundaries. The height of the model is symbolized by H.

3.3.2 Turbulence Modeling

As shown in Chapter 1, the flow inside the cavity is expected to be turbulent. Consequently, a turbulence model has to be selected for an accurate numerical simulation, see Section 2.7. In this work, the SST k-ω turbulence model is used because it is adequate for complex geometries and buoyant flows (Flesch (2016)). It belongs to the 2-equation turbulence models for the RANS equations. The fundamental equations are Eqs. 2.7.10 and 2.7.11. In addition, the detailed turbulence model and its constants are given in Appendix B. For the simulations in this work, the standard turbulence model constants as implemented in OpenFOAM were used.

3.3.3 Boundary and Initial Conditions in CFD

In Section 3.1, the definition of the modeled CSTE system was given. From this, the boundary and initial conditions can be deduced. First, the detailed boundary conditions for the wind tunnel simulations are introduced. Then, the difference to the boundary conditions for the original scale simulations are explained. For an overview of the names of the boundaries, the reader is referred to Fig. 3.3.1. The precise names of the OpenFOAM wall functions and the complete set of numeric values used are given in Appendix C. In the articles by Kalitzin et al. (2005) and Robertson et al. (2015) the reader finds more information on the implementation of the wall functions in OpenFOAM. The exact implementation can be found in the source code (OpenFOAM (2018b)). A starting point for the definition of boundary conditions for CFD simulations can be found in the best practice guideline of Franke et al. (2007).

Because the accuracy of a simulation model with wall functions was deemed sufficient for this study, the node of the wall-adjacent cell had to lie within the logarithmic layer (see Fig. 2.7.1). Whenever this is true, the velocity profile in the boundary layer is calculated with Eq. 2.7.15. In the case of the **wind tunnel simulations**, a constant velocity at the inlet corresponding to the respective Reynolds number and a zero gradient at the outlet were prescribed. All other boundaries were walls and therefore the no-slip condition was applied. For the pressure a zero gradient at the inlet and a fixed value at the outlet were set. A zero gradient was applied to the walls. The temperature of the inflow was fixed at 300 K. At the inner walls of the cavity, a small temperature difference of 1% relative to the inlet temperature was set in order to obtain a heat flux. At the remaining walls the

same temperature as at the inlet was set because during the experiment the wind tunnel walls were temperature controlled. At the exit, a zero gradient was chosen. The turbulence kinetic energy at the inlet was set on the basis of a turbulence intensity of 0.4% (Schewe (1983)). At the outlet, a zero gradient was applied. At the walls, the turbulence kinetic energy profile was calculated with wall functions and had a zero gradient. The turbulence dissipation at the inlet was calculated with the mixing length approach. The remaining boundaries were set analogously to the turbulence kinetic energy. The eddy viscosity and the turbulent thermal diffusivity were calculated from the values at the inlet and outlet. At the walls, a wall function was used for the eddy viscosity and the turbulent thermal diffusivity was calculated via the turbulence Prandtl number. A summary of the applied boundary conditions is found in Table 3.3.1.

In the **original scale simulations**, the constraining walls at the top, bottom, and sides were removed. Instead, at the top and bottom a slip condition was applied and the sides were opened to allow for inflow at a fixed value and outflow with a zero gradient. This affects the velocity, the temperature, the turbulence kinetic energy, and its dissipation. The boundary conditions for the eddy viscosity and the turbulent thermal diffusivity were also changed accordingly. The pressure boundary conditions were changed, too, in order to account for the large differences in height between top and bottom. For the pressure at the outlet and sides an adapted boundary condition was used which computes the pressure according to the barometric formula

$$p = p_{\mathrm{ref}} \exp\left(\frac{\mathbf{g}\cdot\mathbf{x}}{R_{\mathrm{spec}} T_{\mathrm{ref}}}\right), \tag{3.3.1}$$

where p_{ref} and T_{ref} are the reference pressure and temperature, respectively, and $\mathbf{g}$ and $\mathbf{x}$ are the gravity and position vectors, respectively.

Since the cavity temperature was raised to a typical operating temperature of 900 K in these simulations, this temperature rise was applied as a ramp-up function over 1000 iterations. In Table 3.3.2, the boundary conditions are summarized for the original scale simulations.

Numerical simulations which include more than pure diffusive terms also need a set of well-chosen initial values. In this work, the potential flow was solved on the domain and the results were then used to initialize the flow field. The turbulence quantities and the temperature were initially set constant on the whole domain. In the wind tunnel simulations, the pressure field was set constant, too. In the case of the original scale simulations the pressure field was initialized with the barometric formula given in Eq. 3.3.1.

3.3.4 Thermophysical Properties

The thermophysical properties of air for the CFD simulations were taken from VDI (2010). This includes the specific heat capacity c_{p}, the dynamic viscosity μ, and the thermal conductivity k. In the case of the wind tunnel simulations these properties were needed at 6 MPa and for a temperature range of approximately 0 °C to 50 °C. In the case of the original scale simulations these properties were needed at 0.1 MPa and at temperatures from 0 °C to 700 °C. A 4th order polynomial was fitted to the data and then provided to the CFD solver. The data and the fits are displayed in Fig. 3.3.2.

3.3.5 Meshing

In Section 3.3.3 it was mentioned that wall functions were used to model the boundary layer. This directly implies that the node of the wall-adjacent cell had to be within the

Table 3.3.1: Overview of the applied boundary conditions in the wind tunnel simulations. C symbolizes a scalar or vector constant and f a function. "calc" signifies that a quantity is calculated from other quantities.

Wind tunnel	$\mathbf{U}$	p	T	k	ω	ν_t	α_t
Inlet	$\mathbf{U} = \mathbf{C}$	$\frac{\partial p}{\partial n} = 0$	$T = C$	$k = C$	$\omega = C$	calc	calc
Outlet	$\frac{\partial \mathbf{U}}{\partial \mathbf{n}} = 0$	$p = C$	$\frac{\partial T}{\partial n} = 0$	$\frac{\partial k}{\partial n} = 0$	$\frac{\partial \omega}{\partial n} = 0$	calc	calc
Cavity inside	$\mathbf{U} = 0$	$\frac{\partial p}{\partial n} = 0$	$T = C$	$\frac{\partial k}{\partial n} = 0$	$\frac{\partial \omega}{\partial n} = 0$	$\nu_\mathrm{t} = f$	calc
Tower	$\mathbf{U} = 0$	$\frac{\partial p}{\partial n} = 0$	$T = C$	$\frac{\partial k}{\partial n} = 0$	$\frac{\partial \omega}{\partial n} = 0$	$\nu_\mathrm{t} = f$	calc
Top	$\mathbf{U} = 0$	$\frac{\partial p}{\partial n} = 0$	$T = C$	$\frac{\partial k}{\partial n} = 0$	$\frac{\partial \omega}{\partial n} = 0$	$\nu_\mathrm{t} = f$	calc
Bottom	$\mathbf{U} = 0$	$\frac{\partial p}{\partial n} = 0$	$T = C$	$\frac{\partial k}{\partial n} = 0$	$\frac{\partial \omega}{\partial n} = 0$	$\nu_\mathrm{t} = f$	calc
Sides	$\mathbf{U} = 0$	$\frac{\partial p}{\partial n} = 0$	$T = C$	$\frac{\partial k}{\partial n} = 0$	$\frac{\partial \omega}{\partial n} = 0$	$\nu_\mathrm{t} = f$	calc

Table 3.3.2: Overview of the applied boundary conditions in the original scale simulations. C symbolizes a scalar or vector constant and f a function. "calc" signifies that a quantity is calculated from other quantities.

Original scale	$\mathbf{U}$	p	T	k	ω	ν_t	α_t
Inlet	$\mathbf{U} = \mathbf{C}$	$\frac{\partial p}{\partial n} = 0$	$T = C$	$k = C$	$\omega = C$	calc	calc
Outlet	$\mathbf{U}_\mathrm{in} = f$ or $\frac{\partial \mathbf{U}_\mathrm{out}}{\partial \mathbf{n}} = 0$	$p = f$	$T_\mathrm{in} = C$ or $\frac{\partial T_\mathrm{out}}{\partial n} = 0$	$k_\mathrm{in} = C$ or $\frac{\partial k_\mathrm{out}}{\partial n} = 0$	$\omega_\mathrm{in} = C$ or $\frac{\partial \omega_\mathrm{out}}{\partial n} = 0$	calc	calc
Cavity inside	$\mathbf{U} = 0$	$\frac{\partial p}{\partial n} = 0$	$T = f$	$\frac{\partial k}{\partial n} = 0$	$\frac{\partial \omega}{\partial n} = 0$	$\nu_\mathrm{t} = f$	calc
Tower	$\mathbf{U} = 0$	$\frac{\partial p}{\partial n} = 0$	$\frac{\partial T}{\partial n} = 0$	$\frac{\partial k}{\partial n} = 0$	$\frac{\partial \omega}{\partial n} = 0$	$\nu_\mathrm{t} = f$	calc
Top	$\frac{\partial \mathbf{U}}{\partial \mathbf{n}} = 0$	$\frac{\partial p}{\partial n} = 0$	$\frac{\partial T}{\partial n} = 0$	$\frac{\partial k}{\partial n} = 0$	$\frac{\partial \omega}{\partial n} = 0$	calc	calc
Bottom	$\frac{\partial \mathbf{U}}{\partial \mathbf{n}} = 0$	$\frac{\partial p}{\partial n} = 0$	$\frac{\partial T}{\partial n} = 0$	$\frac{\partial k}{\partial n} = 0$	$\frac{\partial \omega}{\partial n} = 0$	calc	calc
Sides	$\mathbf{U}_\mathrm{in} = f$ or $\frac{\partial \mathbf{U}_\mathrm{out}}{\partial \mathbf{n}} = 0$	$p = f$	$T_\mathrm{in} = C$ or $\frac{\partial T_\mathrm{out}}{\partial n} = 0$	$k_\mathrm{in} = C$ or $\frac{\partial k_\mathrm{out}}{\partial n} = 0$	$\omega_\mathrm{in} = C$ or $\frac{\partial \omega_\mathrm{out}}{\partial n} = 0$	calc	calc

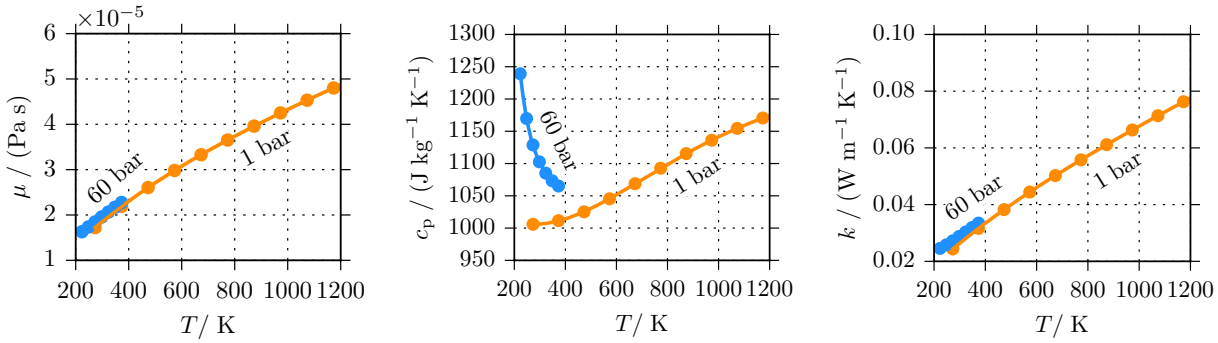

Figure 3.3.2: 4th order polynomial fit of the thermophysical properties of air: dynamic viscosity μ, specific heat capacity c_p, and thermal conductivity k. The data were taken from VDI (2010) and marked with dots.

logarithmic layer and thus, $30 < y^+ < 500$. In all simulations, the regions close to a wall were resolved with an inflation layer of approximately a dozen layers of thin cells. The remainder of the mesh was an unstructured mesh of regions with hexahedrons and of regions with tetrahedrons. In general, the farther away a cell was from the cavity or a wall, the larger was its size. The computational domain was split manually in different blocks before meshing. Then, these blocks were meshed one after another with different settings. This process is called selective meshing. It combines the computational speed and accuracy of the solution on a pure hexahedron mesh in easy meshable blocks with the ease and speed of meshing of a pure tetrahedron mesh in blocks with complex geometries. The result was a mixed unstructured mesh. The meshing was done with ANSYS Meshing 18.0 (ANSYS (2018)). In Fig. 3.3.3 a cross section of the mesh of the wind tunnel simulation with horizontal cavity and wind from the front is shown. It can be seen that the upstream and downstream regions consist of hexahedrons and only the region around the tower is made up of tetrahedrons. A close-up of the mesh in and around the cavity is shown in Fig. 3.3.4. In this figure, the surface mesh based on triangles can be seen on the tower walls behind the cavity.

Since the original scale simulations were done on an extended computational domain, the domain was separated in more regions to easier vary the size of the cells farther away from the tower. Scaling of the cells was applied in upstream, downstream, lateral and vertical directions. The remaining meshing parameters were set analogously to the wind tunnel simulations. The mesh of 1 of the original scale simulations is shown in Fig. 3.3.5. Different colors mark the different meshing blocks of the mesh.

3.3.6 Mesh Independency Study

By increasing the number of cells in a computational domain the discretization error of a CFD simulation is reduced. At the same time, this increases the computational cost. Thus, a CFD simulation should have as little cells as possible, but as much cells as needed to resolve the physics accurately. This trade-off is found by a so-called mesh independency study with at least 3 different sizes of cells in the domain. For such a study, the scaling factor between the cell sizes of 2 consecutive meshes should be large (≈ 2 in each direction) to clearly see the effects. The results of this study for both, the wind tunnel and the original scale simulations, are presented in Fig. 3.3.6. The normalized wall heat flux $\dot{q}_{\mathrm{rel}}$ on the cylindrical walls in the cavity is used as the measure of quality, resulting in $\dot{q}_{\mathrm{rel}} = 1$ for the finest mesh. The blue circles represent the proportional scaling of all cell sizes, except the

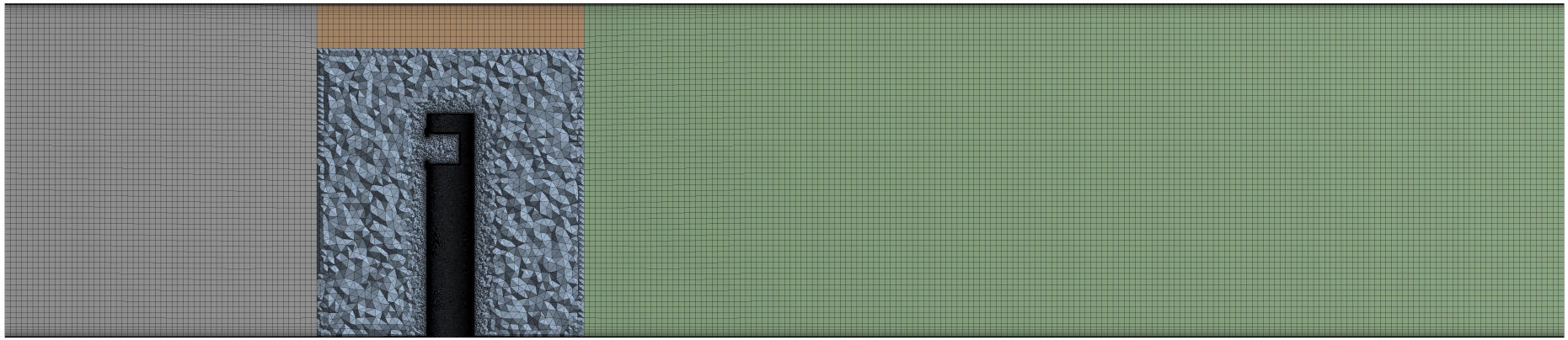

Figure 3.3.3: Cross section of the mesh for a wind tunnel simulation. Hexahedron regions are found upstream and downstream of the tower, a tetrahedron region is located in the cavity and around the tower. The different colors represent the different meshing blocks.

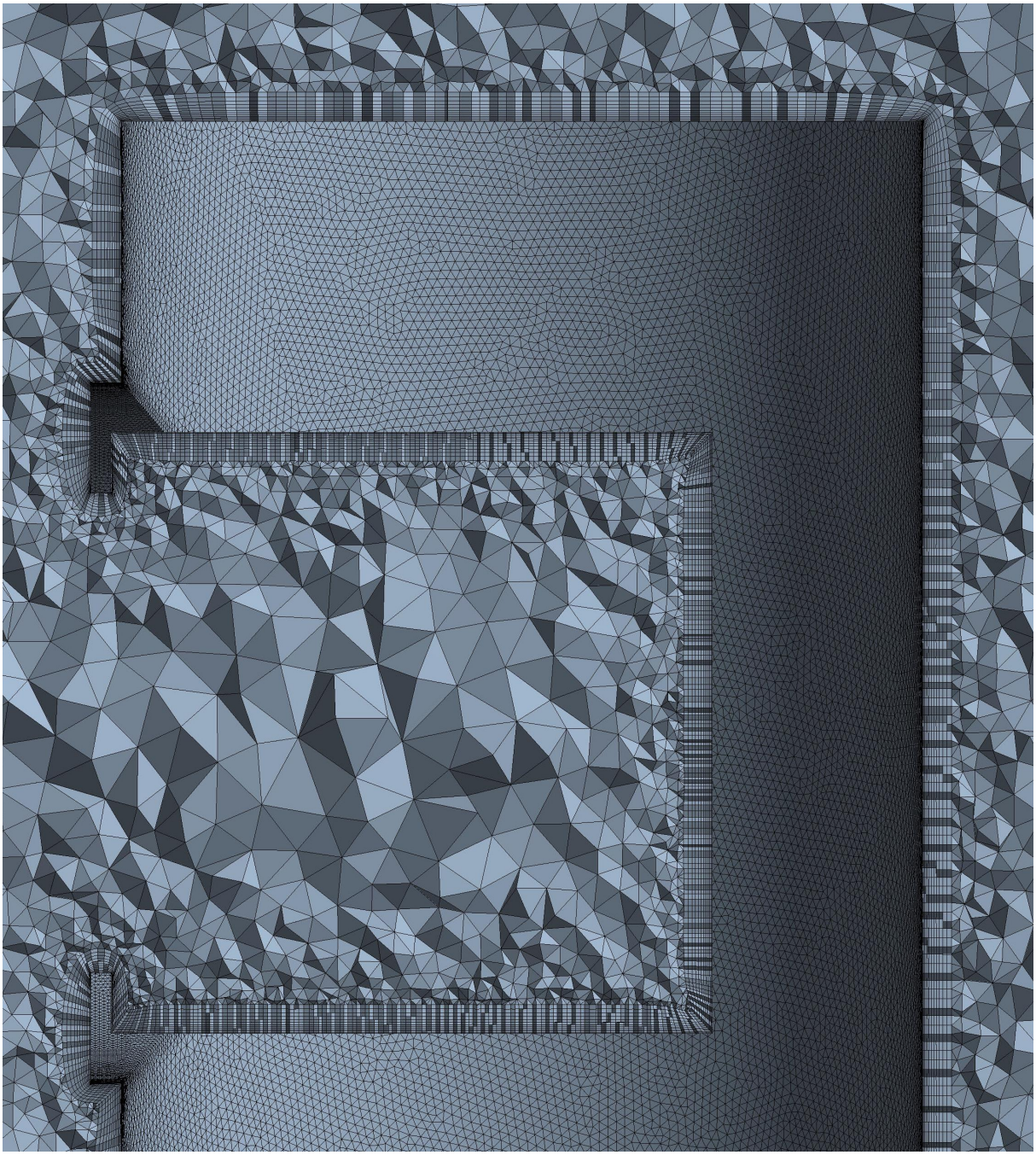

Figure 3.3.4: Half-model of the mesh in and around the cavity of a wind tunnel simulation. On the tower walls behind the cavity, the surface mesh based on triangles can be seen. Starting from this surface mesh, a thin inflation layer covers all walls.

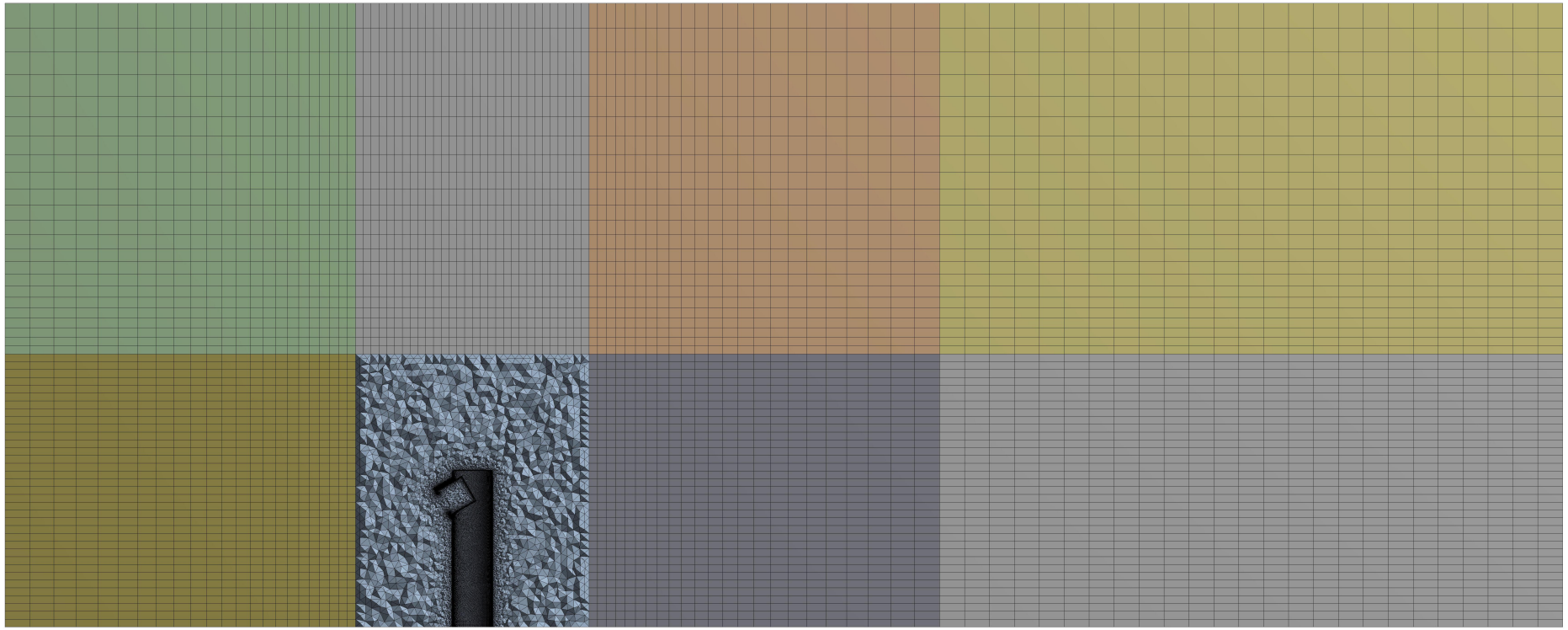

Figure 3.3.5: Cross section of the mesh for an original scale simulation. A tetrahedron region is found close to the cavity and around the tower, the remaining regions consist of hexahedrons. Scaling of the cells was applied in upstream, downstream, lateral and vertical directions. The different colors represent the different meshing blocks.

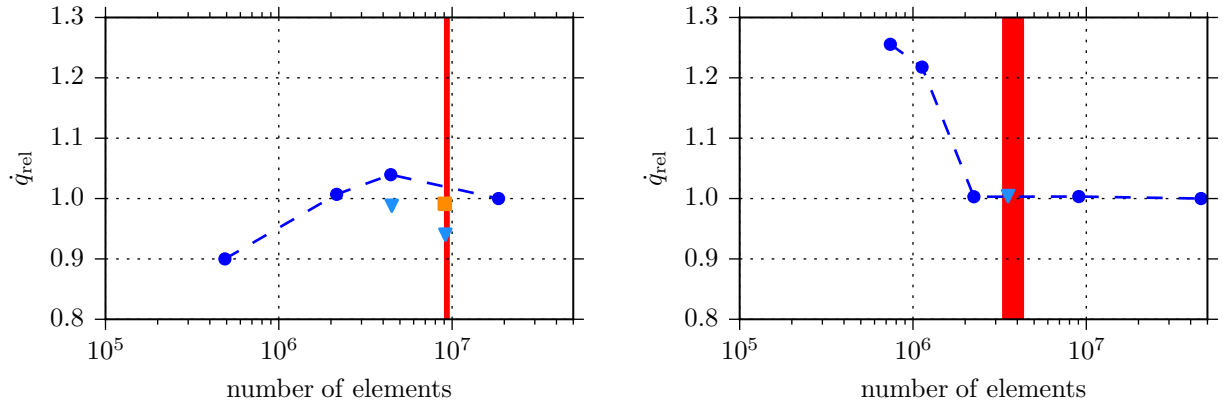

Figure 3.3.6: Mesh independency study of the wind tunnel simulation mesh (left) and the original scale simulation mesh (right). The normalized wall heat flux in the cavity $\dot{q}_{\mathrm{rel}}$ was used as the measure of quality. The blue circles represent proportional scaling of the cells in all directions, except the first layer at the wall. Triangles indicate a reduced first layer height at the wall and the square symbolizes a refinement of the cells within the cavity. The red vertical bars represent the selected number of elements.

height of the first layer at the surface. The triangles indicate a mesh with a reduced first layer height and the square symbolizes a refined mesh inside the cavity. The red vertical bars indicate the number of elements in the final meshes of the wind tunnel and original scale simulations. In the case of the wind tunnel simulations with the horizontal cavity, the meshes had approximately $9.3 \cdot 10^6$ elements. In the case of the original scale simulations, the number of elements ranged from $3.4 \cdot 10^6$ to $4.2 \cdot 10^6$. This difference regarding the number of cells is due to the different inclination angles which required a different number of cells.

3.3.7 Discretization Schemes

In Section 2.7, the concept of discretization was introduced. Now, the discretization schemes used in this work are reported. OpenFOAM provides the user with a variety of advanced schemes. The discretization scheme can be chosen on the basis of each discretization term (advective term, diffusive term, etc.) and for each quantity (velocity, pressure, temperature, turbulence kinetic energy, etc.). This has the advantage that the set of discretization schemes can be tailored to the problem. In all simulations, the gradient terms were discretized with a cell limited central differencing scheme. The divergence terms or advective terms were discretized differently for the 2 types of simulations. In the wind tunnel simulations, a bounded linear upwind scheme was applied for the velocity and the enthalpy terms, a bounded upwind scheme for the turbulence quantities, and a linear scheme for the eddy viscosity. In the original scale simulations, only the schemes for the velocity and enthalpy terms were changed to a bounded van Leer scheme. This scheme showed a slightly better stability. The Laplacian terms or diffusive terms were also discretized differently for the 2 types of simulations. In the wind tunnel simulations, the surface normal gradients were evaluated based on a scheme called corrected. In the original scale simulations, a limiter was added in order to stabilize the solution process. The used discretization schemes together with their order of accuracy are listed in Table 3.3.3. In addition, the used keywords in OpenFOAM are given in Appendix D.

Table 3.3.3: Overview of the used discretization schemes in the wind tunnel and original scale simulations. Also indicated are the conservativeness, boundedness, transportiveness and order of each scheme.

Discretization scheme	Conservative	Bounded	Transportive	Order
central differencing	yes	no	no	2
cell limited central differencing	yes	yes	no	2
bounded upwind	yes	yes	yes	1
bounded linear upwind	yes	yes	yes	2
bounded van Leer	yes	yes	yes	1 to 2
corrected	yes	no	no	2
limited corrected	yes	yes	no	2

3.3.8 Solver and Solution Settings

The goal of the CFD simulations was to achieve more insights regarding the flow in the cavity and around the tower for large SCR systems and not to compute highly accurate absolute numbers. Therefore, the numerical model was solved steady-state to save computational cost. For backward directions, the transient wake with possibly periodical vortices cannot be captured by a steady-state solver. Thus, it is clear that the validity of the CFD simulations is mainly limited to winds from frontal to lateral directions. The used solver is called buoyantSimpleFoam in OpenFOAM. It is a compressible solver which includes also the energy equation and is based on the well known SIMPLE algorithm which is described for example in Versteeg and Malalasekera (2007) or Ferziger and Peric (2002).

In almost all simulations with a SIMPLE solver, one has to specify *under-relaxation factors* Φ. If an under-relaxation factor is smaller than 1 the change of the corresponding quantity is not applied fully but to the relative amount specified by the under-relaxation factor. In the case of a SIMPLE solver, the optimum under-relaxation factors for the pressure and the velocity fields are found according to Ferziger and Peric (2002) as

$$\Phi_U + \Phi_p = 1\,. \tag{3.3.2}$$

For under-relaxation factors of the other quantities, no such clear recommendations can be found in literature. In general, one can say that an under-relaxation of less than 0.1 will slow convergence rather heavily. Thus, an under-relaxation should be chosen as close as possible to 1. In this work, all simulations with wind were calculated with final under-relaxation factors of 0.5 up to 0.8.

Once a simulation is running and converging stably, *convergence criteria* have to be checked. Monitoring residuals may give an indication of convergence. But as stated in Section 2.7, residuals alone are not a sufficient measure of convergence. A good convergence criterion is an integral quantity which is important for the investigated problem. In this work, the area-averaged heat flux and the sum of the heat flux on the cylindrical part of the cavity were monitored. The solution was considered converged, when these integral values did not change anymore for 10000 iterations. An example of the monitoring of the convergence of the original scale simulations is shown in Fig. 3.3.7.

3.3.9 Data Processing

Once a CFD simulation had converged, it was run for another 10000 iterations. At every 100th iteration the heat flux at the inside of the cavity was written out. To obtain a comparable value the area-averaged heat flux values over the last 10000 iterations, which were

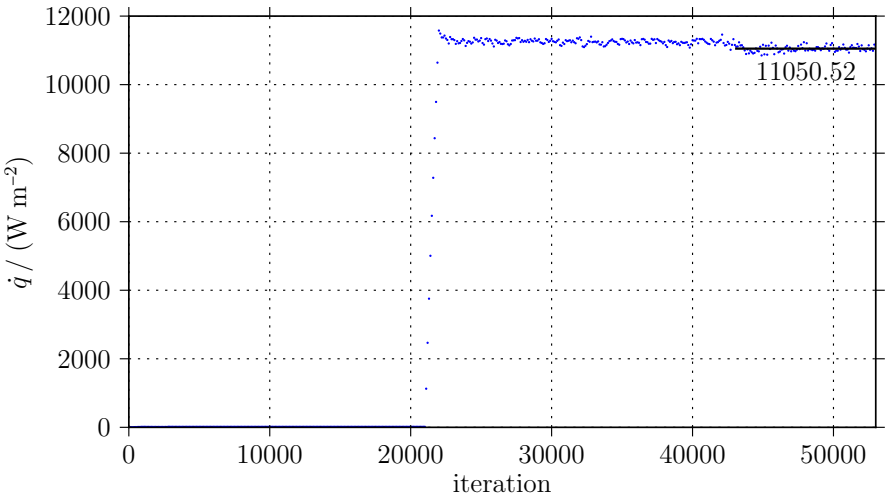

Figure 3.3.7: Convergence of the area-averaged heat flux on the inside of the cavity cylinder walls in the case of an original scale simulation. The heat flux is sampled every 100 iterations. From iteration 21001 to 22000, the temperature was ramped up linearly from $\Delta T = 3\,\mathrm{K}$ to $\Delta T = 600\,\mathrm{K}$. At iteration 42001, the under-relaxation factor for the energy equation was raised to 0.8. The black line indicates the averaging period and is annotated with the iteration-averaged heat flux.

Table 3.3.4: Ratio of forced convective heat flux $\dot{q}$ on the cylindrical part of the cavity to its back part. The ratio is shown for the horizontal cavity at 4 wind incident angles. The wind speed does not introduce a relevant change to the ratio.

Inclination angle γ / °	Incident angle α / °	Ratio $\dot{q}_{\mathrm{cyl}} / \dot{q}_{\mathrm{back}}$
0	0	0.85
0	10	1.00
0	70	0.81
0	90	1.11

100 values, were averaged. This area- and iteration-averaged heat flux $\dot{q}$ was then plugged into a Nusselt number formulation similar to Eq. 3.2.20 to obtain a nondimensional quantity of the heat loss

$$Nu = \frac{\dot{q} d_{\mathrm{cav}}}{k_{\mathrm{air}} \Delta T}. \tag{3.3.3}$$

To visualize the heat flux at the cavity surface OpenFOAM's utility wallHeatFlux was used to calculate the local convective heat flux. After, these data were processed to contour plots with python, see for example Fig. 3.2.12a.

As mentioned in Section 3.2.2, the ratio of $\dot{q}$ on the cylindrical part of the cavity to $\dot{q}$ on the back part of the cavity can be estimated with CFD. In Table 3.3.4 this ratio is presented for the horizontal cavity on the wind tunnel scale and wind incident angles $\alpha = [0°, 10°, 70°, 90°]$. The wind speed does not influence the ratio to a relevant amount.

3.3.10 Uncertainty Estimation

In Section 2.7, the 5 major steps of a CFD simulation were presented. Each of these 5 steps may introduce errors and uncertainty. At this point, it is important to understand the difference between error and uncertainties. In CFD, we speak about errors if we are aware

of the deficiency and we speak about uncertainty if we are unaware or unsure of the deficiency. Thus, numerical deficiencies, coding deficiencies, and user mistakes belong to the term error and discrepancies between the fluid properties in the simulation and in the real flow or deficiencies in the physical model such as introduced by a turbulence model are both belonging to the term uncertainty. One can perform a verification of the code to estimate the errors and a validation with experimental data to estimate the uncertainty. For a more thorough discussion, the reader is referred to the books by Versteeg and Malalasekera (2007) and Ferziger and Peric (2002). In the present work, it is assumed that the CFD code OpenFOAM v4.1 has been thoroughly verified by the developers and the user community. Therefore, the errors related to the code are expected to be small compared to the rest of the errors and the uncertainties. Thus, the sum of the remaining errors, such as user mistakes, and all possible uncertainties can be estimated by a comparison of the simulation results with the results of the wind tunnel measurements, see Section 4.2.1.

In a previous doctoral thesis (Flesch (2016)) and a master's thesis performed during that dissertation it was shown that the same CFD code as used here often underpredicts the free and the mixed convective heat loss. But, the magnitude of underprediction decreased with higher wind speeds and thus by simulating flows that are more governed by forced convection.

3.4 Estimation of Radiative and Conductive Heat Losses from Cavity Receivers

In order to quantify the importance of the convective heat loss it is necessary to consider the radiative and conductive heat losses, too. In this work, this estimation was performed for the original scale. It was assumed that the radiative heat loss is independent of the inclination angle γ. The radiative heat loss was estimated by calculating the view factor of the inner cavity surface to the surroundings and calculating the net radiative exchange according to Eq. 2.3.5. The view factor from the inner cylindrical surface to the aperture was calculated to be 0.1310 and from the cylinder bottom to the aperture opening was calculated to be 0.1159. The surroundings were assumed to be at a temperature of 300 K and to have an absorptivity of 1. The inner cavity walls were assumed to be at a uniform temperature of 900 K and to have an absorptivity of 0.9 which is a typical absorptivity of solar receiver panels. The net radiative heat loss through the aperture was calculated with the radiosity method explained in Section 2.3 by using the set of equations resulting from Eq. 2.3.5. The integral heat loss through radiation is

$$\dot{Q}_{\mathrm{rad}} = 4.2\,\mathrm{MW}\,. \tag{3.4.1}$$

Not only the radiative heat loss, but also the conductive heat loss is independent of γ. The heat loss through conduction was calculated with the 1D Fourier's Law as in Eq. 2.3.7. The temperature difference was assumed to be the full difference between the inner cavity walls and the surroundings. For the thermal insulation a thickness of 0.25 m and a thermal conductivity of $0.1\,\mathrm{W\,m^{-1}\,K^{-1}}$ were assumed (Ebert et al. (2015)). Under these assumptions, the integral heat loss through conduction is

$$\dot{Q}_{\mathrm{cond}} = 0.23\,\mathrm{MW}\,. \tag{3.4.2}$$

Chapter 4

Results

In this chapter, the results which were obtained with the methods described in Chapter 3 are presented. First, the experimental results of the forced convective heat loss measurements are introduced including the related flow visualization measurements. Second, the numerical results on the wind tunnel scale are presented and compared to the experimental data wherever possible. Additionally, the results of the CFD simulations with mixed convection on the original scale are presented. And last, the chapter closes by presenting the results of an estimation of the radiative and conductive heat losses in order to relate the magnitude of the different heat losses to each other.

4.1 Experimental Measurements

As stated in Section 3.2.1, the bulk temperature in the cavity T_{cav} has to equal the free-stream temperature T_∞. If this is true, the measured forced convective heat loss may be related to the Nusselt number in Eq. 3.2.20 directly. Since this condition holds in this work, the nondimensional heat loss in form of the Nusselt number is used throughout this chapter. In many sections of this chapter, the *relative forced convective Nusselt number* Nu_{rel} is used. This means that the interpolated and area-averaged $Nu_{i,aa}$ is normalized with $Nu_{i,aa}$ of the geometrical configuration ($\gamma = 30°, X_{ap} = 1.0$) at $Re = 6 \cdot 10^6$ and $\alpha = 70°$, which is the overall maximum of all measurement points.

Parts of the experimental results have already been published by the author and colleagues, this includes 2 conference contributions (Siegrist et al. (2018a); Stadler and Siegrist (2018)) and a journal article (Siegrist et al. (2018b)).

Missing data in the Reynolds series at $Re = 6 \cdot 10^6$ are due to operational limits of the force balance. The missing data at ($\gamma = 30°, X_{ap} = 0.6, Re = 4.5 \cdot 10^6$) are due to time constraints during the measurements.

The expanded uncertainty (this means at the 3σ level) in measuring the Reynolds number was calculated from data given by the operator of the wind tunnel as [±0.92%, ±0.52%, ±0.45%, ±0.45%] for $Re = [1.5 \cdot 10^6, 3.0 \cdot 10^6, 4.5 \cdot 10^6, 6.0 \cdot 10^6]$, respectively. The expanded uncertainty in measuring the wind incident angle α was estimated to be ±0.9°. The calculated expanded uncertainty for the relative forced convective Nusselt number Nu_{rel} ranges from ±7.0% to ±8.2%.

4.1.1 Forced Convective Heat Loss for Three Inclinations

Figure 4.1.1 shows the relative forced convective Nusselt number at an aperture ratio of 0.8. From left to right, the results are plotted for the cavity inclination angles $\gamma = [0°, 30°, 60°]$.

It is evident that for each geometrical configuration and all wind directions, except for ($\gamma = 0°, X_{ap} = 0.8$) at $\alpha = 140°$, the forced convective Nusselt number always increases with the Reynolds number.

For the **horizontal cavity** (left subfigure in Fig. 4.1.1), the data start at values between 0.05 and 0.2 and rise until the global maxima at $\alpha = 70°$, with the exception of a small plateau at $\alpha = [50°, 60°]$. The maximum value for these Reynolds number series is slightly

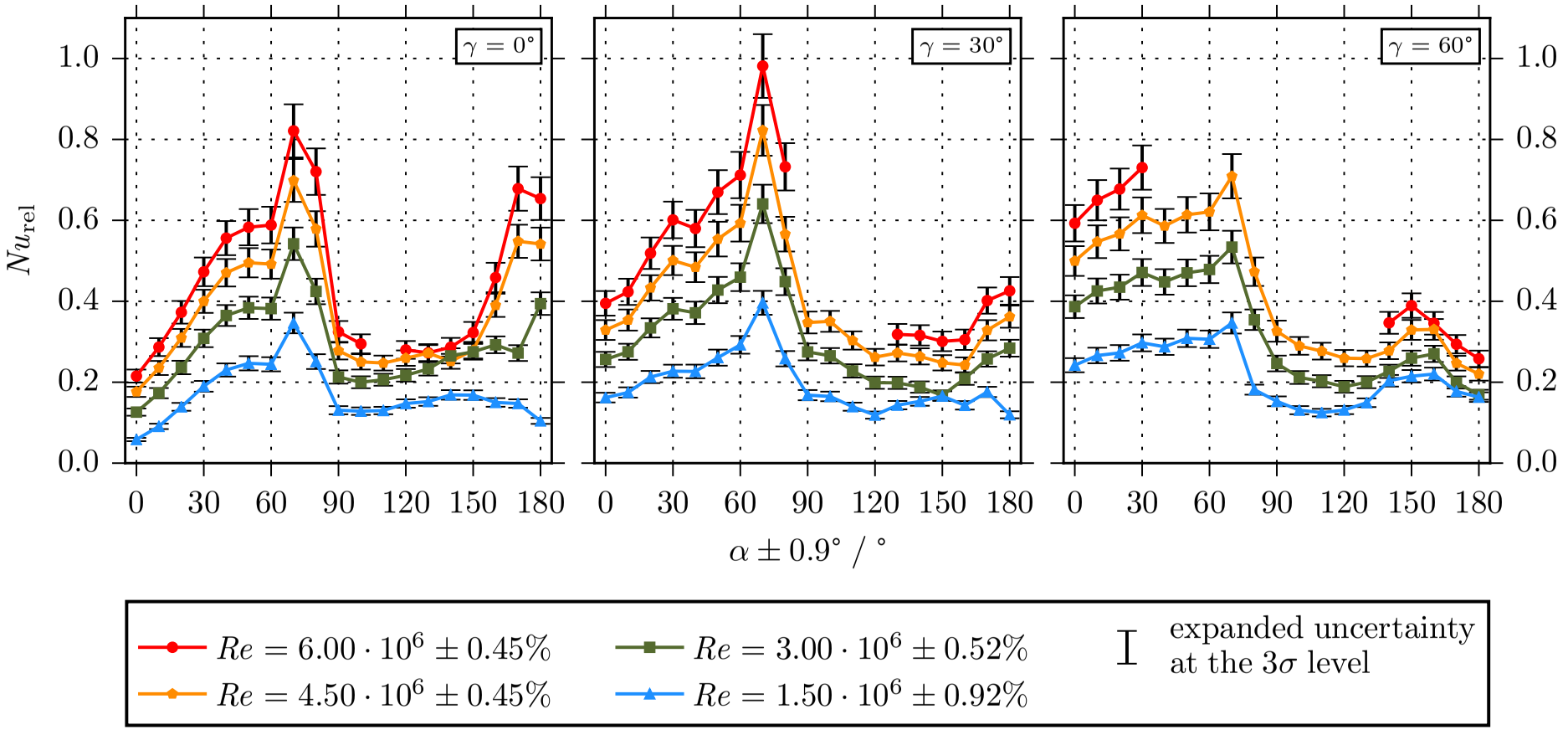

Figure 4.1.1: Relative forced convective Nusselt number for the horizontal cavity with $\gamma = 0°$ (left), for the downward inclined cavity with $\gamma = 30°$ (center), and for the downward inclined cavity with $\gamma = 60°$ (right). X_{ap} was 0.8. Each series was measured at steps of $\alpha = 10°$. Missing points at $Re = 6 \cdot 10^6$ are due to force balance restrictions. Uncertainties are given as expanded uncertainty at the 3σ level.

more than 0.8. After the clear peak, the data drop within $\Delta\alpha = 20°$ to levels comparable to Nu_{rel} at $\alpha = 0°$. For $Re = 1.5 \cdot 10^6$, the relative forced convective Nusselt number remains small and even decreases at $\alpha = 180°$. For $Re = 3 \cdot 10^6$, the relative forced convective Nusselt number slightly increases again until a sharp local maximum at $\alpha = 180°$. For $Re \geq 4.5 \cdot 10^6$, the data also increase slightly, but until broad local maxima at $\alpha = [170°, 180°]$.

In the case of the **cavity with** $\gamma = 30°$ (center subfigure in Fig. 4.1.1), the data rise from values between 0.15 and 0.4 until the global maxima at $\alpha = 70°$, but with the exception of a small plateau at $\alpha = [30°, 40°]$. The peak value for these Reynolds number series is almost 1. Thereafter, the data fall within $\Delta\alpha = 20°$ to levels comparable to Nu_{rel} at $\alpha = 0°$ or to even lower Nusselt numbers. For $Re = 1.5 \cdot 10^6$, the relative forced convective Nusselt number remains small with increasing α. For $Re = 3 \cdot 10^6$, the data further decrease slightly, but increase again for $\alpha \geq 150°$ to a second, local maximum at $\alpha = 180°$. For $Re \geq 4.5 \cdot 10^6$, the data also further decrease slightly and increase again for $\alpha \geq 160°$ to second, local maxima at $\alpha = 180°$.

In the case of the **cavity with** $\gamma = 60°$ (right subfigure in Fig. 4.1.1), the data begin at values of 0.2 to 0.6 and rise until the global maxima at $\alpha = 70°$, but with the exception of small buckles at $\alpha = 40°$. The peak value for these Reynolds number series lies at around 0.7, not including the values for $Re = 6 \cdot 10^6$ at $\alpha = [40°, \ldots, 130°]$. For $Re = 1.5 \cdot 10^6$, the relative forced convective Nusselt numbers drop within $\Delta\alpha = 10°$ to values well below those at $\alpha = 0°$. For $Re = 3 \cdot 10^6$ and $Re = 4.5 \cdot 10^6$, the data drop within $\Delta\alpha = 20°$ to values of Nu_{rel} well below those at $\alpha = 0°$. For $Re = 6 \cdot 10^6$, data at the incident angles where we expect the peak are not existent due to technical limits of the force balance. For $Re = 1.5 \cdot 10^6$, the data remain at low values until an increase at $\alpha \geq 130°$. This second, local maximum is a broad peak at $\alpha = [140°, \ldots, 160°]$ with reduced values for $\alpha \geq 170°$. For $Re = 3 \cdot 10^6$ and $Re = 4.5 \cdot 10^6$, the values remain low, except broad, smaller peaks at $\alpha = [150°, 160°]$. For $Re = 6 \cdot 10^6$, no values were reported at $\alpha = [40°, \ldots, 130°]$. The remaining values of this Reynolds number series show a small local maximum at $\alpha = 150°$ with a linear decrease until $\alpha = 180°$. All of the data at $\alpha \geq 140°$ lie below the values at $\alpha = 0°$. Nu_{rel} for all Reynolds number series at $\alpha = 180°$ shows similar values around 0.2.

4.1.2 Forced Convective Heat Loss for Three Apertures

In Fig. 4.1.2, the relative forced convective Nusselt number Nu_{rel} at an inclination of $\gamma = 30°$ is presented. From left to right, the results are plotted for $X_{\text{ap}} = [1.0, 0.8, 0.6]$. In the rightmost subplot, the data for $Re = 4.5 \cdot 10^6$ were not measured due to time constraints. The center plots of Fig. 4.1.1 and Fig. 4.1.2 show the same data.

The data in this section increase with the Reynolds number without exceptions.

In the case of the **fully open cavity** (left subfigure in Fig. 4.1.2), the data rise monotonically from values between 0.15 and 0.4 until broad global maxima at $\alpha = [60°, 70°]$. The maximum value for these Reynolds number series is 1. After the peak, the relative forced convective Nusselt numbers drop within $\Delta\alpha = 20°$ to levels comparable to Nu_{rel} at $\alpha = 0°$. For $Re = 1.5 \cdot 10^6$, the relative forced convective Nusselt number remains low with a slight increase until $\alpha = 170°$ and a sudden drop at $\alpha = 180°$. For $Re = 3 \cdot 10^6$, Nu_{rel} remains low except for a second, small peak at $\alpha = [160°, 170°]$. For $Re \geq 4.5 \cdot 10^6$, the data remain at low values, but showing small increases at $\alpha = [170°, 180°]$.

The case of the **aperture ratio of 0.8** is already described in the previous section. Thus, the reader is kindly referred to Section 4.1.1.

For the **smallest aperture** studied in this experiment, the data rise steeply from values between 0.15 and 0.4 to first, local maxima at $\alpha = 20°$. After the first peak, the values drop

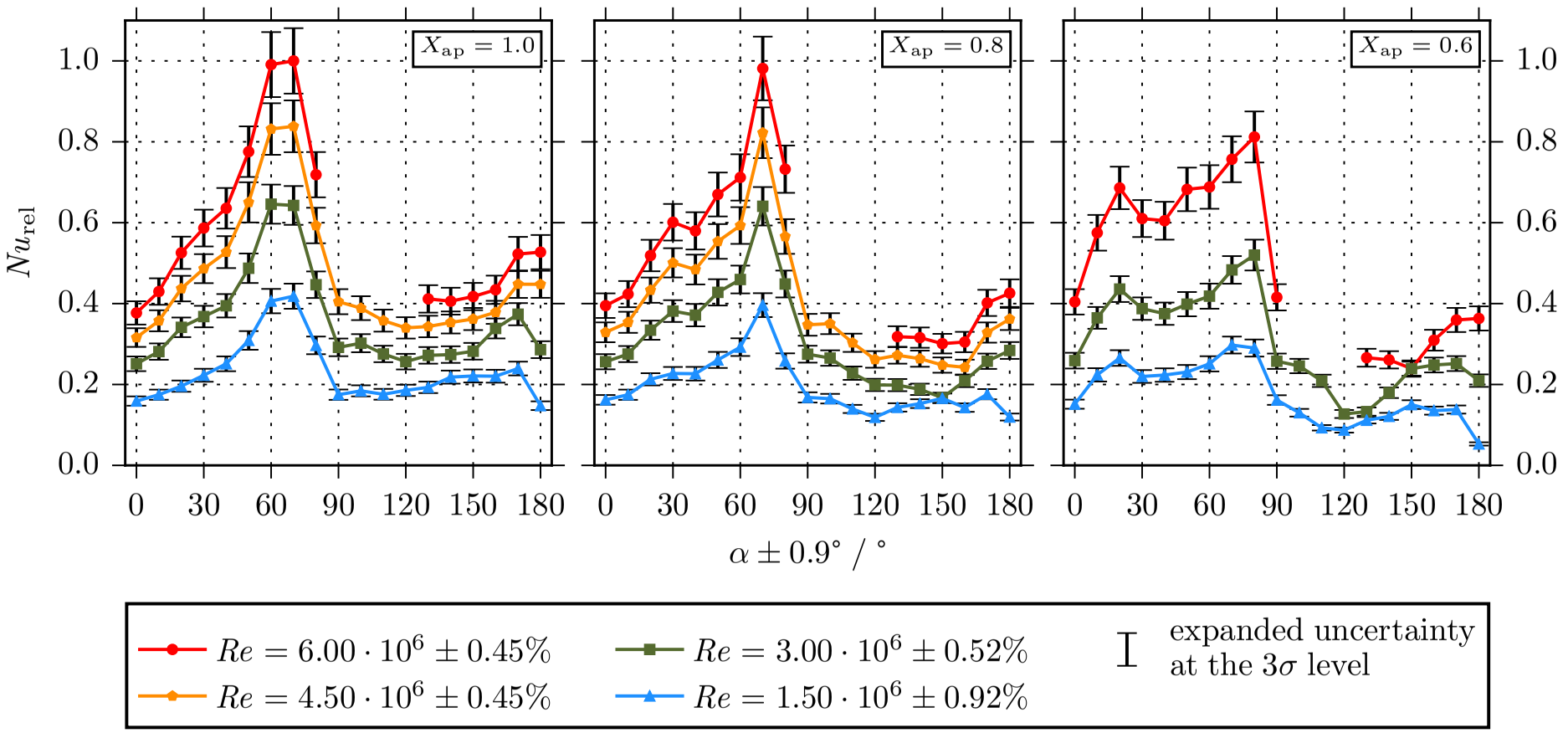

Figure 4.1.2: Relative forced convective Nusselt number for the cavities with an aperture ratio X_{ap} of 1.0 (left), 0.8 (center), and 0.6 (right). The cavities were inclined at $\gamma = 30°$. Each series was measured at steps of $\alpha = 10°$. Missing points at $Re = 6 \cdot 10^6$ are due to force balance restrictions. Due to time constraints the data for $X_{ap} = 0.6$ at $Re = 4.5 \cdot 10^6$ could not be measured. Uncertainties are given as expanded uncertainty at the 3σ level.

in the order of 10% and increase again to second, higher maxima at $\alpha = 80°$. For these Reynolds number series, the maximum Nu_{rel} lies at 0.8. After the global maxima, the data fall steeply within $\Delta\alpha = 10°$ to values comparable to Nu_{rel} at $\alpha = 0°$. For $Re = 1.5 \cdot 10^6$, the data continue to fall until a minimum at $\alpha = 120°$. Then, the relative forced convective Nusselt number increases again to a plateau at $\alpha = [150°, \ldots, 170°]$, whereupon it drops to around 0.05 at $\alpha = 180°$. For $Re = 3 \cdot 10^6$, the data continue to fall, too, until a minimum is reached at $\alpha = 120°$. The relative forced convective Nusselt number reaches a third, broad maximum at $\alpha = [150°, \ldots, 170°]$ with a slight decrease at $\alpha = 180°$. The Reynolds number series at $Re = 4.5 \cdot 10^6$ was not measured due to time constraints. For $Re = 6 \cdot 10^6$, the data also continue to fall, but with an unknown pattern, since the technical limits prevented the measurement at $\alpha = [100°, \ldots, 120°]$. The figure shows, that the data have a small local minimum at $\alpha = 150°$. Thereafter, the relative forced convective Nusselt number increases to a third maximum at $\alpha = [170°, 180°]$.

4.1.3 Forced Convective Heat Loss for Three Reduction Measures

Figure 4.1.3 presents the relative forced convective Nusselt number Nu_{rel} for the horizontal cavity with $X_{ap} = 0.8$. From left to right, the results are plotted for the solid porch, the porous porch, and the aerodynamic porch.

In this figure, one clearly sees that for each reduction measure and all wind directions, except for the porous porch at $\alpha = [140°, 150°]$, the relative forced convective Nusselt number always increases with the Reynolds number.

In the case of the **solid porch**, the data rise monotonically from almost 0 to their first maxima at $\alpha = 50°$. For all Reynolds number series, the maxima are broad and end approximately at $\alpha = 70°$. Thereafter, Nu_{rel} fall to local minima at $\alpha = 90°$. For $Re = 1.5 \cdot 10^6$ and backward winds, the relative forced convective Nusselt number remains at approximately the same level with a slight increase towards higher α and a small drop for $\alpha = 180°$. For $Re \geq 3 \cdot 10^6$, the data remain at the broad minima until $\alpha = 110°$. Then, with higher Reynolds number the data show also higher second peaks at $\alpha = 130°$ and sharper second minima at $\alpha = 150°$. For the 3 highest Reynolds numbers and backward winds with $\alpha > 150°$, Nu_{rel} increase to values similar to its peak value. The maximum peak value for all Reynolds number series lies slightly above 0.6.

For the **porous porch**, the relative forced convective Nusselt numbers start approximately at values of 0.05 to 0.2. Then, the data increase steadily until broad maxima are reached. For $Re = 1.5 \cdot 10^6$, the maximum is located at $\alpha = [40°, \ldots, 70°]$. After this maximum, the data fall to a minimum at $\alpha = 90°$. For winds with $\alpha > 90°$, Nu_{rel} remains approximately constant with a slightly increasing trend and a small drop at $\alpha = 180°$. For $Re \geq 3 \cdot 10^6$, the peaks start at $\alpha = 50°$ and last until $\alpha = 70°$. Afterwards, the data fall to minima at $\alpha = 90°$. The value of the local minimum at $\alpha = 90°$ for each Re is almost the same as the value for $\alpha = 0°$. For $Re = 3 \cdot 10^6$ and $90° < \alpha \leq 180°$, the relative forced convective Nusselt number increases continuously. For $Re = 4.5 \cdot 10^6$ and $\alpha > 90°$, the data rise to values that are higher than the first maximum. In the case of $Re = 6 \cdot 10^6$, Nu_{rel} has a local minimum at $\alpha = 140°$ and rises steeply to the maximum for all Re which lies at 0.7.

In the case of the **aerodynamic porch**, the data begin almost at 0 and rise approximately linearly to the maxima. For $Re = 3 \cdot 10^6$, this maximum is located at $\alpha = 60°$. For the remaining Reynolds number series, the maxima are at $\alpha = [60°, 70°]$. Thereafter, the data for all Re fall until local minima at $\alpha = 90°$ which are approximately half of their respective maximum value. Then, for $Re = 1.5 \cdot 10^6$ the relative forced convective Nusselt number increases slightly and remains almost constant throughout the backward winds, except for a drop at $\alpha = 180°$. For $Re = 3 \cdot 10^6$, Nu_{rel} increases and then remains roughly constant at

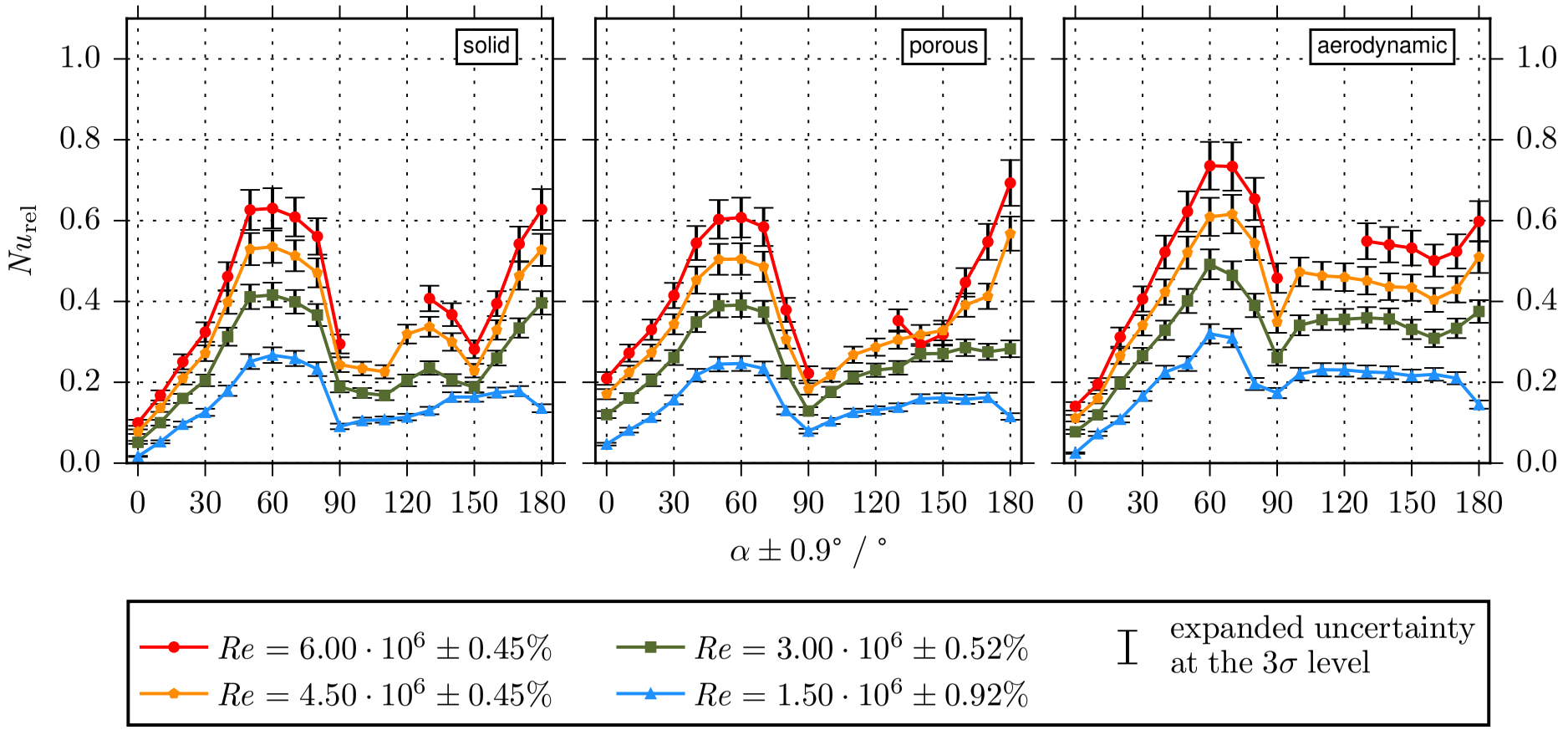

Figure 4.1.3: Relative forced convective Nusselt number for 3 reduction measures: solid porch (left), porous porch (center), and aerodynamic porch (right), mounted on the horizontal cavity ($\gamma = 0°$) with $X_{ap} = 0.8$. Each series was measured at steps of $\alpha = 10°$. Missing points at $Re = 6 \cdot 10^6$ are due to force balance restrictions. Uncertainties are given as expanded uncertainty at the 3σ level.

$\alpha = [100°, \ldots, 140°]$. For $Re = 4.5 \cdot 10^6$, the data also increase, but then have a negative linear trend. For all $Re \geq 3 \cdot 10^6$, the data have second minima at $\alpha = 160°$ and second maxima at $\alpha = 180°$. The overall peak value for the 3 reduction measures is marginally higher than 0.7.

4.1.4 Tabulated Values for the Measurements

In Table 4.1.1, the ratio of the maximum to the minimum relative forced convective Nusselt number of a given Reynolds number series as well as the maximum relative forced convective Nusselt number is given. The table comprises the data presented in Figs. 4.1.1, 4.1.2, and 4.1.3 in a condensed form. Since the measurements for $(\gamma = 60°, X_{ap} = 0.8, Re = 6 \cdot 10^6)$ are missing in large parts, the values derived from this data series are marked with a dagger and have to be interpreted with caution. The table also includes the references to the figures of the geometrical configurations.

In this table it can be seen that the horizontal cavity with $X_{ap} = 0.8$ has max-to-min ratios which lie in between of 3.9 and 6.1 and has a maximum Nu_{rel} of 0.82. For a cavity inclination of 30° the max-to-min ratios range from 3.3 to 3.8 and 0.98 is the maximum value. At the highest inclination, the ratios are 3.0 ± 0.2 and the maximum lies at 0.71 without considering the partial data. In the case of the fully open cavity at $\gamma = 30°$, the max-to-min ratios are 2.7 ± 0.1 and the maximum relative forced convective Nusselt number is 1. For the same inclination but the more closed aperture ($X_{ap} = 0.6$), the max-to-min ratios range from 3.4 to 5.6 and the maximum is at 0.81. The max-to-min ratios for the solid porch are high and lie between 6.4 and 18.1. The maximum value is 0.63. In the case of the porous porch, the ratios range from 3.3 to 5.3 and the maximum Nu_{rel} is 0.69. The third reduction measure, the aerodynamic porch, shows a range of max-to-min ratios of in between 5.3 and 12.9 and has a maximum value of 0.74.

4.1.5 Absolute Incident Angle

The absolute incident angle χ is defined as the cone angle between the incident wind and the aperture normal as shown in Fig. 3.2.1b. Because only the forced convection was measured the expectation was that the relative forced convective Nusselt number for a constant absolute incident angle should be approximately equal, for example in the cases of $(\gamma = 0°, \alpha = 30°)$ and $(\gamma = 30°, \alpha = 0°)$. It should be noted that for the horizontal cavity with $\gamma = 0°$ follows $\chi = \alpha$. This is not true for $\gamma = [30°, 60°]$. To analyze the relation between Nu_{rel} and χ a subset of the data was selected. The subset included the data from the configurations without reduction measures with $X_{ap} = 0.8$ and $\alpha \leq 90°$. Only frontal winds were selected because at $\alpha > 90°$ the influence of the tower and the wake was supposed to be predominant and χ can consequently not be known. On this selected subset a rotation matrix was applied and the resulting data are plotted in Fig. 4.1.4. This figure shows that the relative forced convective Nusselt numbers for each Reynolds number series are of similar magnitude at $\chi = [30°, 40°, 50°, 60°]$ and $\chi = 90°$. At absolute incident angles $\chi = [70°, 80°]$ the spread in Nu_{rel} is larger than at the other absolute incident angles. This coincides with the peak values for each Reynolds number series. Also easily identifiable is the approximately linear increase for all Re until the inflection point at $\chi \approx 70°$ and the following large drop in Nu_{rel}.

4.1.6 Nusselt Number as a Function of the Reynolds Number

To analyze the dependency of the relative forced convective Nusselt number on the Reynolds number a multi-variate regression was used to fit a power law with a one-fits-all exponent: $Nu_{rel} = CRe^n$. The exponent $n = 0.68$ for all absolute incident angles χ. The

Table 4.1.1: Ratio of the maximum relative forced convective Nusselt number to the minimum relative forced convective Nusselt number of the same Reynolds number series as well as the maximum relative forced convective Nusselt number of each Reynolds number series. The reduction measures were measured with $X_{ap} = 0.8$. The data in Fig. 4.1.1 center and Fig. 4.1.2 center are identical. The data for ($\gamma = 30°, X_{ap} = 0.6, Re = 4.5 \cdot 10^6$) are missing due to time constraints.

Subfigure	Inclination angle γ / °	Aperture	Reynolds number Re	Max-to-min ratio	Maximum value $Nu_{rel,max}$
Figs. 4.1.1 left 3.2.9a	0	0.8	$1.5 \cdot 10^6 \pm 0.92\%$	$6.1 \pm 7.4\%$	$0.35 \pm 7.4\%$
	0	0.8	$3.0 \cdot 10^6 \pm 0.52\%$	$4.5 \pm 7.4\%$	$0.54 \pm 7.4\%$
	0	0.8	$4.5 \cdot 10^6 \pm 0.45\%$	$4.0 \pm 7.6\%$	$0.70 \pm 7.6\%$
	0	0.8	$6.0 \cdot 10^6 \pm 0.45\%$	$3.9 \pm 8.0\%$	$0.82 \pm 8.0\%$
Figs. 4.1.1 center 3.2.9b	30	0.8	$1.5 \cdot 10^6 \pm 0.92\%$	$3.3 \pm 7.5\%$	$0.40 \pm 7.5\%$
	30	0.8	$3.0 \cdot 10^6 \pm 0.52\%$	$3.8 \pm 7.4\%$	$0.64 \pm 7.4\%$
	30	0.8	$4.5 \cdot 10^6 \pm 0.45\%$	$3.4 \pm 7.6\%$	$0.82 \pm 7.6\%$
	30	0.8	$6.0 \cdot 10^6 \pm 0.45\%$	$3.3 \pm 8.0\%$	$0.98 \pm 8.0\%$
Figs. 4.1.1 right 3.2.9c	60	0.8	$1.5 \cdot 10^6 \pm 0.92\%$	$2.8 \pm 7.5\%$	$0.35 \pm 7.5\%$
	60	0.8	$3.0 \cdot 10^6 \pm 0.52\%$	$3.2 \pm 7.6\%$	$0.53 \pm 7.6\%$
	60	0.8	$4.5 \cdot 10^6 \pm 0.45\%$	$3.2 \pm 7.7\%$	$0.71 \pm 7.7\%$
	60	0.8	$6.0 \cdot 10^6 \pm 0.45\%$	$2.8 \pm 7.5\%^{\dagger}$	$0.73 \pm 7.5\%^{\dagger}$
Figs. 4.1.2 left 3.2.10a	30	1.0	$1.5 \cdot 10^6 \pm 0.92\%$	$2.8 \pm 7.4\%$	$0.42 \pm 7.4\%$
	30	1.0	$3.0 \cdot 10^6 \pm 0.52\%$	$2.6 \pm 7.5\%$	$0.65 \pm 7.5\%$
	30	1.0	$4.5 \cdot 10^6 \pm 0.45\%$	$2.7 \pm 7.6\%$	$0.84 \pm 7.6\%$
	30	1.0	$6.0 \cdot 10^6 \pm 0.45\%$	$2.7 \pm 8.1\%$	$1.00 \pm 8.1\%$
Figs. 4.1.2 right 3.2.10c	30	0.6	$1.5 \cdot 10^6 \pm 0.92\%$	$5.6 \pm 7.0\%$	$0.30 \pm 7.0\%$
	30	0.6	$3.0 \cdot 10^6 \pm 0.52\%$	$4.1 \pm 7.3\%$	$0.52 \pm 7.3\%$
	30	0.6	$6.0 \cdot 10^6 \pm 0.45\%$	$3.4 \pm 7.8\%$	$0.81 \pm 7.8\%$
Figs. 4.1.3 left 3.2.11a	0	solid	$1.5 \cdot 10^6 \pm 0.92\%$	$18.1 \pm 7.2\%$	$0.27 \pm 7.2\%$
	0	solid	$3.0 \cdot 10^6 \pm 0.52\%$	$8.6 \pm 7.3\%$	$0.42 \pm 7.3\%$
	0	solid	$4.5 \cdot 10^6 \pm 0.45\%$	$7.0 \pm 7.5\%$	$0.54 \pm 7.5\%$
	0	solid	$6.0 \cdot 10^6 \pm 0.45\%$	$6.4 \pm 7.9\%$	$0.63 \pm 7.9\%$
Figs. 4.1.3 center 3.2.11b	0	porous	$1.5 \cdot 10^6 \pm 0.92\%$	$5.3 \pm 7.5\%$	$0.25 \pm 7.5\%$
	0	porous	$3.0 \cdot 10^6 \pm 0.52\%$	$3.3 \pm 7.5\%$	$0.39 \pm 7.5\%$
	0	porous	$4.5 \cdot 10^6 \pm 0.45\%$	$3.4 \pm 7.4\%$	$0.57 \pm 7.4\%$
	0	porous	$6.0 \cdot 10^6 \pm 0.45\%$	$3.4 \pm 8.2\%$	$0.69 \pm 8.2\%$
Figs. 4.1.3 right 3.2.11c	0	aero	$1.5 \cdot 10^6 \pm 0.92\%$	$12.9 \pm 7.5\%$	$0.32 \pm 7.5\%$
	0	aero	$3.0 \cdot 10^6 \pm 0.52\%$	$6.4 \pm 7.5\%$	$0.49 \pm 7.5\%$
	0	aero	$4.5 \cdot 10^6 \pm 0.45\%$	$5.6 \pm 7.7\%$	$0.62 \pm 7.7\%$
	0	aero	$6.0 \cdot 10^6 \pm 0.45\%$	$5.3 \pm 8.0\%$	$0.74 \pm 8.0\%$

†These values should be used with caution, since they are calculated from a largely incomplete data series.

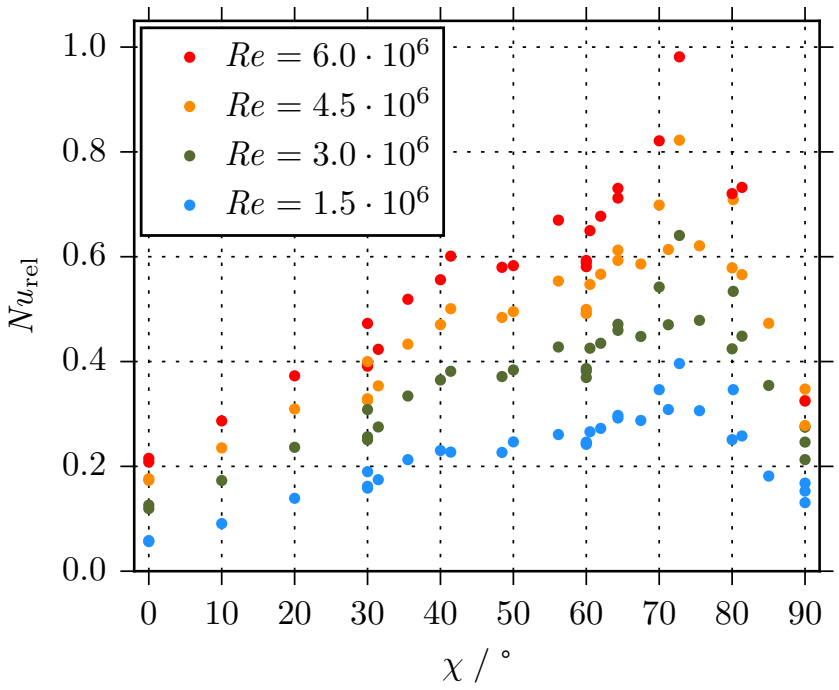

Figure 4.1.4: Relative forced convective Nusselt number for all measurements with $X_{ap} = 0.8$ and $\alpha \leq 90°$. The variable χ represents the absolute incident angle with respect to the aperture normal as defined in Fig. 3.2.1b.

data together with the fits are plotted in Fig. 4.1.5. The monomial constants C were calculated as $[4.64 \cdot 10^{-6}, 9.73 \cdot 10^{-6}, 1.69 \cdot 10^{-5}, 1.03 \cdot 10^{-5}]$ in ascending order of a selection of the absolute incident angle $\chi = [0°, 30°, 60°, 90°]$. The coefficient of determination is $R^2 = 0.92$.

Easily visible are 2 data points at ($\chi = 0°, Re = 1.5 \cdot 10^6$) that stick out from the power-law fit. It can be noted that for $\chi = 0°$ the relative Nusselt numbers are the lowest. For $\chi = [0°, \ldots, 60°]$, Nu_{rel} increases with increasing χ. In the case of $\chi = 90°$, the values of the relative forced convective Nusselt number are comparable to those at $\chi = 30°$.

4.1.7 Visualization with Background-Oriented Schlieren Imaging

During the experiments, the visualization technique BOS (see 3.2.1.5 for details) was used to obtain visual information about the flow close to the cavity. In Fig. 4.1.6, the mean pixel shift Δpx of the background pattern is shown for the horizontal cavity with an aperture ratio $X_{ap} = 0.8$ for 4 wind incident angles $\alpha = [60°, 70°, 80°, 90°]$ and at $Re = 6 \cdot 10^6$. The magnitude and direction of the pixel shift are indicated by the black arrows. The barb symbolizes the wind direction. It can be seen that at $\alpha = 60°$ the mean pixel shift is low. Then, at $\alpha = 70°$ the upstream edge of the cavity generates a strong pixel shift which is very close to the aperture. Interestingly, this coincides with the maximum of Nu_{rel} of this Re series, see left subfigure in Fig. 4.1.1. At $\alpha = 80°$, this strong deviation is still seen, but has moved moderately away from the aperture. And finally, for lateral winds Δpx is reduced and has moved far away from the aperture.

4.2 Numerical Simulations

In this chapter, the results obtained with the performed CFD simulations, as described in Section 3.3, are presented. It starts with the comparison of the CFD simulations of 1 model of the wind tunnel experiments to the related measurements. This comparison is

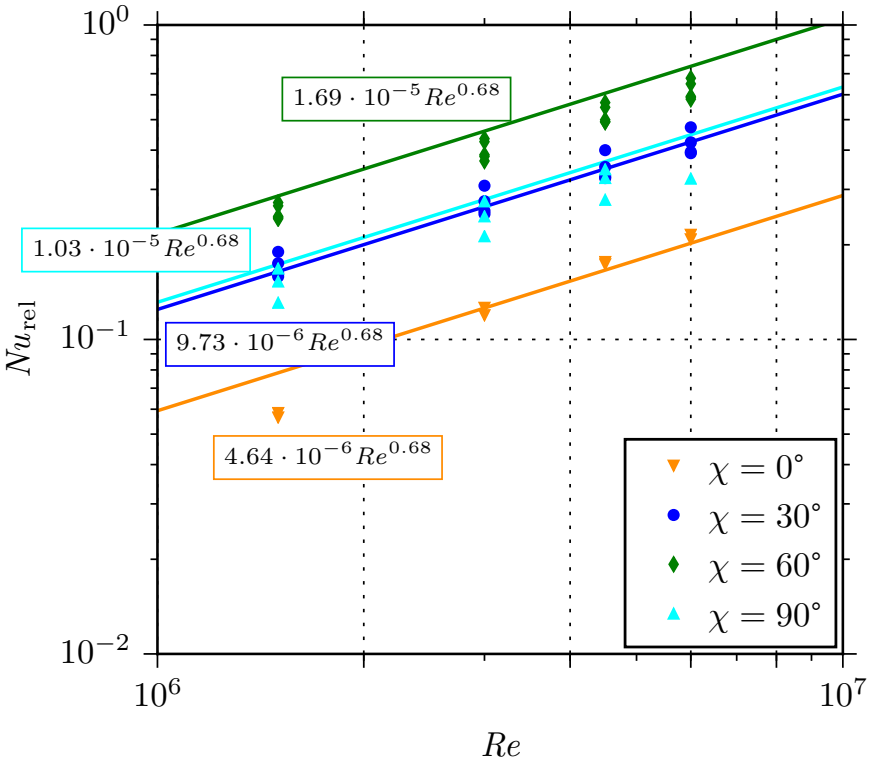

Figure 4.1.5: Relative forced convective Nusselt number for all measurements with $X_{\mathrm{ap}} = 0.8$ and $\chi = [0°, 30°, 60°, 90°]$. The data were fitted to a power law with a multi-variate regression.

done on the basis of a slightly heated cavity and thus is in the forced convection regime only. It serves as validation for the numerical simulations at high Reynolds numbers. It then continues and presents the CFD simulation results of the original scale model. These simulations were done with a typical operating temperature of the cavity at 1 typical wind speed that was chosen to give a mixed convection regime.

4.2.1 Comparison of the Experimental and Numerical Data of a Wind Tunnel Model

The data of the CFD simulations for the wind tunnel model with $\gamma = 0°$ and $X_{\mathrm{ap}} = 0.8$ are presented in Fig. 4.2.1 and marked by solid lines. These CFD simulations were designed to be dominated by forced convection and should therefore be comparable to the experimental measurements which are marked by dashed lines. All CFD data were scaled with a single factor to minimize the sum of the distances between the experimental and numerical values. This is a valid procedure because Nu_{rel} is normalized with an arbitrary value. Hence, the numerical values have to be scaled accordingly. The red diamond symbolizes the result of the simulation where the domain cross section was scaled by approximately 3 while keeping all other parameters identically. Since the CFD simulations were performed with a steady-state solver the region for $\alpha \leq 90°$ is considered the trusted region and marked with a green background. For $\alpha > 90°$ the CFD model is expected to be unable to capture relevant physical phenomena such as vortices in the wake. Thus, these values have to be considered with caution. The experimental data are not commented again because they are an extract of the data already presented in the left subfigure of Fig. 4.1.1.

The forced convective heat loss data computed by the CFD simulations start much higher than the measured values. These CFD values at $\alpha = 0°$ are comparable to experimen-

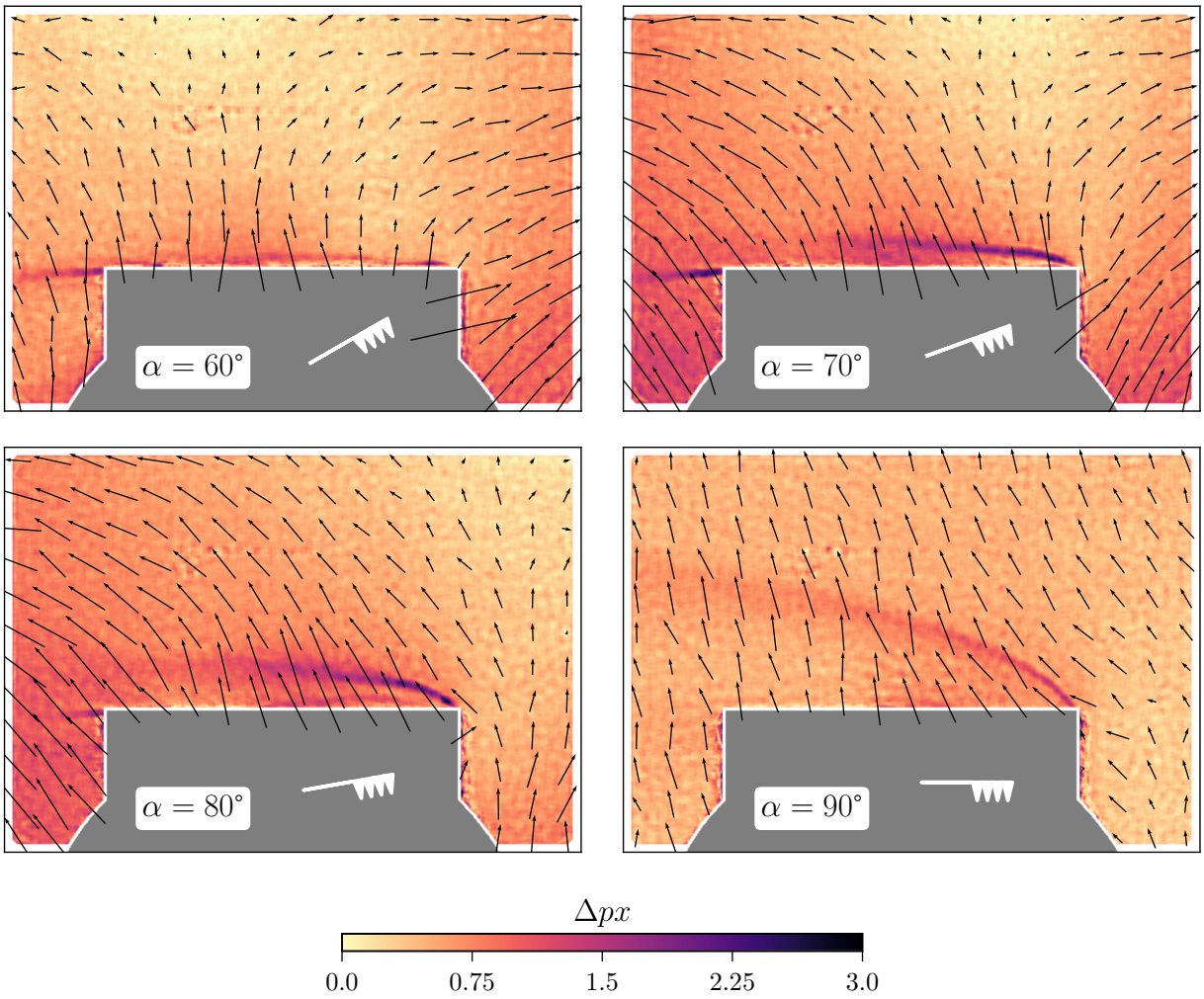

Figure 4.1.6: Mean pixel shift Δpx of the background pattern obtained with a background-oriented schlieren imaging setup. Magnitude and direction of Δpx are indicated by arrows. The barb symbolizes the wind incident angle α. The case shown here is the horizontal cavity with $X_{ap} = 0.8$ and at $Re = 6 \cdot 10^6$.

tal values at $\alpha \approx [30°, 40°]$. Interestingly, the result of an enlarged domain is much closer to the measurements, but lies still above the measured value. At $\alpha = 10°$, the CFD simulations result in slightly higher Nu_{rel} compared to the experiments. At the location of the experimental maximum values at $\alpha = 70°$, the CFD simulation with the lower wind speed underpredicts and the simulation with the higher wind speed overpredicts the forced convective heat loss. For lateral winds, both simulations show lower heat loss values. At backward winds, the lower wind speed simulations give results that are almost indistinguishable of the measured ones. The higher wind speed simulations underpredict the forced convective heat loss considerably. They also show a large drop from $\alpha = 170°$ to $\alpha = 180°$.

4.2.2 Simulations of the Original Scale Model

The geometrical configurations in Fig. 3.2.9 were also simulated in CFD on the original scale with mixed convection and a typical operating temperature of the receiver. The simulation results of these 3 configurations with cavity inclination angles of $\gamma = [0°, 30°, 60°]$ are shown in Fig. 4.2.2. The simulations were performed for 1 Reynolds number $Re = 6.0 \cdot 10^6$. As explained in Section 4.2.1, the steady-state solver cannot resolve the physics accurately

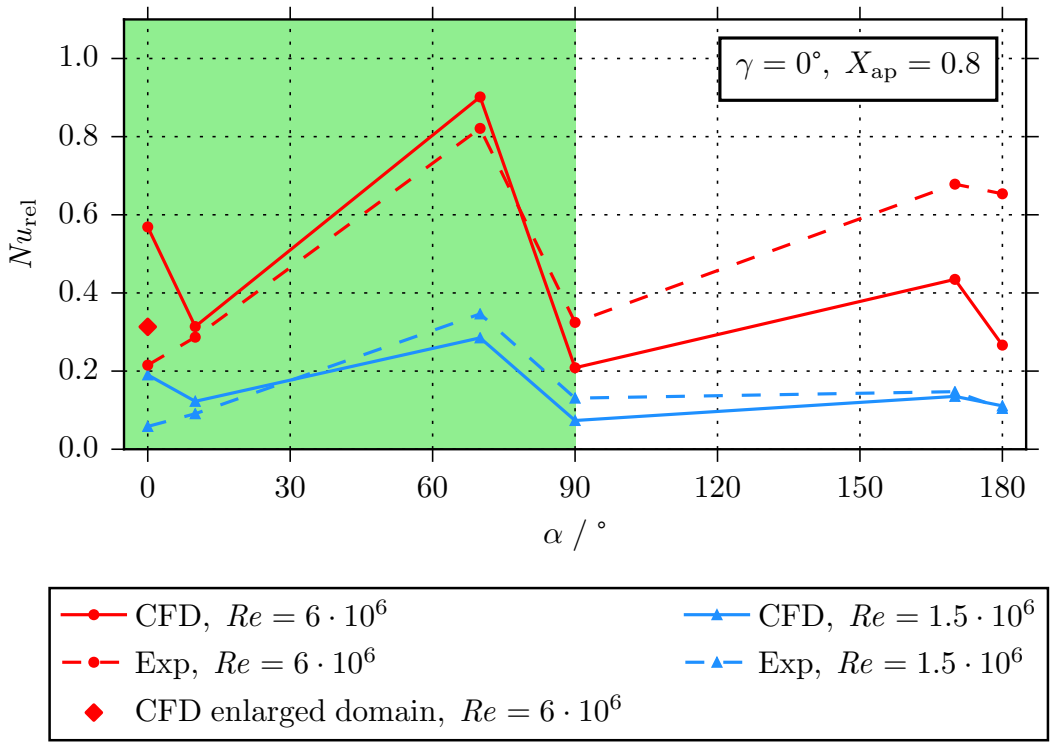

Figure 4.2.1: Comparison of the CFD results to the corresponding experimental measurements. This model had an aperture ratio of $X_{ap} = 0.8$ and a cavity inclination of $\gamma = 0°$. The CFD data were scaled to minimize the sum of the distances between the experimental and numerical values. The red diamond symbolizes the result for an enlarged domain. The green area indicates the region of trusted results.

for incident angles $\alpha > 90°$. Thus, the region of trusted results is limited to $0° \leq \alpha \leq 90°$ and hence, only simulations for $\alpha = [0°, 30°, 60°, 70°, 90°]$ were performed. The Richardson number was 0.33 at this wind speed. Next to the CFD results, also the pure free convective heat loss calculated with the Clausing model (see Eqs. 1.3.1 to 1.3.5) is shown by the grey horizontal lines.

A comparison of the 3 subfigures in Fig. 4.2.2 shows that in general the mixed convective heat loss is lower the more the cavity is inclined.

In the case of the **horizontal cavity** the mixed convective Nusselt number has its maximum of approximately 6000 at frontal winds. With increasing incident angle α the convective heat loss decreases almost linearly and reaches its minimum approximately at $\alpha = [60°, 70°]$. Thereafter, at lateral winds, the mixed convective Nu increases slightly. The difference of the maximum to the minimum is $\Delta Nu \approx 1000$. The pure free convective Nu at zero inclination was estimated to be approximately 2600. On average, the mixed convective heat loss is larger than that of pure free convection by a factor of 2.1.

For the **cavity inclined at** $\gamma = 30°$ the maximum of the mixed convective heat loss is approximately as high as the minimum in the case of the horizontal cavity, that means $Nu \approx 5000$. The data vary only moderately with different wind incident angles α, except for a reduction of approximately 10% from $\alpha = 70°$ to $\alpha = 90°$. The pure free convective Nu at the intermediate inclination was estimated to be approximately 2000. On average, the mixed convective heat loss is larger than that of pure free convection by a factor of 2.5.

The data of the **cavity inclined at** $\gamma = 60°$ are roughly 40% lower than those from the horizontal or slightly inclined cavity. Nu starts at approximately 2500 and increase to a

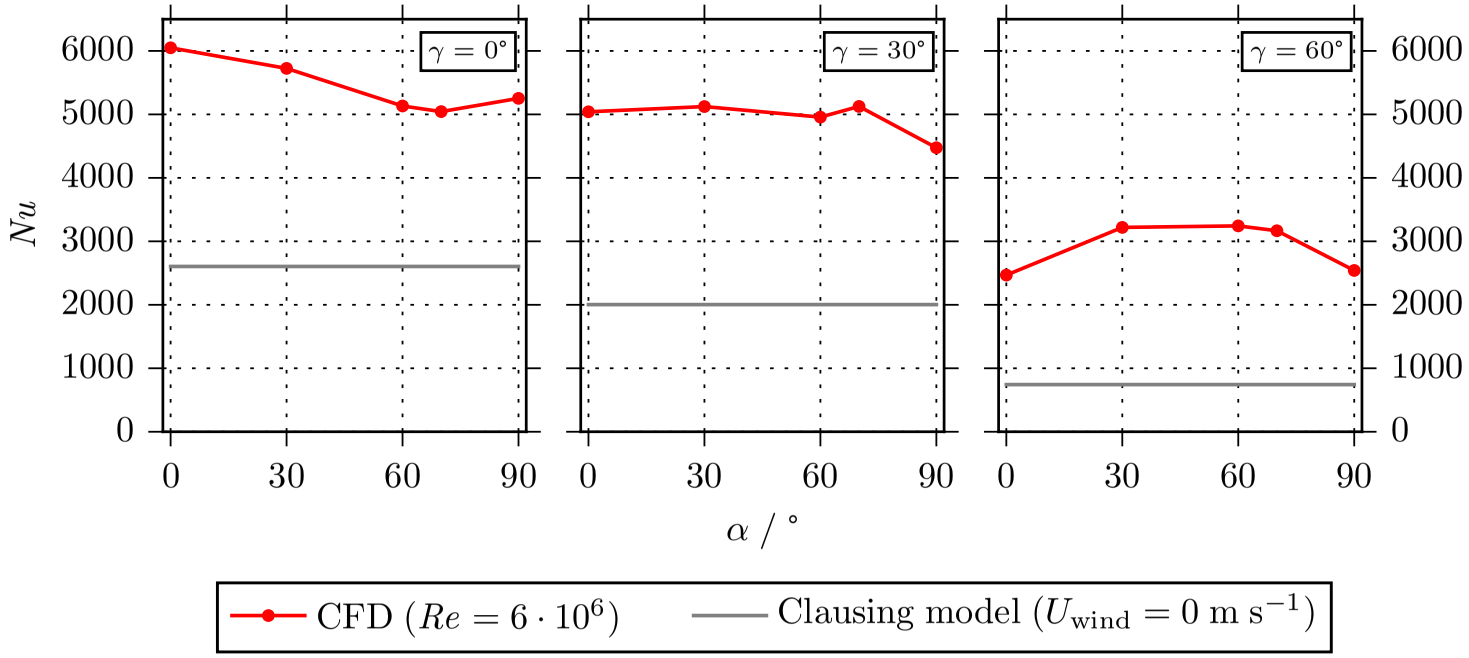

Figure 4.2.2: Mixed convective Nusselt number of the original scale model obtained with CFD simulations. The 3 models had an aperture ratio $X_{ap} = 0.8$ and cavity inclination angles $\gamma = [0°, 30°, 60°]$ from left to right. The grey horizontal lines indicate the results for pure free convection calculated with the Clausing model.

Table 4.3.1: Comparison of estimated heat losses via convection, radiation and conduction from 3 geometrical configurations: ($\gamma = 0°, X_{ap} = 0.8$), ($\gamma = 30°, X_{ap} = 0.8$), and ($\gamma = 60°, X_{ap} = 0.8$). The mixed convective heat loss is given as the maximum and the minimum of the CFD results on the original scale. The percentages indicate the relative share of each type of heat loss.

Configuration	Heat loss Convection $\dot{Q}_{conv}$ / MW	Radiation $\dot{Q}_{rad}$ / MW	Conduction $\dot{Q}_{cond}$ / MW
$\gamma = 0°,\ X_{ap} = 0.8$	8.2 to 9.8 (65% to 69%)	4.2 (29% to 33%)	0.23 (2%)
$\gamma = 30°,\ X_{ap} = 0.8$	7.3 to 8.3 (62% to 66%)	4.2 (33% to 36%)	0.23 (2%)
$\gamma = 60°,\ X_{ap} = 0.8$	4.0 to 5.3 (48% to 55%)	4.2 (43% to 49%)	0.23 (2% to 3%)

plateau between $\alpha = 30°$ and $\alpha = 70°$. At lateral winds, the mixed convective Nusselt number drops to a value close to that at frontal winds. The pure free convective *Nu* at the largest inclination was estimated to be approximately 740. On average, the mixed convective heat loss is larger than that of pure free convection by a factor of 3.9.

4.3 Estimated Radiative and Conductive Heat Losses from Cavity Receivers

This final section of the results focuses on the comparison of the estimated radiative and conductive heat losses to the mixed convective heat loss obtained with CFD simulations. The values were calculated for the 3 geometrical configurations and operating parameters as used for the original scale CFD simulations in Section 4.2.2: ($\gamma = 0°, X_{ap} = 0.8$), ($\gamma = 30°, X_{ap} = 0.8$), and ($\gamma = 60°, X_{ap} = 0.8$). The results are presented graphically in Fig. 4.3.1 and numerically in Table 4.3.1. The results include the maximum and minimum mixed convective heat loss of each geometrical configuration. The radiative and conductive heat loss were assumed to be equal for all configurations and wind speeds and were obtained via analytic expressions, see Section 3.4. In both, figure and table, the relative share of each heat loss is given.

As described in Section 4.2.2 and shown in Fig. 4.2.2, the mixed convective heat loss is reduced the more the cavity is inclined. The maximum mixed convective heat loss was 9.8 MW and the minimum was 4.0 MW. Its relative contribution to the total heat loss ranges from 48% to 69%. The radiative heat loss is in the same order of magnitude and is 4.2 MW, which translates to a relative share of between 29% and 49%. The conductive heat loss is 1 order of magnitude smaller and is only 0.23 MW, which gives a relative share of 2% to 3%.

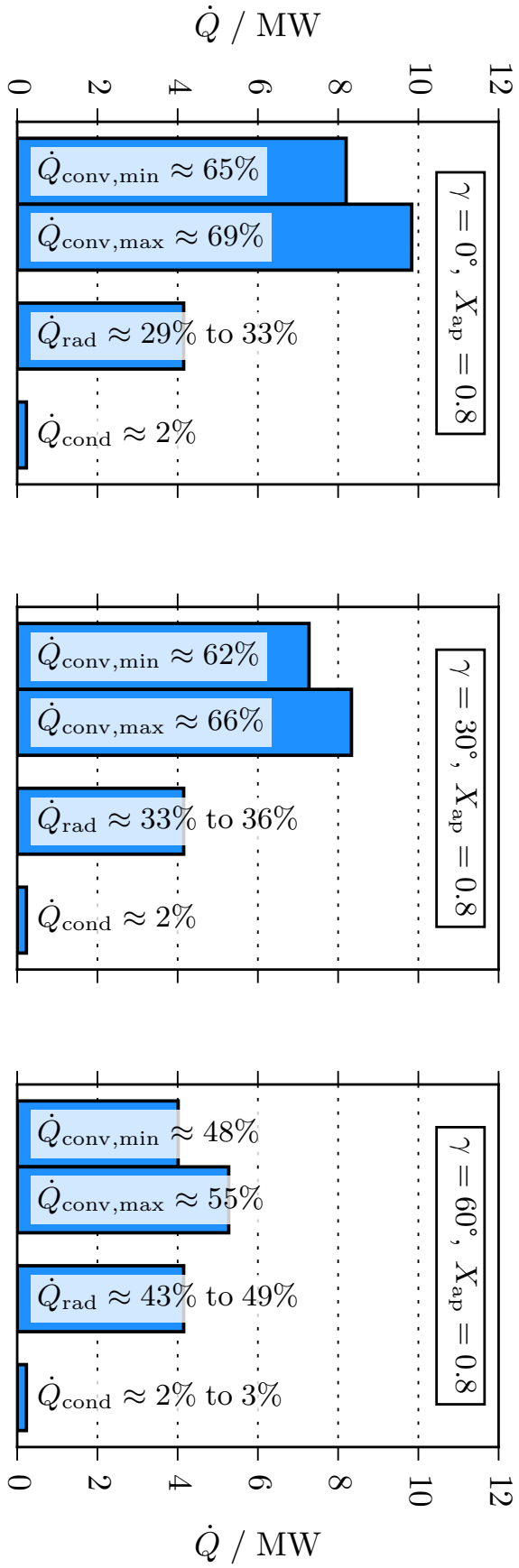

Figure 4.3.1: Comparison of estimated heat losses via convection, radiation and conduction from 3 geometrical configurations: ($\gamma = 0°, X_{\mathrm{ap}} = 0.8$), ($\gamma = 30°, X_{\mathrm{ap}} = 0.8$), and ($\gamma = 60°, X_{\mathrm{ap}} = 0.8$). The mixed convective heat loss is given as the maximum and the minimum of the CFD results on the original scale. The percentages indicate the relative share of each type of heat loss.

Chapter 5

Discussion

This discussion chapter highlights the important points of the results presented in Chapter 4. Necessary conditions are repeated and justified wherever needed. Hypotheses are established where the data allows for it and consequently, the related supportive and contradictory arguments are discussed.

The discussion starts with the influence of the wind speed and wind direction on the forced convective heat loss. It then continues with a comparison of the measured data to previously published measurements for a heated external cylinder. Thereafter, the performance of the 3 reduction measures for forced convective heat loss is discussed. The first 3 sections are based on the wind tunnel measurements only. In the fourth section, the data on forced convection obtained with CFD is compared to the measured data. This is done for integral values and also for surface values. Then, the numerical data of the mixed convection simulations on the original scale are compared to literature. In the second to last section, the relation of the mixed convective heat loss to the radiative heat loss and to the conductive heat loss on the original scale is discussed. Finally, the discussion closes with the consequence for the design of multi-megawatt CSTE cavities.

As explained in Section 3.2.1, the fluid exchange between the internal and the external flow has to be maintained when using a CTA system inside a cavity. This is to make sure that the temperature in the bulk of the internal flow corresponds to the free-stream temperature, see Eq. 3.2.2. This has been shown to be true for the present investigation, see for example Fig. 3.2.3. Thus, the forced convective heat flow measured by the hot-film sensors is a direct measure of the forced convective heat loss from the cavity to the external flow.

The reader is kindly reminded that, whenever the following discussion is based on the measured wind tunnel data only, the statements are clearly intended to be valid only in the pure forced convection regime, see Section 3.2.1 for more details.

5.1 Influence of Wind Speed and Wind Direction on the Forced Convective Heat Loss

To interpret data meaningfully the relative uncertainty has to be lower than the relative change of the data. In this work, the maximum relative uncertainty at the 3σ level is $\pm 8.2\%$. This is almost 1 order of magnitude smaller than the typical relative change of the data, see Table 4.1.1.

After having seen the results in Sections 4.1.1, 4.1.2, and 4.1.4, supposedly the most obvious hypothesis is:

Hypothesis 1 *Forced convective heat loss from a cavity is highly sensitive to the external, governing flow conditions. Specifically, this means that the forced convective heat loss from a cavity without reduction measures may be increased by (i) the wind speed by a factor of up to 2.7 and (ii) the wind direction by a factor of up to 6.1.*

The measured data presented in the 3 aforementioned sections support this first hypothesis. By dividing the values in the fifth column in Table 4.1.1, one obtains the ratio of the

maximum values which may be as high as 2.7 and 2.8 without and with reduction measures, respectively. In this table, one can also see that the max-to-min ratio is 2.6 at least and may be as high as 6.1 without reduction measures or as high as 18.1 with reduction measures. Additionally, the computed data presented in Section 4.2.1 show a substantial dependency on the wind speed and the wind direction. No contradictory data was found for Hypothesis 1.

The sensitivity to the wind direction further suggests that one has to select an increment of the wind incident angle α that is fine enough to capture the relevant phenomena of the forced convection. For example Figs. 4.1.1 and 4.1.2 indicate that the selected $\Delta\alpha = 10°$ may be adequate.

Hypothesis 1 may be refined to the more specific Hypotheses 2 to 4 concerning the studied geometrical configurations.

Hypothesis 2 *The location of the peak of the relative forced convective Nusselt number Nu_{rel} with respect to the wind incident angle α changes with the aperture ratio X_{ap}, but not with the inclination angle γ or the Reynolds number.*

This hypothesis is supported by the data in Fig. 4.1.1. In this figure, the reader may observe the peaks of the relative forced convective Nusselt numbers at all Reynolds series at $\alpha = 70°$. All geometrical configurations of this figure have $X_{\mathrm{ap}} = 0.8$, but different γ. This hypothesis is further supported by the data in Fig. 4.1.2, where $\gamma = 30°$ and X_{ap} is varied. At all Reynolds series, it can be seen that the peak shifts by $\alpha \approx 20°$ towards positive α if X_{ap} is reduced from 1 to 0.6. The only contradictory argument in this data set can be found in Fig. 4.1.2. At $Re = 1.5 \cdot 10^6$, the data do not show such a large shift in α for the peak location. This seems to be caused by a broader peak in the rightmost subfigure, where $X_{\mathrm{ap}} = 0.6$. However, this data do not contradict the general trend, but only exhibit the trend less strongly.

In the next hypothesis, I try to generalize the forced convective heat loss characteristics with respect to the absolute incident angle χ, where $\chi = f(\alpha, \gamma)$. This hypothesis stems from theoretical considerations; since the flow is in the pure forced convection regime and the cavity is axisymmetric, the flow is expected to behave similarly for similar χ, no matter what combination of α and γ leads to that χ.

Hypothesis 3 *The change in forced convective heat loss from a cavity for wind incident angles $\alpha \leq 90°$ due to a change in the absolute incident angle χ can be estimated with $Nu_{\mathrm{rel}} = f_1(\chi)$.*

This hypothesis is mainly supported by the data in Fig. 4.1.4. One can see that for each Reynolds series the data follow closely a similar, almost linear trend. Interesting to note is that the data has a different slope for different Reynolds numbers, but all series have an inflection point at $\chi \approx 70°$. The data after the inflection point show a larger spread, this might be caused by the increasing influence of the tower for larger α and thus larger χ. This hypothesis should be tested for $X_{\mathrm{ap}} \neq 0.8$ in a future investigation.

On the basis of the absolute incident angle, the data was analyzed with respect to Reynolds number dependency. It was shown in Section 4.1.6 that the data can be fitted with a power law that has a one-fits-all exponent. That exponent corresponds well with literature data. Thus, this analysis supports Hypothesis 4.

Hypothesis 4 *The change in forced convective heat loss from a cavity for wind incident angles $\alpha \leq 90°$ due to a change in the Reynolds number can be estimated with $Nu_{\mathrm{rel}} = f_2(Re)$.*

Remarkable is that this analysis was performed with a Reynolds number on the basis of the cavity diameter and the free-stream properties. Since the agreement with literature is good, one may conclude that the external Reynolds number is a good indicator of the internal Reynolds number. What is needed to link these 2 Reynolds numbers is a function of χ. This can be seen in Fig. 4.1.5, where the slopes are the same for all χ, but each curve has a different preexponential constant, depending on χ. To further validate this hypothesis it should be tested for $X_{ap} \neq 0.8$. An interesting approach is the combination of Hypotheses 3 and 4 into 1 single function for the forced convective heat loss: $Nu_{rel} = f_1(\chi)f_2(Re)$. A first attempt to find a function $f_2(Re)$ was presented in Fig. 4.1.5. In a next step, function $f_1(\chi)$ could be fitted to the preexponential factors.

When discussing Hypothesis 3, the effect of the tower has been mentioned. Now, an attempt to grasp this effect more thoroughly is made in the next hypothesis.

Hypothesis 5 *The existence of a tower does not cause a substantial shift in the location of the peak value of the relative forced convective Nusselt number Nu_{rel} with respect to the wind incident angle α.*

Supportive arguments come from a comparison to previous experimental and numerical studies published in Flesch et al. (2014), Flesch et al. (2015), Flesch (2016), and Flesch et al. (2016). As in the present work, in those studies an axisymmetric cavity was used as well, but without a tower. In addition, those studies were performed with mixed convection, for smaller cavities, $X_{ap} = 0.55$, and with $\Delta\alpha = 30°$. Thus, the comparison has to be made with caution. What can be compared well are the curves for a fixed inclination, but different wind speeds and wind incident angles. It is safe to assume that the variation of these curves is caused by the forced convection contribution. In the cited works, the maximum is always located at $\alpha = 90°$. Comparing it to the measured value of the closest matching geometrical configuration of this work, which is ($\gamma = 30°, X_{ap} = 0.6, Re = 1.5 \cdot 10^6$), shows that $\Delta\alpha \approx 10°$ towards negative α in the present work. It is difficult to say whether this shift is caused by the presence of the tower when at the same time the resolution of α in the cited works is larger than the $\Delta\alpha$ discussed here. Support for Hypothesis 5 can also be found in the arguments for Hypothesis 2; the trend of the peak location observed in Fig. 4.1.2 leads to an expectation that for even smaller X_{ap} the peak shifts towards higher α.

5.2 Comparison to the Forced Convective Heat Loss from a Heated External Cylinder

The author and colleagues published a short comparison to the measured forced convective heat loss from a heated external cylinder in Siegrist et al. (2018b). The measurement campaign with the heated external cylinder was published by Achenbach (1977). He measured the local forced convective heat loss from a heated circular cylinder to the cross flow of air up to a Reynolds number of $Re = 4 \cdot 10^6$. In Fig. 5.2.1, the test series of Achenbach with the highest Reynolds number is compared to the closest matching test series of this work ($\gamma = 0°, Re = 3 \cdot 10^6$). Since the Reynolds number of this work is based on the cavity diameter, it has to be multiplied by 4/3 to give a Reynolds number which is based on the external cylinder or tower diameter. The curves are scaled to minimize the sum of the distances.

In this figure, it is remarkable that for comparable Reynolds numbers the qualitative behavior of the forced convective heat loss match well, especially for the following 4 characteristics. Firstly, Achenbach reported a steady rise of the heat loss until a peak at

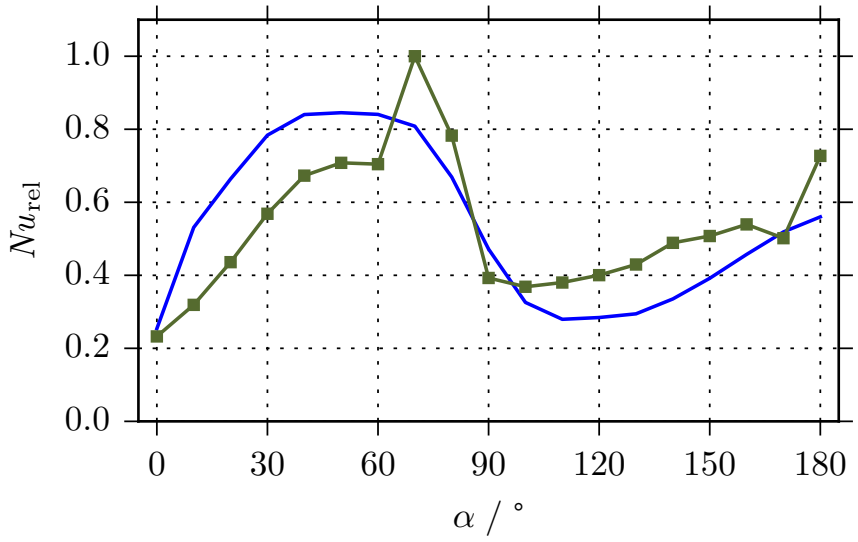

Figure 5.2.1: Comparison of the forced convective heat loss from an external heated cylinder (blue curve) at $Re = 4{\cdot}10^6$ (data: Achenbach (1977)) to the measured data at ($\gamma = 0°, X_{ap} = 0.8, Re = 3{\cdot}10^6$) of this work (green curve with square markers). The curves are scaled to minimize the sum of the distances. Remark: This work's Reynolds number has to be multiplied by 4/3 to change the characteristic length to be the cylinder diameter.

$\alpha \approx [50°, 60°]$. Secondly, he reported max-to-min ratios of approximately 4. Thirdly, for lateral winds he observed a large drop in heat loss. And fourthly, for $\alpha \geq 120°$ he reported an increase again in the forced convective heat loss. All 4 observations can also be made in this contribution, see Table 4.1.1 and Fig. 5.2.1. It can be observed that the resulting curves are less smooth than the ones obtained by Achenbach. This is explained due to the protruding cavity in this work which may cause a more complex flow behavior. The visualizations obtained with the BOS setup may explain this sharp peak well, see Section 4.1.7. The mentioned arguments lead to Hypothesis 6.

Hypothesis 6 *The qualitative behavior of the forced convective heat loss from a cavity with inclination angle $\gamma = 0°$ and an external cylinder is similar for similar Reynolds numbers.*

The phenomena observed and reported by Achenbach (1977) may be adapted to forced convective heat loss from cavities. By doing so one may arrive at the following description of the governing flow: (i) the displacement of the flow due to the cavity and the tower causes the flow to accelerate and the heat transfer to increase along the external surface from the stagnation point until the separation point is reached and the flow detaches; (ii) the transition to a turbulent boundary layer causes the exchange of mass and heat to increase substantially; (iii) the separation of the flow causes an abrupt deceleration in the boundary layer for downstream regions which decreases the heat transfer considerably; (iv) the wake increases the heat transfer of the downstream section due to the fluctuations close to the surface; and (v) the deflection of the flow is caused by the aperture plane and the tower and effects that the flow in front of the aperture may have a different direction than the incident wind. This explanatory framework is also translated graphically in Fig. 5.2.2, where the red dot marks the stagnation point, the red dash marks the boundary layer transition point, and the red triangle marks the separation point where the flow detaches from the surface. This explanatory framework may be condensed to the following hypothesis:

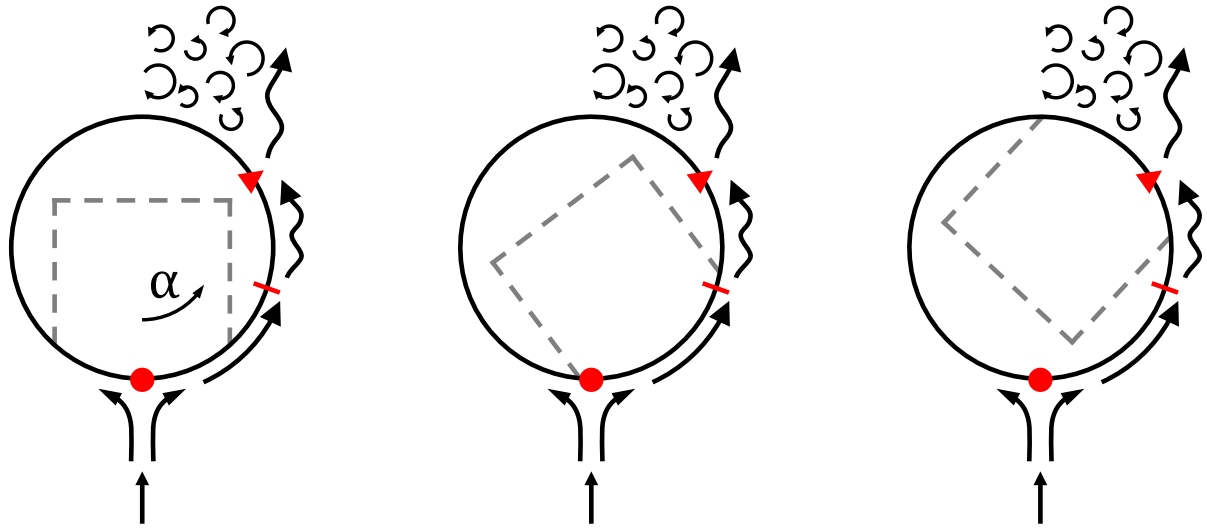

Figure 5.2.2: Illustration of the forced convective heat loss mechanisms. The flow passes the stagnation point (red dot), accelerates along the cylinder surface and transitions to a turbulent boundary layer at a point marked with the red dash, and finally detaches from the surface at the separation point (red triangle). The grey dashed lines indicate a symbolic cavity. For the sake of clarity, only one half of the flow is considered.

Hypothesis 7 *The external, governing flow characteristics for forced convective heat loss from a cavity are defined by the displacement, separation, wake, and deflection of the external flow due to the aperture and the tower as well as by the turbulent transition of the boundary layer on the outside of the cavity and the tower.*

The last hypothesis in this section is emphasizing that the flow characteristics that govern the forced convection inside the cavity is most important very close to the aperture.

Hypothesis 8 *Forced convective heat loss from a cavity is governed by the external flow characteristics in direct vicinity of the aperture opening.*

This hypothesis is supported primarily by reasoning based on fluid dynamics. Without an external driving force, the fluid in the cavity would stand still because it is in the pure forced convection regime. The only way to transfer momentum to the internal flow, and thus accelerate the fluid in the cavity, is by viscous and pressure forces that act across the aperture opening. Thus, it becomes immediately clear that the flow characteristics in direct vicinity of the aperture define the flow characteristics inside the cavity. Additional support for this hypothesis can be found in the visualized data obtained by the BOS setup, see Fig. 4.1.6. In this figure, one can see that when the zone of large pixel shift is of lower magnitude and when it has moved away from the aperture, then the resulting heat loss in the left subfigure of Fig. 4.1.1 is lower, too.

5.3 Comparison of the Performance of the Three Reduction Measures

The measured data of the 3 reduction measures in Fig. 4.1.3 has to be related to the data in Fig. 4.1.1 (left). Whenever the forced convective heat loss with 1 of the reduction measures in the first figure is lower than that of the reference case in the latter figure the forced convective heat loss from the cavity is reduced. This comparison is plotted in Fig. 5.3.1

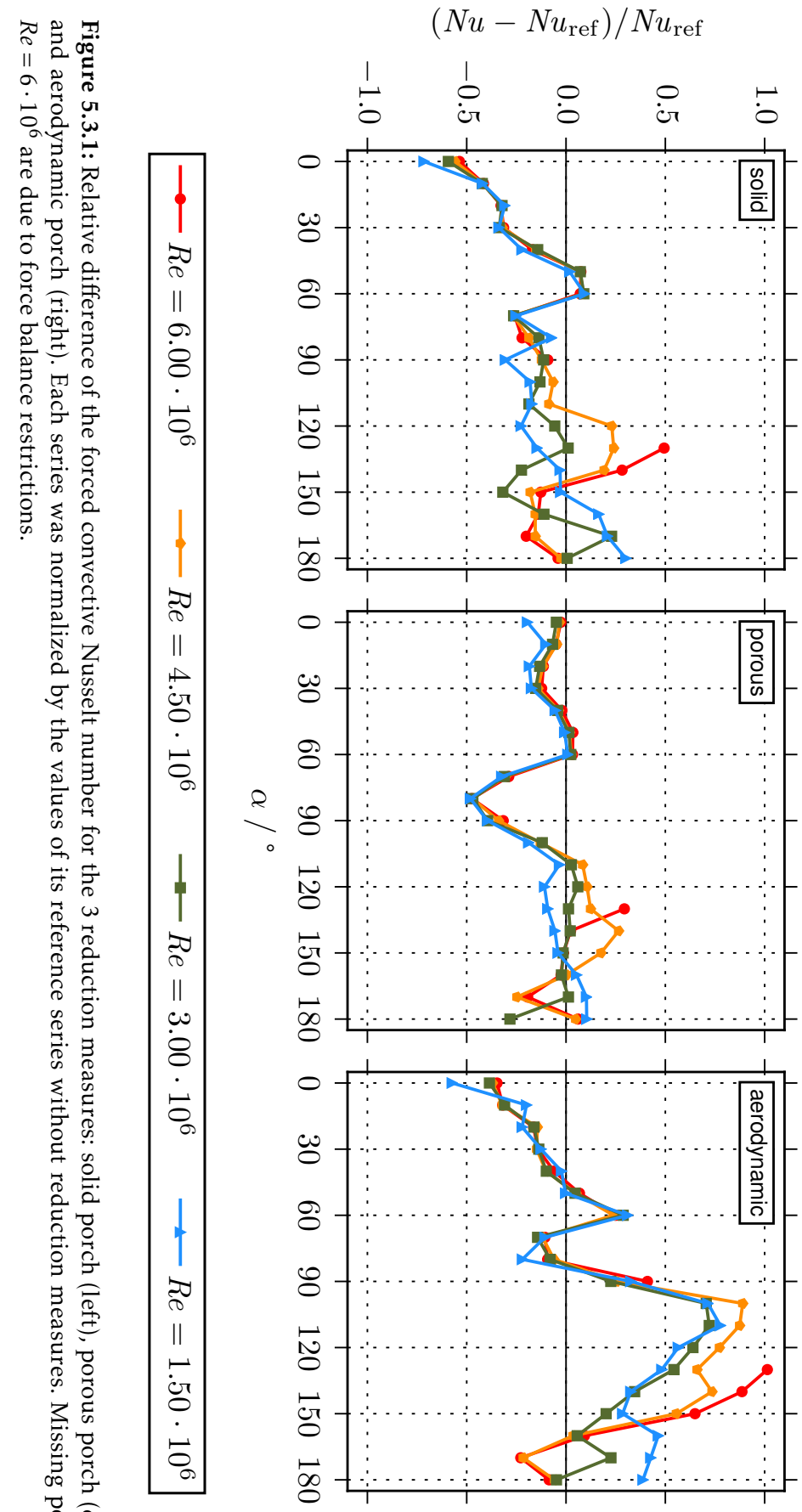

Figure 5.3.1: Relative difference of the forced convective Nusselt number for the 3 reduction measures: solid porch (left), porous porch (center), and aerodynamic porch (right). Each series was normalized by the values of its reference series without reduction measures. Missing points at $Re = 6 \cdot 10^6$ are due to force balance restrictions.

as the **relative reduction potential** $(Nu - Nu_{\mathrm{ref}})/Nu_{\mathrm{ref}}$. Negative values indicate reduction, positive values indicate increase. For each of the 3 reduction measures the trend is similar for all Reynolds number series until the maximum of the relative forced convective Nusselt number Nu_{rel}. Thereafter, the reduction characteristics depend heavily on Re and the spread of the relative reduction potential is larger. It is interesting to note that the solid porch performs exceptionally well for $\alpha \leq 40°$. For winds from such frontal directions, the downstream face of the cone of the porch still deflects some of the wind in the aperture plane and decelerates the wind speed in front of the aperture which might cause the relative reduction in forced convective heat loss. This effect is expected to happen as long as the incident angle is lower than the cone angle of the solid porch (which is 45°). For winds with $\alpha = [70°, \ldots, 100°]$ the porous porch has a relative reduction potential of up to −50%. At those angles, the velocity in front of the aperture is expected to be at maximum because the forced convective heat loss without a reduction measure is at maximum, too. As it was reasoned earlier in this work, this can be explained by the coupling of the internal and external flow across the aperture. As explained in Section 3.2.1.4, the porous porch reduces the momentum of the flow due to a pressure drop which is proportional to the square of the velocity. This reasoning could explain the highly effective mechanism of the porous porch at angles around where the forced convective heat loss is at maximum. For all other angles, the porous porch seems to perform similarly well as the reference case. The aerodynamic porch does not seem to be a good reduction measure for forced convective heat loss, except for $\alpha \leq 40°$. At such small α, the aerodynamic porch is expected to follow the same principles as the solid porch. When $\alpha = [70°, 80°]$, the forced convective heat loss is reduced moderately. For winds with $\alpha = [90°, \ldots, 150°]$, the aerodynamic porch increases the forced convective heat loss by a factor of up to 2. This might be explained by the nozzle effect which collects, deflects, and accelerates the fluid that comes from lateral directions, see Fig. A.6 for a drawing of the aerodynamic porch. This nozzle effect was intended by design, see Section 3.2.1.4. If this increase is caused by the nozzle, then it could possibly mean that this reduction measure could be effective in producing a passive aerowindow, which is a proven reduction measure (see Flesch (2016)). To validate the effectiveness of this reduction measure it should be investigated in detail in future research.

Similar to Fig. 5.3.1, the performance of the reduction measures is plotted again, this time in form of the **absolute reduction potential** $Nu - Nu_{\mathrm{ref}}$ in Fig. 5.3.2. One can clearly see that the trends for all 3 reduction measures remain the same. Interesting to note is that the porous porch performs exceptionally well for wind coming at $\alpha = [70°, 80°]$.

In Table 5.3.1 the absolute reduction performance averaged over the wind incident angle α is presented. One can see that both, for the solid and the porous porch the direction-averaged mean is negative, indicating a reduction. For the aerodynamic porch positive values result which means that the forced convective heat loss increases when the wind blows from each direction with the same likelihood.

The arguments brought up in this section can be condensed into 1 hypothesis for each of the 3 reduction measures. The first 1 is for the solid porch.

Hypothesis 9 *The solid porch effectively reduces the forced convective heat loss mainly for wind incident angles $\alpha \leq 40°$. For $\alpha > 40°$, the reduction performance is ambiguous.*

The effects described in this hypothesis can also be explained by using Hypotheses 7 and 8 and state that if the reduction measure is able to reduce the velocity in the aperture plane by means of deflection or separation then the forced convective heat loss is also reduced. As explained in the beginning of this section, it is expected that this mechanism is effective in this case.

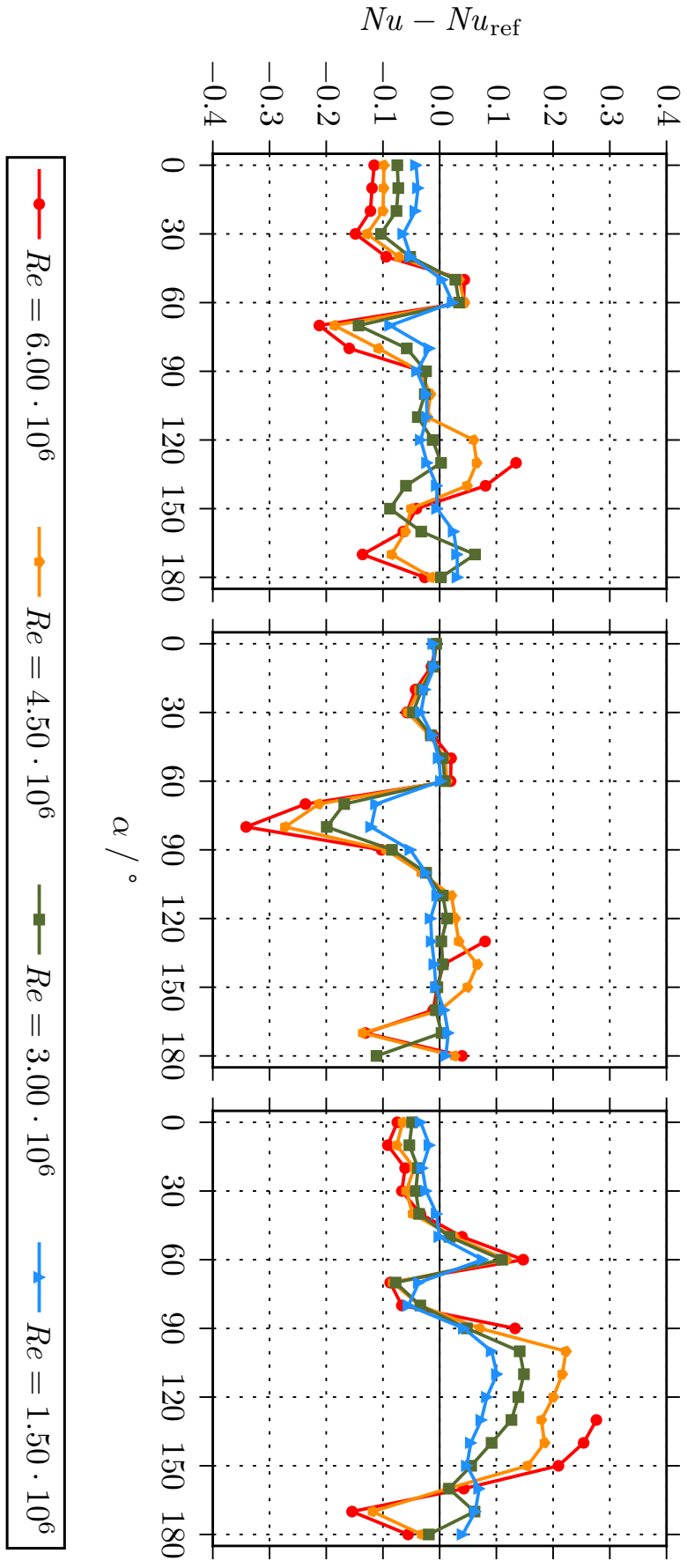

Figure 5.3.2: Absolute difference of the forced convective Nusselt number for the 3 reduction measures: solid porch (left), porous porch (center), and aerodynamic porch (right). Missing points at $Re = 6 \cdot 10^6$ are due to force balance restrictions.

Table 5.3.1: Mean absolute reduction of the forced convective Nusselt number due to the 3 reduction measures with ($X_{ap} = 0.8, \gamma = 0°$). Some points at $Re = 6.0 \cdot 10^6$ could not be measured due to force balance restrictions.

Subfigure	Aperture	Reynolds number Re	Mean performance
Figs. 5.3.2 left 3.2.11a	solid	$1.5 \cdot 10^6$	−0.021
	solid	$3.0 \cdot 10^6$	−0.040
	solid	$4.5 \cdot 10^6$	−0.046
	solid	$6.0 \cdot 10^6$	−0.063†
Figs. 5.3.2 center 3.2.11b	porous	$1.5 \cdot 10^6$	−0.021
	porous	$3.0 \cdot 10^6$	−0.033
	porous	$4.5 \cdot 10^6$	−0.032
	porous	$6.0 \cdot 10^6$	−0.047†
Figs. 5.3.2 right 3.2.11c	aero	$1.5 \cdot 10^6$	+0.025
	aero	$3.0 \cdot 10^6$	+0.028
	aero	$4.5 \cdot 10^6$	+0.038
	aero	$6.0 \cdot 10^6$	+0.020†

†These values should be used with caution, since they are calculated from a partially incomplete data series.

Hypothesis 10 *The porous porch effectively reduces the forced convective heat loss mainly for wind incident angles $\alpha = [70°, \ldots, 100°]$. For α outside this interval, the reduction performance is almost inexistent.*

The mechanism that supports this hypothesis was reasoned earlier in this section and can also be linked to Hypotheses 7 and 8; the porous porch does not cause deflection or separation of the flow, it only reduces the momentum, especially for high wind speeds.

Hypothesis 11 *The aerodynamic porch reduces the forced convective heat loss for wind incident angles $\alpha \leq 40°$. For $\alpha = [90°, \ldots, 150°]$, the aerodynamic porch increases the forced convective heat loss which is due to high wind speeds in the aperture, caused by the nozzle effect.*

Also this last hypothesis can be supported with the reasoning stated in Hypotheses 7 and 8. At the wind incident angles where the nozzle has an effect, the generated wind jet is parallel to the aperture plane and passes the aperture in direct proximity. Thus, it can accelerate the fluid in the cavity effectively which generates additional forced convective heat loss. In the case of mixed convection, such an aerowindow has been shown to result in an effective passive reduction of the mixed convective heat loss, see for example Flesch (2016). As a consequence, this observation suggests the following hypothesis.

Hypothesis 12 *The aerodynamic porch generates a passive aerowindow that might reduce the convective heat loss in the case of mixed convection.*

To test this hypothesis further experiments have to be performed in the mixed convection regime. In such a study, it has to be tested whether the jet that is observed in this experiment is also established in a mixed convection regime and hence reduces the mixed convective heat loss.

5.4 Comparison of the Experimental and Numerical Data on Forced Convection

The numerical data which was presented in Section 4.2 is discussed hereafter. A direct comparison of the wind tunnel measurements and their 1:1 simulations in CFD is presented. This is done for both, the integral values and the surface values.

5.4.1 Comparison of the Integral Values

The order of magnitude of the deviation of the numerical data from the experimental data is smaller than the order of magnitude of the change in Nu_{rel} reported in Fig. 4.2.1. This means that the numerical data can be interpreted meaningfully.

In Fig. 4.2.1, one can clearly see that for $\alpha \leq 10°$ the simulated data deviate strongly from the measured data. By post-processing the data it was found that this effect is due to the flow attaching to 1 side of the domain, although such small incident angles should not give rise to such a strong attachment. This effect almost completely vanishes by enlarging the domain. It is suspected that this effect would also not be relevant if a transient CFD model is used, as it is done for example in Flesch (2016). Here, it means that the values for $\alpha \leq 10°$ have to be treated with caution.

From Fig. 4.2.1 it can further be deduced that for $\alpha > 90°$ the simulated data also deviate from the measured data. As described in Section 4.2.1, this is expected, since a steady-state solver cannot resolve accurately fluctuating characteristics such as a vortex street. For the remaining frontal wind directions, the experimental and the numerical data match. Thus, for this work the following hypothesis is formulated.

Hypothesis 13 *CFD simulations based on steady-state RANS may give valid forced convective heat loss values that are close to measured data, in the case of wind incident angles* $\alpha \leq 90°$.

5.4.2 Comparison of the Surface Values

In this section, locally resolved values on the cylindrical part of the cavity are discussed. For a comparison to measurements, 3 wind incident angles $\alpha = [10°, 70°, 90°]$ are selected and the results of the CFD simulations are shown in Fig. 5.4.1 for a configuration of $(\gamma = 0°, X_{\mathrm{ap}} = 0.8, Re = 6 \cdot 10^6)$. The corresponding results of the measurements are shown in Fig. 5.4.2 for the same incident angles and configuration. The Nusselt numbers are fixed at the maximum of the simulations and the measurements, respectively. Please note the slightly different definition of the Nusselt number for the CFD results as defined in Eq. 3.3.3 and for the measurements as defined in Eq. 3.2.20. In Figs. 5.4.1 and 5.4.2, the very low values at $\varphi = 0$ (cavity top) and $\varphi = \pi$ (cavity bottom) are clearly visible. These 2 regions are interpreted as being the pivotal regions of the internal flow. This is supported by both center subfigures which both show maxima at $\varphi = \pi/2$ (cavity left) and $\varphi = 3\pi/2$ (cavity right). These 2 regions can consequently be interpreted as the regions with the highest wind speeds due to the fact that the tangential speed of a rotating fluid increases with increasing distance from the rotational axis. Simplifying the internal flow as 1 single eddy that fills almost all of the cavity and rotates with an angular velocity can help to understand the heat transfer characteristics in pure forced convection. The driving force that controls the angular velocity of this internal flow is the transfer of momentum across the aperture from the external flow as described in Hypothesis 7. On the basis of the above arguments a new hypothesis is formulated.

Hypothesis 14 *In pure forced convection, the internal flow in a cavity can be considered as 1 single eddy.*

The subfigures in Fig. 5.4.1 suggest that there may be smaller secondary flow structures close to the edges at the front and back of the cavity for ($\varphi = [\pi, \ldots, 2\pi], z \approx 0$) and ($\varphi = [0, \ldots, \pi], z \approx 1$). It is interpreted that these flow structures are fluid streams that hit the cavity wall at ($\varphi = 3\pi/2, z \approx 0$) and ($\varphi = \pi/2, z \approx 1$) and are deflected along the cavity surface in positive and negative direction of φ.

5.5 Comparison of the Numerical Data on Mixed Convection to Literature

As can be seen in Fig. 4.2.2, the pure free convective heat loss is always lower than the mixed convective heat loss. It is assumed that the Clausing model is valid and accurate, as shown in Section 1.3. The difference between the free and mixed convective heat loss indicates that the forced convective heat loss contributes considerably to the mixed convective heat loss. The additional part due to forced convection also increases in relative terms with increasing inclination angle γ, as reported in Section 4.2.2. These observations lead to the next hypothesis.

Hypothesis 15 *For cavities on the multi-megawatt scale the forced convective heat loss always contributes substantially to the mixed convective heat loss. The relative increase is larger the more the cavity is inclined.*

The more the cavity is inclined the more of the fluid inside the cavity is in the stagnant zone. Now, if wind approaches a strongly inclined cavity this wind has a higher chance to displace hot fluid in the stagnant zone than if the same wind hits a cavity with less inclination. This may explain the increased relative importance with increased inclination. A similar reasoning was already presented in Flesch (2016).

A comparison of the measured data (Fig. 4.1.1) to the simulated data on the original scale (Fig. 4.2.2) does not allow for a clear and general deduction of the characteristics of mixed convective heat loss from the characteristics of pure forced convective heat loss. Although the simulations were performed with $Ri = 0.33$, the qualitative behavior of the forced convective heat loss is not anymore visible in the mixed convective heat loss. However, as stated in Hypothesis 15, the forced convection does still have a large impact. Interesting is that for $\gamma = 0°$ the characteristics of the forced convection experiments and of the mixed convection simulations show slightly complementary trends. This might be due to the increasing flow in front of the aperture for increasing wind incident angles, which enhances the convection in the forced convection case but might reduce the convection in the mixed convection case due to an aerowindow. Flesch et al. (2016) reported that this reduction measure has a larger reduction potential for less inclined cavities. This might also explain why there is no correlation between the forced and mixed convective heat loss trends for $\gamma = [30°, 60°]$.

The results of the original scale simulation can also be compared to a previous work by Flesch (2016). The simulations that match the CFD models in Fig. 4.2.2 best had $Ri \approx 0.28$ and $Re = 3.7 \cdot 10^5$. The simulations were also done for $\gamma = [0°, 30°, 60°]$, but with $X_{\mathrm{ap}} = 0.55$ and $d_{\mathrm{cav}} \approx 2.4\,\mathrm{m}$. In general, the mixed convective Nusselt number reported by Flesch is about 1 order of magnitude lower. This is expected, because the Nusselt number scales with the characteristic length. Noteworthy is that the results in the previous experiment support only the second part of Hypothesis 15. The first part is not supported because the mixed convective heat loss at $\gamma = 0°$ is roughly equal to the contribution of the pure free convection. This stands in contrast to the results in Fig. 4.2.2, where the mixed convective heat loss lies roughly a factor of 2 above the free convective heat loss. Another relevant

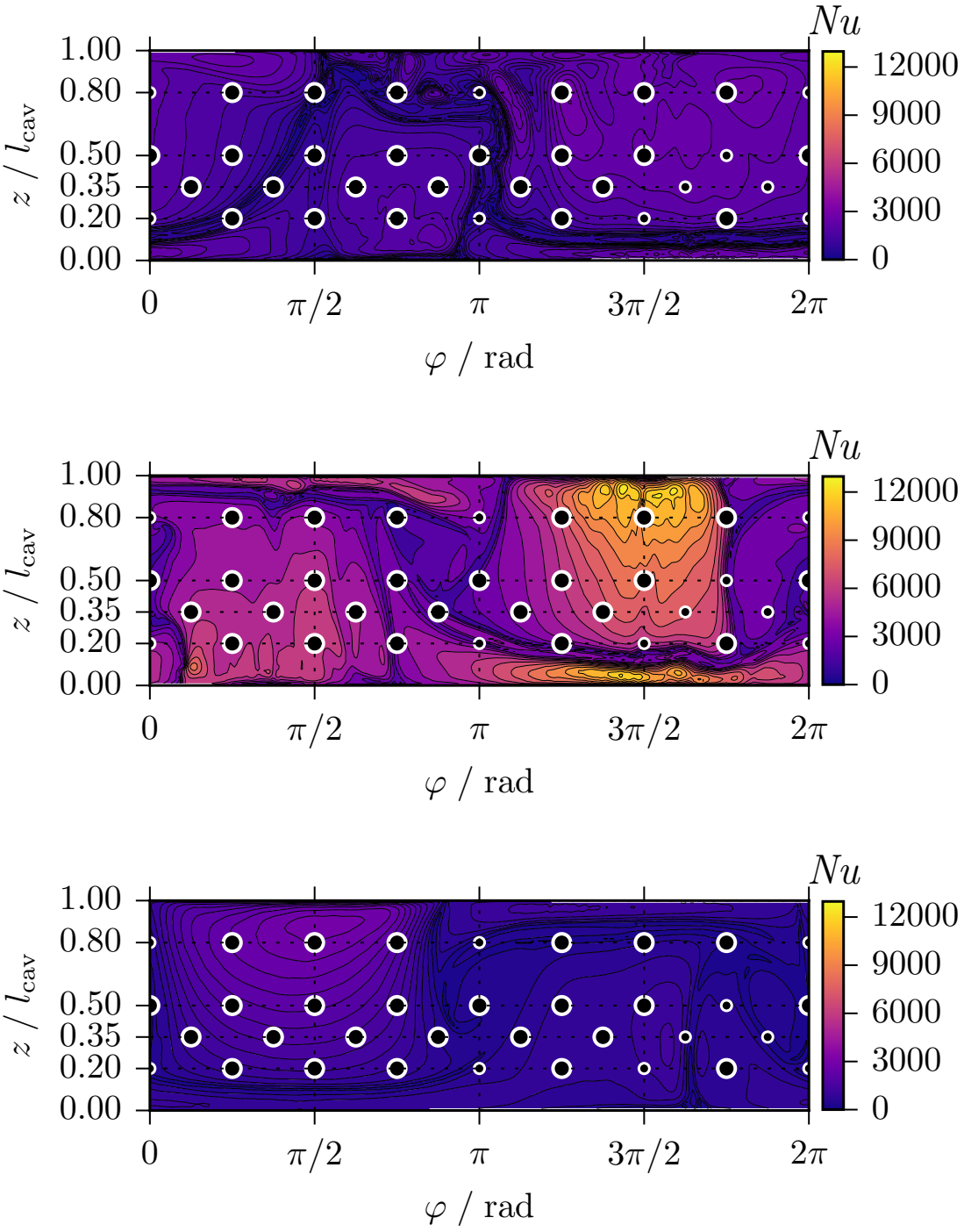

Figure 5.4.1: Iteration-averaged local *Nu* based on the CFD simulation data on the cylindrical surface of the cavity. The 3 subfigures represent $\alpha = [10°, 70°, 90°]$ from the top to the bottom at a configuration of ($\gamma = 0°, X_{ap} = 0.8, Re = 6 \cdot 10^6$). For easier comparison to the data in Fig. 5.4.2, the locations of the working sensors are indicated by large dots and those of the broken sensors are indicated by small dots.

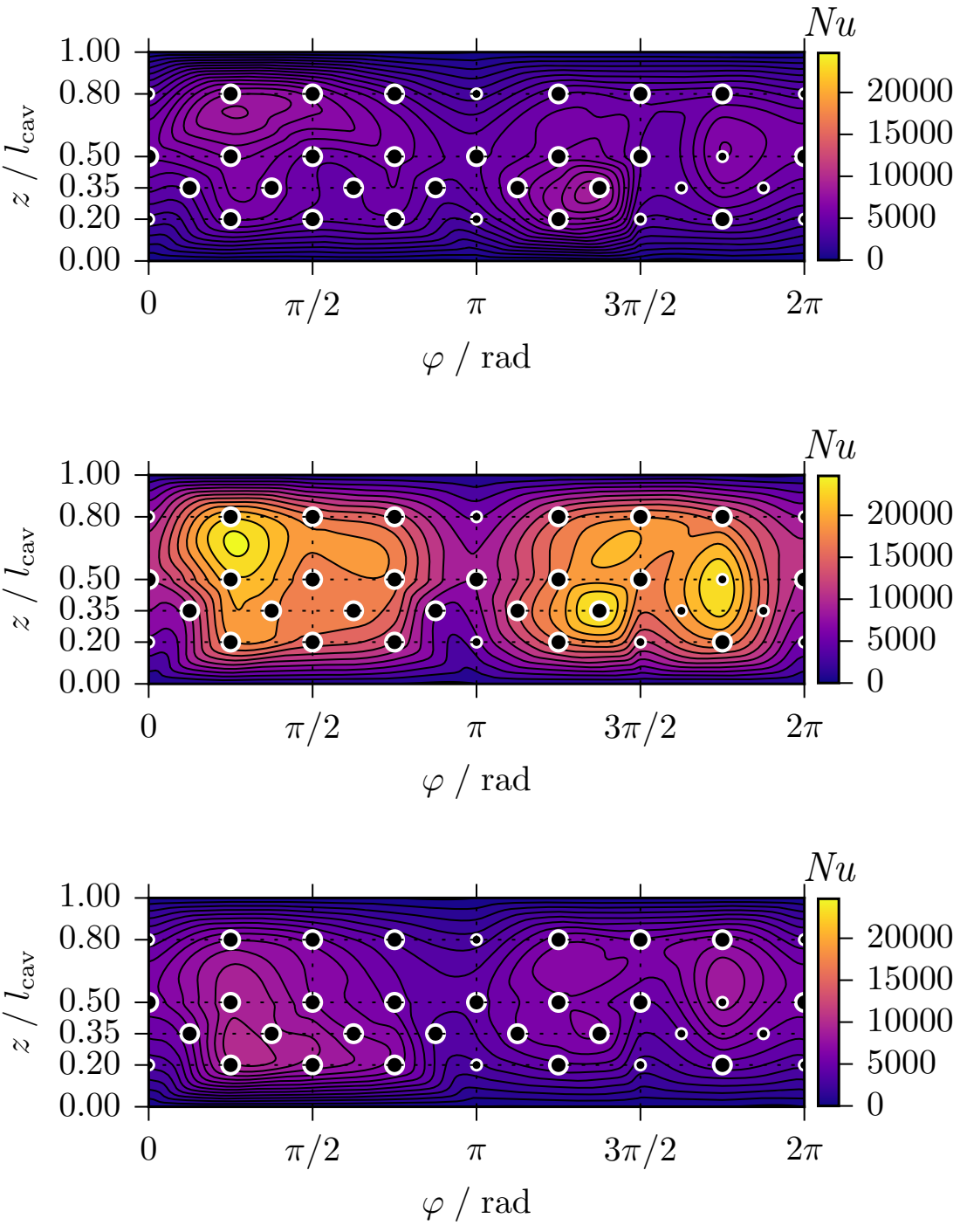

Figure 5.4.2: Local *Nu* based on the measured data which were interpolated with a cubic spline method on the whole cylindrical surface of the cavity. The 3 subfigures represent $\alpha = [10°, 70°, 90°]$ from the top to the bottom at a configuration of ($\gamma = 0°, X_{ap} = 0.8, Re = 6 \cdot 10^6$). Large dots represent the working sensors, small dots represent the broken sensors.

study was done by Clausing et al. (1989). The receiver used in that study was of square geometry and had a height of 1.2 m. Their findings were that when $Ri > 0.2$ the forced convection contribution is negligible. A third study was performed by Ma (1993). A cylindrical cavity with $d_{cav} = 0.66\,m$ and a conical end was used. It was reported that for $Ri \lesssim 0.5$ the forced convective heat loss contributes substantially to the mixed convective heat loss. As a conclusion, the present work supports previous works in so far that below a specific value of the Richardson number the forced convective heat loss contributes significantly to the mixed convective heat loss. The results of the present work indicate that the exact value may depend not barely on the Richardson number but on a combination of the Richardson number with either the Reynolds number or the Grashof number. Since the size of the cavity in the present work is considerably larger than in the previous works, the aforementioned conclusion suggests the following hypothesis.

Hypothesis 16 *In larger cavities, the contribution of the forced convective heat loss to the mixed convective heat loss is larger than for smaller cavities at the same Richardson number.*

5.6 Relation of the Mixed Convective Heat Loss to the Total Heat Loss

In Section 4.3, the results from simulations and estimations were shown in order to relate the mixed convective heat loss for $Re = 6 \cdot 10^6$ to the radiative and conductive heat losses. In all 3 cases, the conductive heat loss plays only a minor role and the mixed convective heat loss is at least as large as the radiative heat loss. For $\gamma = 0°$ the mixed convective heat loss is more than twice the radiative heat loss. For $\gamma = 30°$ the mixed convective heat loss is still almost twice as big as the radiative heat loss. Only in the case of $\gamma = 60°$ the mixed convective heat loss is of the same order of magnitude. This directly gives the following hypothesis.

Hypothesis 17 *The mixed convective heat loss from large cavities with inclination angles* $\gamma = [0°, 30°, 60°]$ *at the Reynolds number* $Re = 6 \cdot 10^6$ *is at least of the same order of magnitude as the radiative heat loss. At maximum, it can be up to twice as large as the radiative loss. The conductive heat loss may be neglected.*

If the operating temperature is increased, the mixed convective heat loss is expected to change proportionally with the temperature. Since the emitted radiation is proportional to the fourth power of the operating temperature, the relative weight may shift in favour of the radiative heat loss if the operating temperature is increased.

5.7 Consequences for the Design of Multi-Megawatt CSTE Cavities

The data presented in Figs. 3.1.3a to 3.1.3c point out that the predominant wind direction differs for each site. This observation is now combined with the insights (i) that a major share of the total heat loss from large cavities is the mixed convective heat loss (Section 5.6); (ii) that in turn the mixed convective heat loss exhibits a substantial contribution of the forced convective heat loss (Section 5.5); (iii) that the forced convective heat loss might be reduced through adequate reduction measures (Section 5.3); and (iv) that the forced convective heat loss is highly sensitive to the wind direction and the wind speed (Section 5.1). Then, the following final hypothesis may be formulated:

Hypothesis 18 *The optimization of the design of a multi-megawatt CSTE cavity receiver with respect to convective heat loss is possible when a specific site is given and its meteorological boundary conditions are well known.*

Chapter 6

Conclusions

In this chapter, the findings presented in Chapter 4 and discussed in Chapter 5 are reviewed and summarized to give a concise overview of the contribution of the present thesis to the field of convection.

At this stage, 2 important remarks are recalled:

- The condition stated in Section 3.2.1 and defined in Eq. 3.2.2 requires the fluid to be exchanged sufficiently across the aperture. This condition is met in this work. Consequently, the relative forced convective Nusselt number is directly proportional to the relative forced convective heat loss.

- Whenever the following conclusions are based on the measured wind tunnel data only, the statements are clearly intended to be valid only in the pure forced convection regime ($Ri \ll 1$). Thus, the reader is explicitly advised against transferring these statements directly to the mixed convection regime without taking great care and without performing additional work.

Before presenting the individual conclusions, the 3 goals of the present thesis are recalled (see Section 1.4):

1. To shed light on the heat transfer in the forced convection limit ($Ri \ll 1$) for large scale cavities ($Re \geq 10^6$).

2. To enhance the understanding of the heat transfer in the mixed convection regime ($Ri \approx 1$) for large scale cavities ($Gr \geq 10^{10}$, $Re \geq 10^6$).

3. To analyze possible convective heat loss reduction measures.

These 3 goals have been addressed in this thesis by (i) wind tunnel measurements of the forced convective heat loss from models of solar central cavity receivers with 3 different cavity inclinations at 1 aperture opening ratio and with 3 different aperture opening ratios at 1 cavity inclination, including the relevant part of the tower; (ii) wind tunnel measurements of the forced convective heat loss from 3 passive reduction measures that were a solid porch, a porous porch, and an aerodynamic optimized porch; (iii) numerical simulations of the wind tunnel models that have been done for a small selection of the wind tunnel measurement points in order to validate the numerical code in the forced convection limit; (iv) numerical simulations of the original scale at $Ri \approx 1$ and $Gr \geq 10^{10}$ that have been done for 3 cavity inclinations at 1 aperture opening ratio.

The first conclusion drawn in this work is that the novel *ringlike wall-mounted hot-film sensors are a suitable means for measuring the forced convective heat flux from complex internal geometries*. This was shown by theoretical considerations (see Section 3.2.1.1), experimental measurements and their associated uncertainty (see Sections 4.1 and 5.1), and the comparison of the measurements to the simulations (see Sections 4.2.1 and 5.4).

Based on the measured data (see Sections 4.1.1, 4.1.2, and 4.1.4), only supportive arguments could be found for Hypothesis 1. Thus, *the forced convective heat loss from a cavity is highly sensitive to the wind speed and the wind direction*. It was found that the forced convective heat loss from a cavity without reduction measures may be increased by (i) the wind speed by a factor of up to 2.7 and (ii) the wind direction by a factor of up to 6.1.

From this high sensitivity to the external, governing flow it is concluded that *future studies should have a wind incident angle increment* $\Delta\alpha \leq 10°$ *in order to capture the relevant phenomena of the forced convective heat loss*.

Also based on the measurements, Hypothesis 2 was formulated. Since the supportive arguments outweigh the contradictory arguments by far, it is concluded that *the location of the peak of the relative forced convective Nusselt number* Nu_{rel} *with respect to the wind incident angle* α *changes with the aperture ratio* X_{ap}*, but not with the inclination angle* γ *or the Reynolds number*.

In Hypotheses 3 and 4, the change in forced convective heat loss from a cavity for a fixed Reynolds number is suggested to follow a function f_1 depending on the absolute incident angle χ and for a fixed absolute incident angle is suggested to follow a function f_2 depending on the Reynolds number. Combining these 2 insights, it is concluded that *the forced convective heat loss from a cavity for* $\alpha \leq 90°$ *can be estimated with* $Nu_{\mathrm{rel}} = f_1(\chi)f_2(Re)$. A concrete empirical function is not given because the underlying data was measured only for $X_{\mathrm{ap}} = 0.8$, but first estimates can be made from the results in Figs. 4.1.4 and 4.1.5.

In Hypothesis 5, it was stated that the tower does not cause a substantial shift in the location of the peak value of the forced convective heat loss with respect to α. *Whether Hypothesis 5 is correct is not determinable with the present data set*. More investigations need to be made, especially with a focus on the influence of the tower on the flow field in front of the cavity.

The comparison to a heated external cylinder (see Section 5.2) leads to the conclusion that *the qualitative behavior of the forced convective heat loss from a cavity with inclination angle* $\gamma = 0°$ *and an external cylinder is similar for similar Reynolds numbers*. Also in Section 5.2, an explanatory framework is introduced that may help to better understand forced convective heat loss from cavities. This framework is depicted graphically in Fig. 5.2.2. As the basis of this framework, *Hypotheses 7 and 8 stress the importance of the characteristics of the external flow in direct vicinity to the aperture*.

The investigation of the 3 reduction measures led to Hypotheses 9 to 11. It is concluded that *for forced convection the solid porch reduces the heat loss mainly at wind incident angles* $\alpha \leq 40°$*, the porous porch reduces the heat loss mainly at* $\alpha = [70°,\ldots,100°]$*, and the aerodynamic porch moderately reduces the heat loss at* $\alpha \leq 40°$ *and increases the heat loss at* $\alpha = [90°,\ldots,150°]$. The heat loss increase for pure forced convection could actually mean that there could be a beneficial, protective aerowindow for mixed convection (see Hypothesis 12 and Section 5.3). But, this has to be investigated in more detail in the future.

From the comparison of the experimental measurements and the numerical simulations it is concluded that *steady-state RANS simulations may give valid results for wind incident angles* $\alpha \leq 90°$. Additionally, Hypothesis 14 is considered true, which means that *in pure forced convection the internal flow in a cavity can be considered as 1 single eddy*.

From the CFD simulations on the original scale (see Hypothesis 15) it is concluded that *the forced convective heat loss contributes substantially to the mixed convective heat loss on the original scale*. Interestingly, the characteristics of the measured forced convective heat loss are not reflected in the characteristics of the simulated mixed convective heat loss. The causes are however not understood, yet. The comparison of the original scale simulations to previous experiments suggests that *in larger cavities the contribution of the*

forced convective heat loss to the mixed convective heat loss is larger than for smaller cavities at the same Richardson number. However, a future study has to be performed to investigate this in more depth.

The conclusion that sets the convective heat loss in relation to the radiative heat loss and the conductive heat loss is based on the discussion in Section 5.6. It is concluded that *the mixed convective heat loss from cavities with inclination angles* $\gamma = [0°, 30°, 60°]$ *is at least of the same order of magnitude as the radiative heat loss; at maximum, it can be up to twice as large as the radiative loss; and the conductive heat loss may be neglected*.

Finally, it is concluded that *the optimization of the design of a multi-megawatt CSTE cavity receiver with respect to convective heat loss is possible when a specific site is given and its meteorological boundary conditions are well known.*

Chapter 7

Outlook

In the conclusions in Chapter 6, a selection of relevant questions that remain unanswered after this thesis are given. They are collected hereafter.

One of the largest questions that rose during this work and that remains unanswered, is how the characteristics of the pure forced convective heat loss shape the characteristics of the mixed convective heat loss. To further investigate this topic a CFD study on the original scale with a series of $Ri \approx [0.01, \ldots, 100]$ is suggested. By doing so, the researcher will be able to deduce at what Richardson number the forced characteristics can be observed clearly and when and how they change.

To characterize the direction independency of the ringlike hot-film sensors a study on a flat plate under known flow conditions should be carried out. By rotating the plate and correlating it to for example a conventional straight hot-film sensor, the direction independency can be measured.

The explanatory framework has to be tested with more data in order to validate it. Different geometries of the cavity should be tested with different tower geometries and different flow conditions. Ideally, after thorough testing one will also be able to add a quantification to this framework.

As pointed out in Chapter 6, the relative forced convective heat loss Nu_{rel} can be estimated by a combination of 2 functions depending on the absolute incident angle χ and the Reynolds number, respectively. To find an empirical formula more measurements with additional geometries are needed.

To understand the influence of the tower on the flow field in front of the cavity and hence the forced convective heat loss more data are needed. Especially of interest are imaging methods, be they numerical or experimental.

In order to give a useful indication, whether the reduction measures also reduce the mixed convective heat loss in a real CSTE system, these reduction measures have to be tested numerically or experimentally in an original scale setup with mixed convection. Of particular interest would be whether the aerodynamic porch really generates a nozzle effect and whether this effect would lead to a passive aerowindow.

Bibliography

Achenbach, E (1977). "The effect of surface roughness on the heat transfer from a circular cylinder to the cross flow of air". In: *International Journal of Heat and Mass Transfer* 20, pp. 359–369. DOI: 10.1016/j.applthermaleng.2015.05.059.

ANSYS, Inc., USA (2018). *ANSYS Meshing*. URL: https://www.ansys.com/products/platform/ansys-meshing (visited on 2018-03-13).

Barlow, J B, W H Rae, and A Pope (1999). *Low-Speed Wind Tunnel Testing*. 3rd ed. New York: Wiley.

Beasley, D E and R S Figliola (1988). "A generalised analysis of a local heat flux probe". In: *Journal of Physics E: Scientific Instruments* 21, pp. 316–322. DOI: 10.1088/0022-3735/21/3/016.

Bellhouse, B J and D L Schultz (1966). "Determination of mean and dynamic skin friction, separation and transition in low-speed flow with a thin-film heated element". In: *Journal of Fluid Mechanics* 24, pp. 379–400. DOI: 10.1017/S0022112066000715.

Bergman, T L, A S Lavine, F P Incropera, and D P DeWitt (2011). *Fundamentals of Heat and Mass Transfer*. 7th ed. Hoboken: Wiley.

Boehm, R F (1987). "A Review of Convective Loss Data From Solar Central Receivers". In: *Journal of Solar Energy Engineering* 109, pp. 101–107. DOI: 10.1115/1.3268185.

Bruun, H H (1995). *Hot-wire Anemometry*. Oxford: Oxford University Press.

Chen, D, Y Liu, R Benito, and W Stein (2006). "CFD Modelling of the Radiation and Convection Losses in the MTSA Receiver". In: *5th International Conference on CFD in the Process Industries*.

Clausing, A M (1979). "Experimental Studies of Forced, Natural and Combined Convective Heat Transfer at Cryogenic Temperatures". In: *1st International Symposium on Cryogenic Wind Tunnels*, pp. 24.1–24.8.

— (1981). "An analysis of convective losses from cavity solar central receivers". In: *Solar Energy* 27, pp. 295–300. DOI: 10.1016/0038-092X(81)90062-1.

— (1983). "Convective Losses From Cavity Solar Receivers—Comparisons Between Analytical Predictions and Experimental Results". In: *Journal of Solar Energy Engineering* 105, pp. 29–33. DOI: 10.1115/1.3266342.

Clausing, A M, L D Lister, and J M Waldvogel (1989). "Combined convection from isothermal cubical cavities with a variety of side-facing apertures". In: *International Journal of Heat and Mass Transfer* 32, pp. 1561–1566. DOI: 10.1016/0017-9310(89)90077-X.

Clausing, A M, J M Waldvogel, and L D Lister (1987). "Natural convection from isothermal cubical cavities with a variety of side-facing apertures". In: *Journal of Heat Transfer* 109, pp. 407–412. DOI: 10.1115/1.3248095.

Comte-Bellot, G (1976). "Hot-wire Anemometry". In: *Annual Review of Fluid Mechanics* 8, pp. 209–231. DOI: 10.1146/annurev.fl.08.010176.001233.

Dantec Dynamics A/S, Denmark (2018). *Hot-wire and Hot-film Probes - Technical Reference*. URL: https://www.dantecdynamics.com/hot-wire-and-hot-film-probes-technical-reference (visited on 2018-06-14).

Duffie, J A and W A Beckman (2013). *Solar Engineering of Thermal Processes*. 4th ed. Hoboken: Wiley. DOI: 10.1002/9781118671603.

Ebert, M, W Arnold, A Avila-Marin, T Denk, J Hertel, A Jensch, W Reinalter, A Schlierbach, and R Uhlig (2015). "Development of insulation for high flux density receivers". In: *SolarPACES 2014*. Vol. 69. Energy Procedia, pp. 369–378. DOI: 10.1016/j.egypro.2015.03.043.

Emeis, S (2013). *Wind Energy Meteorology*. 1st ed. Berlin: Springer. DOI: 10.1007/978-3-642-30523-8.

Emes, M J, M Arjomandi, and G J Nathan (2015). "Effect of heliostat design wind speed on the levelised cost of electricity from concentrating solar thermal power tower plants". In: *Solar Energy* 115, pp. 441–451. DOI: 10.1016/j.solener.2015.02.047.

Eyler, L L (1979). *Predictions of convective losses from a solar cavity receiver*. Report PNL-SA-8070. Pacific Northwest Laboratory.

Falcone, P K (1986). *A Handbook for Solar Central Receiver Design*. Report SAND86-8009. Sandia National Laboratories.

Fang, J B, J J Wei, X W Dong, and Y S Wang (2011). "Thermal performance simulation of a solar cavity receiver under windy conditions". In: *Solar Energy* 85, pp. 126–138. DOI: 10.1016/j.solener.2010.10.013.

Faust, K M, E J Plate, and M Kuczera (1981). "Experimental Investigation of the Convective Losses from the Cavity Receiver of the Project GAST". In: *Convective Losses From Solar Central Receivers. Proceedings of a DOE/SERI/SNLL Workshop*. Ed. by Sandia National Laboratories and P K Falcone. SAND81-8014, pp. 143–163.

Ferziger, J H and M Peric (2002). *Computational Methods for Fluid Dynamics*. 3rd ed. Berlin: Springer.

Flesch, R (2016). "Windeinfluss auf Cavity-Receiver für solare Turmkraftwerke". Doctoral Thesis. RWTH Aachen University. URL: https://publications.rwth-aachen.de/record/659716/files/659716.pdf (visited on 2018-02-12).

Flesch, R, J Grobbel, H Stadler, R Uhlig, and B Hoffschmidt (2016). "Reducing the Convective Losses of Cavity Receivers". In: *SolarPACES 2015*. Ed. by V Rajpaul and C Richter. Vol. 1734. AIP Conference Proceedings, p. 030014. DOI: 10.1063/1.4949066.

Flesch, R, H Stadler, R Uhlig, and B Hoffschmidt (2015). "On the Influence of Wind on Cavity Receivers for Solar Power Towers: An Experimental Analysis". In: *Applied Thermal Engineering* 87, pp. 724–735. DOI: 10.1016/j.applthermaleng.2015.05.059.

Flesch, R, H Stadler, R Uhlig, and R Pitz-Paal (2014). "Numerical analysis of the influence of inclination angle and wind on the heat losses of cavity receivers for solar thermal power towers". In: *Solar Energy* 110, pp. 427–437. DOI: 10.1016/j.solener.2014.09.045.

Fletcher, E A and R L Moen (1977). "Hydrogen and Oxygen from Water". In: *Science* 197, pp. 1050–1056. DOI: 10.1126/science.197.4308.1050.

Franke, J, A Hellsten, H Schlünzen, and B Carissimo (2007). *Best Practice Guideline for the CFD Simulation of Flows in the Urban Environment*. Report COST Action 732.

Gray, D D and A Giorgini (1976). "The validity of the Boussinesq approximation for liquids and gases". In: *International Journal of Heat and Mass Transfer* 19, pp. 545–551. DOI: 10.1016/0017-9310(76)90168-X.

Harris, J A and T G Lenz (1985). "Thermal Performance of Solar Concentrator/Cavity Receiver Systems". In: *Solar Energy* 34, pp. 135–142. DOI: 10.1016/0038-092X(85)90170-7.

Haselbacher, A (2017). "Modeling, Verification, and Validation in Computational Fluid Dynamics". Lecture during the SFERA Summer School 2017. Berlin.

Heisler, G M and D R DeWalle (1988). "Effects of Windbreaks Structure on Wind Flow". In: *Agriculture, Ecosystems and Environment* 22/23, pp. 41–69. DOI: 10.1016/B978-0-444-43019-9.50008-0.

Hess, C F and R H Henze (1984). "Experimental Investigation of Natural Convection Losses From Open Cavities". In: *Journal of Heat Transfer* 106, pp. 333–338. DOI: 10.1115/1.3246677.

Ho, C K (2016). "A review of high-temperature particle receivers for concentrating solar power". In: *Applied Thermal Energy* 109, pp. 958–969. DOI: 10.1016/j.applthermaleng.2016.04.103.

— (2017). "Advances in central receivers for concentrating solar applications". In: *Solar Energy* 152, pp. 38–56. DOI: 10.1016/j.solener.2017.03.048.

Howell, J R, ed. (2018). *A Catalog of Radiation Heat Transfer Configuration Factors*. URL: http://www.thermalradiation.net/tablecon.html (visited on 2018-03-10).

Howell, J R, R Siegel, and M Pinar Mengüc (2011). *Thermal Radiation Heat Transfer*. 5th ed. Boca Raton: CRC Press.

Hughes, G, J Pye, M Kaufer, E Abbasi-Shavazi, J Zhang, A McIntosh, and T Lindley (2016). "Reduction of Convective Losses in Solar Cavity Receivers". In: *SolarPACES 2015*. Ed. by V Rajpaul and C Richter. Vol. 1734. AIP Conference Proceedings, p. 030023. DOI: 10.1063/1.4949075.

Humphrey, J A C, L Miller, and K-S Chen (1981). "Experimental Investigation of Thermally Driven Flow in Open Cavities of Rectangular Cross-Section". In: *Convective Losses From Solar Central Receivers. Proceedings of a DOE/SERI/SNLL Workshop*. Ed. by Sandia National Laboratories and P K Falcone. SAND81-8014, pp. 71–92.

Humphrey, J A C, F S Sherman, P Le Quéré, K-S Chen, L Miller, and W-M To (1982). *Investigation of Free-Forced Convection Flows in Cavity-Type Receivers*. Report SAND79-8196. Sandia National Laboratories.

Intergovernmental Panel on Climate Change (2013). *Summary for Policymakers*. In: *Climate Change 2013 – The Physical Science Basis. Working Group I Contribution to the Fifth Assessment Report of the Intergovernmental Panel on Climate Change*. Ed. by T F Stocker, D Qin, G-K Plattner, M Tignor, S K Allen, J Boschung, A Nauels, Y Xia, V Bex, and P M Midgley. URL: https://www.ipcc.ch/report/ar5/wg1 (visited on 2018-02-12).

IRENA (2012). *Renewable Energy Technologies: Cost Analysis Series. Concentrating Solar Power*. Report. URL: http://irena.org/publications/2012/Jun/Renewable-Energy-Cost-Analysis---Concentrating-Solar-Power.

ISO (2008). *Guide to the expression of uncertainty in measurement (GUM:1995)*. International Organization for Standardization.

Kaimal, J C and J J Finnigan (1994). *Atmospheric Boundary Layer Flows*. 1st ed. Oxford: Oxford University Press.

Kakaç, S, Y Yener, and A Pramuanjaroenkij (2014). *Convective Heat Transfer*. 3rd ed. Boca Raton: CRC Press.

Kalitzin, G, G Medic, G Iaccarino, and P Durbin (2005). "Near-wall behavior of RANS turbulence models and implications for wall functions". In: *Journal of Computational Physics* 204, pp. 265–291. DOI: 10.1016/j.jcp.2004.10.018.

Kim, J K, J S Kim, and W Stein (2015). "Simplified heat loss model for central tower solar receiver". In: *Solar Energy* 116, pp. 314–322. DOI: 10.1016/j.solener.2015.02.022.

Kim, J K, H K Yoon, and Y H Kang (2007). "Experimental Study on Heat Loss from Cavity Receiver for Solar Power Tower". In: *Proceedings of International Solar Energy Society Solar World Congress 2007*, pp. 1719–1723.

Kim, J S, P Liovic, Y C S Too, G Hart, and W Stein (2012). "CFD Analysis of Heat Loss from 200kW Cavity Reactor". In: *SolarPACES 2012*.

Kline, S J (1986). *Similitude and Approximation Theory*. 1st ed. Berling: Springer.

Kraabel, J S (1983). "An experimental investigation of the natural convection from a side-facing cubical cavity". In: *ASME-JSME Thermal Engineering Joint Conference Proceedings*. Vol. 1, pp. 299–306.

Le Quéré, P, F Penot, and M Mirenayat (1981). "Experimental Study of Heat Loss through Natural Convection from an Isothermal Cubic Open Cavity". In: *Convective Losses From Solar Central Receivers. Proceedings of a DOE/SERI/SNLL Workshop*. Ed. by Sandia National Laboratories and P K Falcone. SAND81-8014, pp. 165–174.

Leibfried, U and J Ortjohann (1995). "Convective Heat Loss from Upward and Downward-Facing Cavity Solar Receivers: Measurements and Calculations". In: *Journal of Solar Energy Engineering* 117, pp. 75–84. DOI: 10.1115/1.2870873.

Liovic, P, J S Kim, G Hart, and W Stein (2014). "Wind dependence of energy losses from a solar gas reformer". In: *Applied Thermal Engineering* 63, pp. 333–346. DOI: 10.1016/j.applthermaleng.2013.11.002.

Liu, B, J Qu, W Zhang, L Tan, and Y Gao (2014). "Numerical evaluation of the scale problem on the wind flow of a windbreak". In: *Scientific Reports* 4, p. 6619. DOI: 10.1038/srep06619.

Lomas, C G (1986). *Fundamentals of Hot Wire Anemometry*. 1st ed. Cambridge: Cambridge University Press.

Lovegrove, K and W Stein, eds. (2012). *Concentrating Solar Power Technology*. 1st ed. Cambridge: Woodhead Publishing.

Ma, R Y (1993). *Wind Effects on Convective Heat Loss From a Cavity Receiver for a Parabolic Concentrating Solar Collector*. Report SAND92-7293. Sandia National Laboratories. DOI: 10.2172/10192244.

Martin, H (2014). "Nusselt's Fundamental Law of Heat Transfer - Revisited". In: *Heat Transfer Engineering* 35, pp. 246–250. DOI: 10.1080/01457632.2013.825163.

McCroskey, W J and E J Durbin (1972). "Flow Angle and Shear Stress Measurements Using Heated Films and Wires". In: *Journal of Basic Engineering* 94, pp. 46–52. DOI: 10.1115/1.3425384.

McDonald, C G (1995). *Heat Loss from an Open Cavity*. Report SAND95-2939. Sandia National Laboratories.

McMordie, R K (1981). "Convection Losses from a Cavity Receiver". Presented at the 20th National ASME-AIChE Heat Transfer Conference.

— (1984). "Convection Heat Loss from a Cavity Receiver". In: *Journal of Solar Energy Engineering* 106, pp. 98–100. DOI: 10.1115/1.3267569.

McNaughton, K G (1988). "Effects of Windbreaks on Turbulent Transport and Microclimate". In: *Agriculture, Ecosystems and Environment* 22/23, pp. 17–39. DOI: 10.1016/B978-0-444-43019-9.50007-9.

Menter, F R (1994). "Two-Equation Eddy-Viscosity Turbulence Models for Engineering Applications". In: *AIAA Journal* 32, pp. 1598–1605. DOI: 10.2514/3.12149.

Menter, F R, M Kuntz, and R Langtry (2003). "Ten Years of Industrial Experience with the SST Turbulence Model". In: *Turbulence, Heat and Mass Transfer 4*, pp. 625–632.

Mirenayat, H (1981). "Etude éxperimentale du transfer de chaleur par convection naturelle dans une cavité isotherme ouverte". Doctoral Thesis. University of Poitiers.

O'Donovan, T S, T Persoons, and D B Murray (2011). "High-resolution hot-film measurement of surface heat flux to an impinging jet". In: *Measurement Science and Technology* 22, p. 105402. DOI: 10.1088/0957-0233/22/10/105402.

OpenFOAM Foundation (2018a). *OpenFOAM User Guide*. URL: https://cfd.direct/openfoam/user-guide-v4 (visited on 2018-03-13).

— (2018b). *OpenFOAM C++ Source Code Guide*. URL: https://cpp.openfoam.org/v4 (visited on 2018-03-13).

Paitoonsurikarn, S and K Lovegrove (2002). "Numerical Investigation of Natural Convection Loss in Cavity-Type Solar Receivers". In: *Proceedings of Solar 2002*.

Paitoonsurikarn, S, K Lovegrove, G Hughes, and J Pye (2011). "Numerical Investigation of Natural Convection Loss From Cavity Receivers in Solar Dish Applications". In: *Journal of Solar Energy Engineering* 133, p. 021004. DOI: 10.1115/1.4003582.

Paitoonsurikarn, S, T Taumoefolau, and K Lovegrove (2004). "Estimation of Convection Loss from Paraboloidal Dish Cavity Receivers". In: *Proceedings of the 42nd Conference of the Australia and New Zealand Solar Energy Society (ANZSES)*.

Pavlovic, M D and F Penot (1991). "Experiments in the Mixed Convection Regime in an Isothermal Open Cubic Cavity". In: *Experimental Thermal and Fluid Science* 4, pp. 648–655. DOI: 10.1016/0894-1777(91)90072-Y.

Prakash, M, S B Kedare, and J K Nayak (2009). "Investigations on heat losses from a solar cavity receiver". In: *Solar Energy* 83, pp. 157–170. DOI: 10.1016/j.solener.2008.07.011.

Rajpaul, V and C Richter, eds. (2016). *SolarPACES 2015*. Vol. 1734. AIP Conference Proceedings.

Reddy, K S, G Vershetty, and T Srihari Vikram (2016). "Effect of wind speed and direction on convective heat losses from solar parabolic dish modified cavity receiver". In: *Solar Energy* 131, pp. 183–198. DOI: 10.1016/j.solener.2016.02.039.

Robertson, E, V Choudhoury, S Bhushan, and D K Walters (2015). "Validation of OpenFOAM numerical methods and turbulence models for incompressible bluff body flows". In: *Computers and Fluids* 123, pp. 122–145. DOI: 10.1016/j.compfluid.2015.09.010.

Sandia National Laboratories and P K Falcone, eds. (1981). *Convective Losses From Solar Central Receivers. Proceedings of a DOE/SERI/SNLL Workshop*. SAND81-8014.

SAURAN (2017). *Southern African Universities Radiometric Network*. URL: http://sauran.net (visited on 2017-07-15).

Scheffler, M and P Colombo, eds. (2005). *Cellular Ceramics: Structure, Manufacturing, Properties and Applications*. Weinheim: Wiley-VCH.

Schewe, G (1983). "On the force fluctuations acting on a circular cylinder in crossflow from subcritical up to transcritical Reynolds numbers". In: *Journal of Fluid Mechanics* 133, pp. 265–285. DOI: 10.1017/S0022112083001913.

Schlichting, H and K Gersten (1997). *Grenzschicht-Theorie*. 9th ed. Berlin: Springer.

Schüler, D et al. (2016). "The enerMENA meteorological network – Solar radiation measurements in the MENA region". In: *SolarPACES 2015*. Ed. by V Rajpaul and C Richter. Vol. 1734. AIP Conference Proceedings, p. 150008. DOI: 10.1063/1.4949240.

Schwarzbözl, P, Mark Schmitz, and R Pitz-Paal (2009). "Visual HFLCAL - A Software Tool for Layout and Optimisation of Heliostat Fields". In: *SolarPACES 2009*. URL: http://elib.dlr.de/60308.

Siebers, D L and J S Kraabel (1984). *Estimating Convective Energy Losses from Solar Central Receivers*. Report SAND84-8717. Sandia National Laboratories.

Siegrist, S (2016). "Sensor für einen Heissfilmanemometer sowie Heissfilmanemometer". German pat. req. DE 10 2016 221 629 A1. DLR e. V. (filed on 2016-11-04).

Siegrist, S, H Stadler, and B Hoffschmidt (2017). "Novel Wall-mounted Hot-film Sensors for the Measurement of the Forced Convection from an Open Cylindrical Cavity". Paper

presented at the 9th World Conference on Experimental Heat Transfer, Fluid Mechanics and Thermodynamics (Ex-HFT9). URL: http://elib.dlr.de/112812.

Siegrist, S, H Stadler, and B Hoffschmidt (2018a). "Measurements of the Forced Convective Heat Loss from Open Cylindrical Cavities of Multi-MW Scale Solar Central Receiver Systems". In: *SolarPACES 2017*. Ed. by A Rebolledo and C Richter. AIP Conference Proceedings. DOI: 10.1063/1.5067072.

— (2018b). "Wind tunnel measurements of forced convective heat loss from multi-megawatt cavities of solar central receiver systems". In: *Solar Energy* 169, pp. 607–615. DOI: 10.1016/j.solener.2018.04.029.

SolarPACES (2017). *CSP Projects Around the World*. URL: http://www.solarpaces.org/csp-technologies/csp-projects-around-the-world (visited on 2017-12-26).

Stadler, H, A Bauknecht, S Siegrist, R Flesch, C C Wolf, N van Hinsberg, and M Jacobs (2017). "Background-oriented schlieren imaging of flow around a circular cylinder at low Mach numbers". In: *Experiments in Fluids* 58.9, p. 114. DOI: 10.1007/s00348-017-2398-7.

Stadler, H and S Siegrist (2018). "Analysing the wind flow around solar cavity receivers by means of background oriented schlieren imaging". Paper presented at the 18th International Symposium on Flow Visualization (ISFV 18).

Stieglitz, R and V Heinzel (2012). *Thermische Solarenergie*. 1st ed. Berlin: Springer. DOI: 10.1007/978-3-642-29475-4.

Stine, W B and C G McDonald (1989). "Cavity Receiver Convective Heat Loss". In: *Proceedings of International Solar Energy Society Solar World Congress 1989*.

Stolten, D and V Scherer, eds. (2013). *Transition to Renewable Energy Systems*. 1st ed. Weinheim: Wiley-VCH. DOI: 10.1002/9783527673872.

Tan, T, Y Chen, Z Chen, N Siegel, and G Kolb (2009). "Wind effect on the performance of solid particle solar receivers with and without the protection of an aerowindow". In: *Solar Energy* 83, pp. 1815–1827. DOI: 10.1016/j.solener.2009.06.014.

Tao of Systems Integration, Inc., USA (2016). *Private communication with the manufacturer of the sensors*.

Taumoefolau, T, S Paitoonsurikarn, G Hughes, and K Lovegrove (2004). "Experimental Investigation of Natural Convection Heat Loss From a Model Solar Concentrator Cavity Receiver". In: *Journal of Solar Energy Engineering* 126, pp. 801–807. DOI: 10.1115/1.1687403.

Tracey, T R, F A Blake, C Royere, and C T Brown (1977). "One MWth solar cavity steam generator solar test program". In: *International Solar Energy Society, Annual Meeting*. Ed. by C Beach and E Fordyce.

Tropea, C, A Yarin, and J F Foss, eds. (2007). *Springer Handbook of Experimental Fluid Mechanics*. 1st ed. Berlin: Springer.

Uhlig, R, R Flesch, B Gobereit, S Giuliano, and P Liedke (2014). "Strategies enhancing efficiency of cavity receivers". In: *SolarPACES 2013*. Vol. 49. Energy Procedia, pp. 538–550. DOI: 10.1016/j.egypro.2014.03.058.

van Hinsberg, N, G Schewe, and M Jacobs (2017). "Experimental investigation on the combined effects of surface roughness and corner radius for square cylinders at high Reynolds numbers up to 10^7". In: *Journal of Wind Engineering & Industrial Aerodynamics* 173, pp. 14–27. DOI: 10.1016/j.jweia.2017.12.003.

VDI (2010). *VDI Heat Atlas*. 2nd ed. Berlin: Springer.

Versteeg, H K and W Malalasekera (2007). *An Introduction to Computational Fluid Dynamics. The Finitve Volume Method*. 2nd ed. Harlow: Pearson.

Villafán-Vidales, H I, C A Arancibia-Bulnes, D Riveros-Rosas, H Romero-Paredes, and C A Estrada (2017). "An overview of the solar thermochemical processes for hydrogen and syngas production: Reactors, and facilities". In: *Renewable and Sustainable Energy Reviews* 75, pp. 894–908. DOI: 10.1016/j.rser.2016.11.070.

von Böckh, P and T Wetzel, eds. (2017). *Wärmeübertragung*. 7th ed. Berlin: Springer. DOI: 10.1007/978-3-662-55480-7.

Wilson, J D (1987). "On the Choice of a Windbreak Porosity Profile". In: *Boundary-Layer Meteorology* 38, pp. 37–49. DOI: 10.1007/BF00121553.

Winter, C-J, R L Sizmann, and L L Vant-Hull, eds. (1991). *Solar Power Plants*. 1st ed. Berlin: Springer. DOI: 10.1007/978-3-642-61245-9.

Wu, S-Y, F-H Guo, and L Xiao (2014). "Numerical investigation on combined natural convection and radiation heat losses in one side open cylindrical cavity with constant heat flux". In: *International Journal of Heat and Mass Transfer* 71, pp. 573–584. DOI: 10.1016/j.ijheatmasstransfer.2013.12.064.

Wu, S-Y, L Xiao, Y Cao, and Y-R Li (2010). "Convection heat loss from cavity receiver in parabolic dish solar thermal power system: A review". In: *Solar Energy* 84, pp. 1342–1355. DOI: 10.1016/j.solener.2010.04.008.

Wu, W, L Amsbeck, Reiner Buck, N Waibel, P Langner, and R Pitz-Paal (2014). "On the influence of rotation on thermal convection in a rotating cavity for solar receiver applications". In: *Applied Thermal Engineering* 70, pp. 694–704. DOI: 10.1016/j.applthermaleng.2014.03.059.

Wu, Y C and L C Wen (1978). *Solar Thermal Power Systems Advanced Solar Thermal Technology Project: Solar receiver performance in the temperature range of 300 to 1300 degree Celsius*. Report JPL-5102-82. Jet Propulsion Lab. URL: https://www.osti.gov/biblio/6953298.

Xiao, L, S-Y Wu, and Y-R Li (2012). "Numerical study on combined free-forced convection heat loss of solar cavity receiver under wind environments". In: *International Journal of Thermal Sciences* 60, pp. 182–194. DOI: 10.1016/j.ijthermalsci.2012.05.008.

Yuan, J K, C K Ho, and J M Christian (2015). "Numerical Simulation of Natural Convection in Solar Cavity Receivers". In: *Journal of Solar Energy Engineering* 137, p. 031004. DOI: 10.1115/1.4029106.

Zdravkovich, M M (1997). *Flow Around Circular Cylinders. Volume I: Fundamentals*. 1st ed. Oxford: Oxford University Press.

Appendices

A Drawings of the Wind Tunnel Models

A drawing of the wind tunnel model with $\gamma = 30°$ and $X_{ap} = 0.8$ is shown in Fig. A.1. In this drawing, one can see the modular setup with the hollow tower part, the head part with the seat for the cavity inlay, and the cavity inlay which is held in place by the aperture. At the very bottom, one can also see the structure which prevents the boundary layer from influencing the tower.

In the following figures, drawings are shown for the different heads and 2 of the reduction measures.

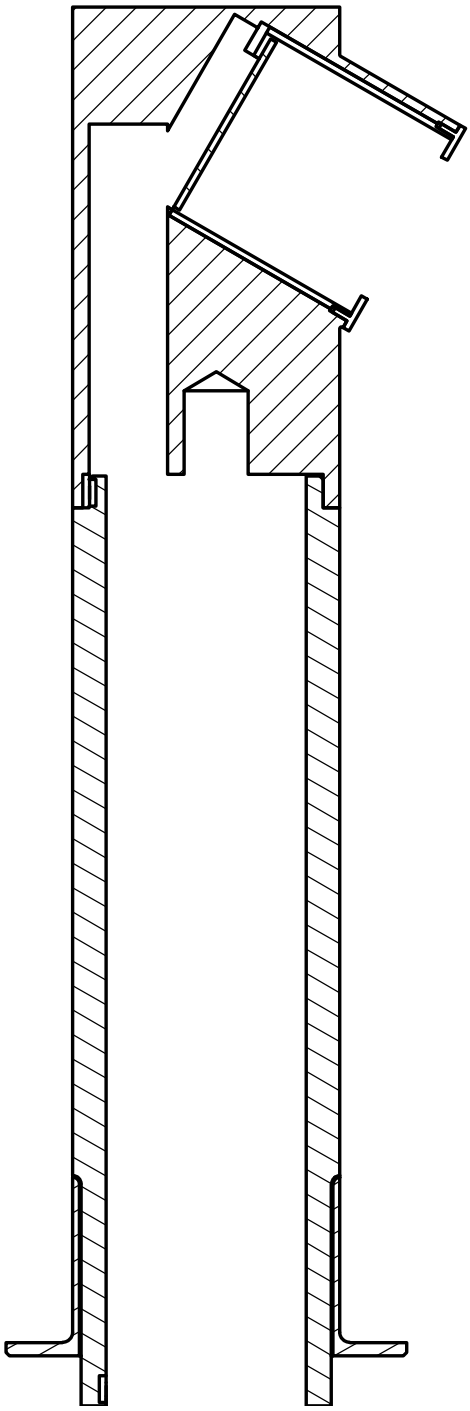

Figure A.1: Drawing of the wind tunnel model with $\gamma = 30°$ and $X_{ap} = 0.8$.

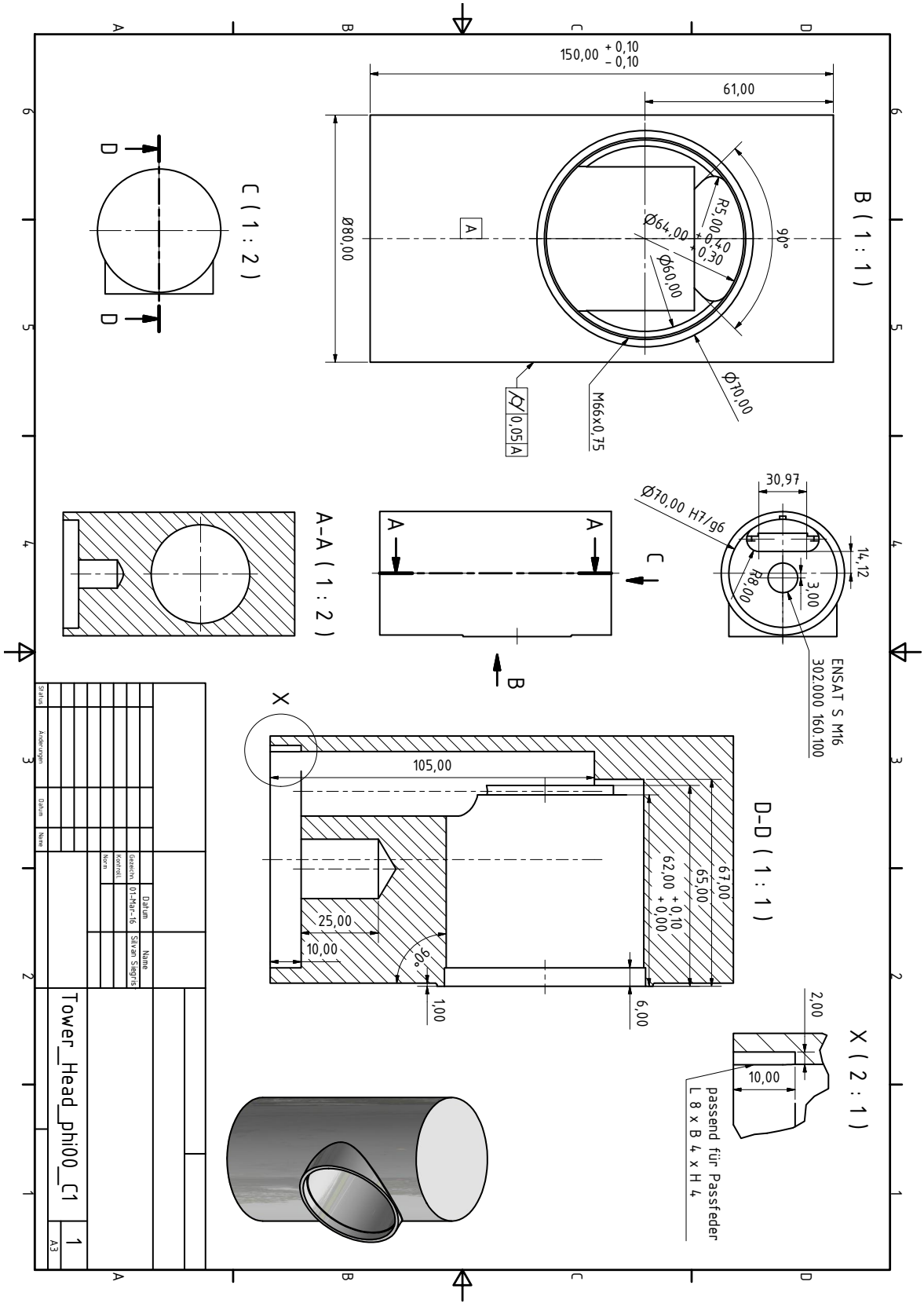

Figure A.2: Drawing of the head of the wind tunnel model with $\gamma = 0°$.

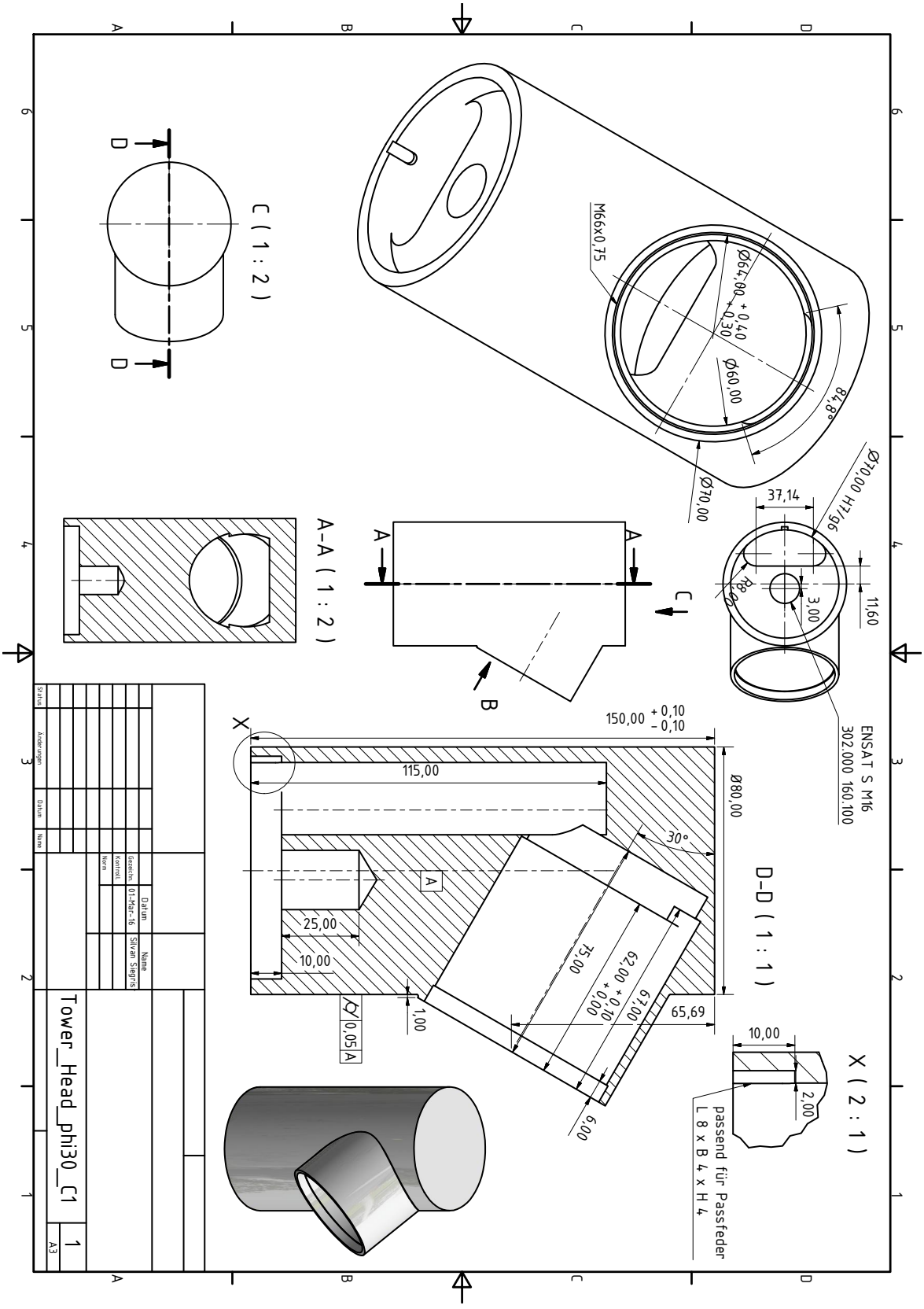

Figure A.3: Drawing of the head of the wind tunnel model with $\gamma = 30°$.

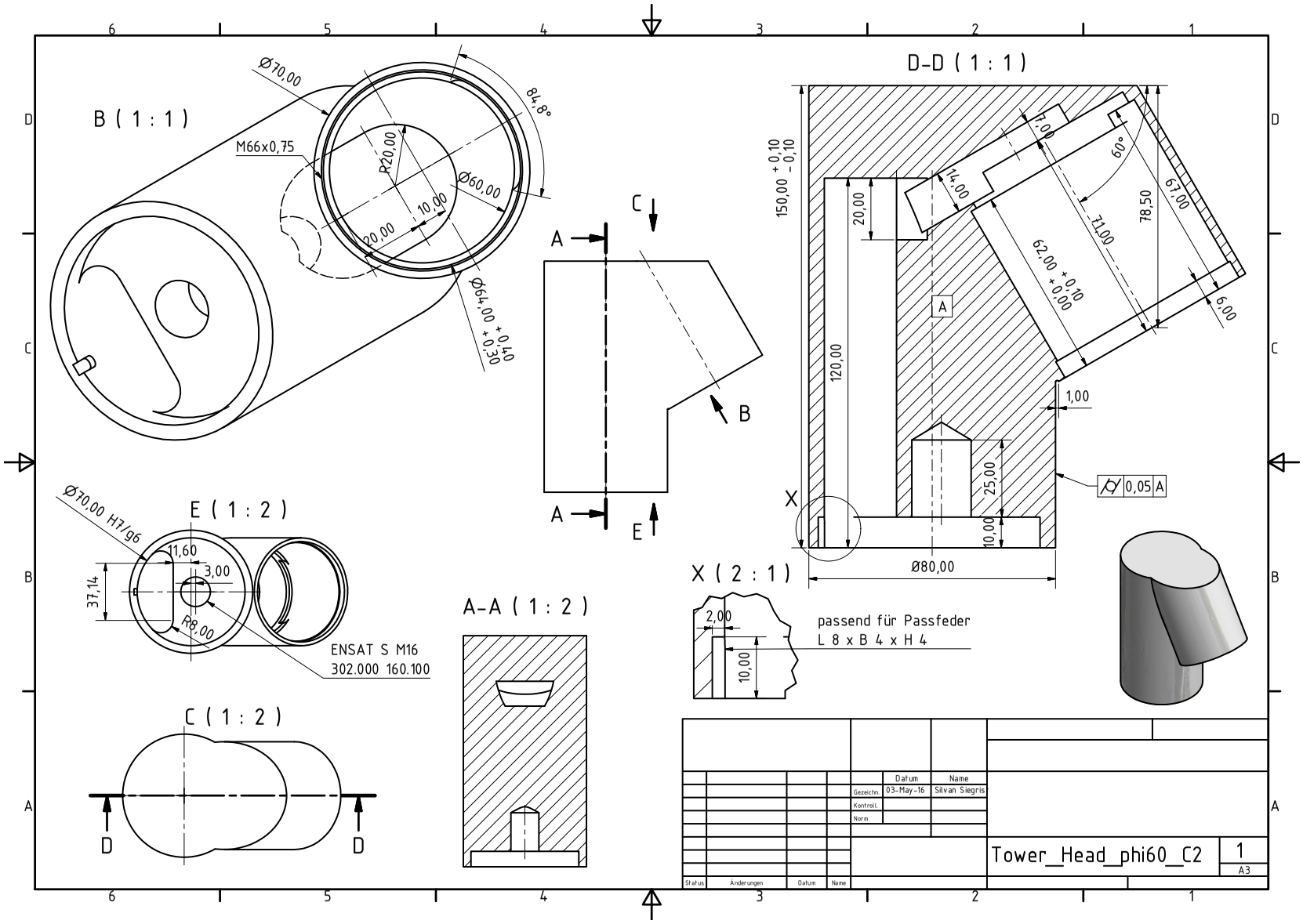

Figure A.4: Drawing of the head of the wind tunnel model with $\gamma = 60°$.

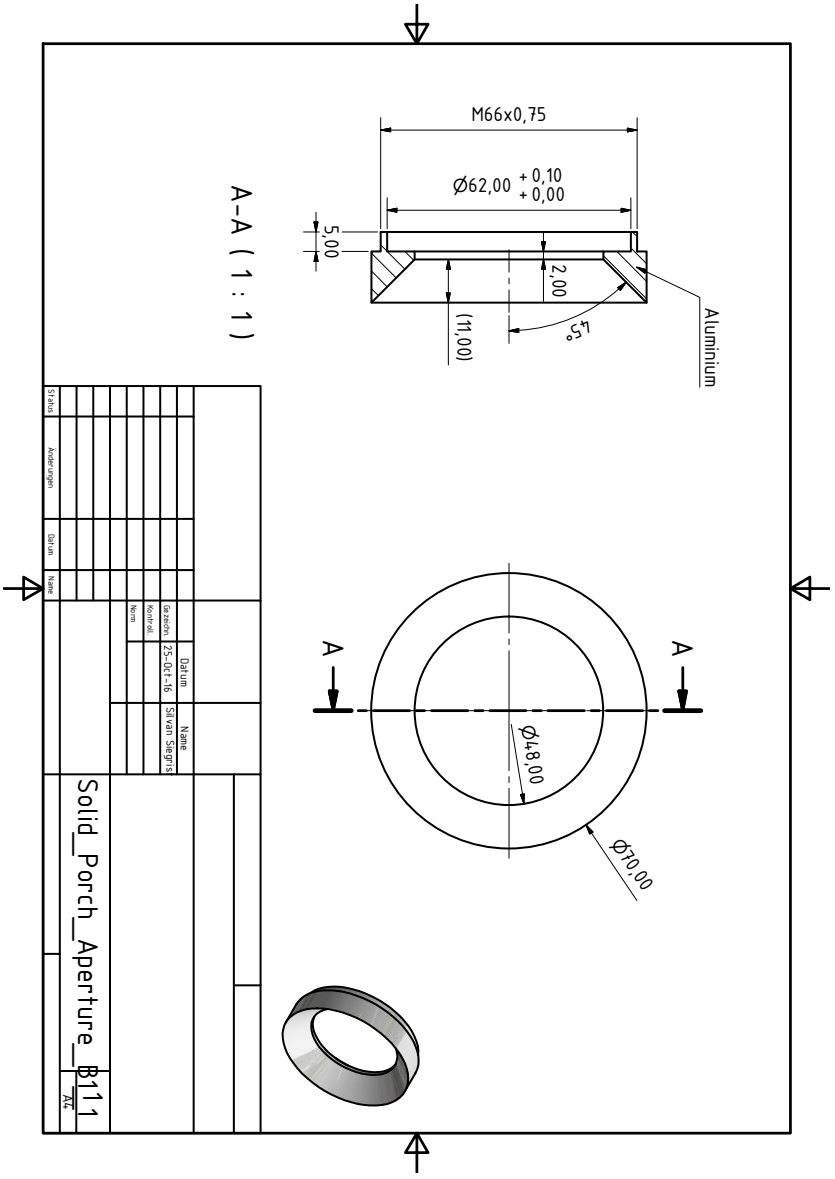

Figure A.5: Drawing of the solid porch.

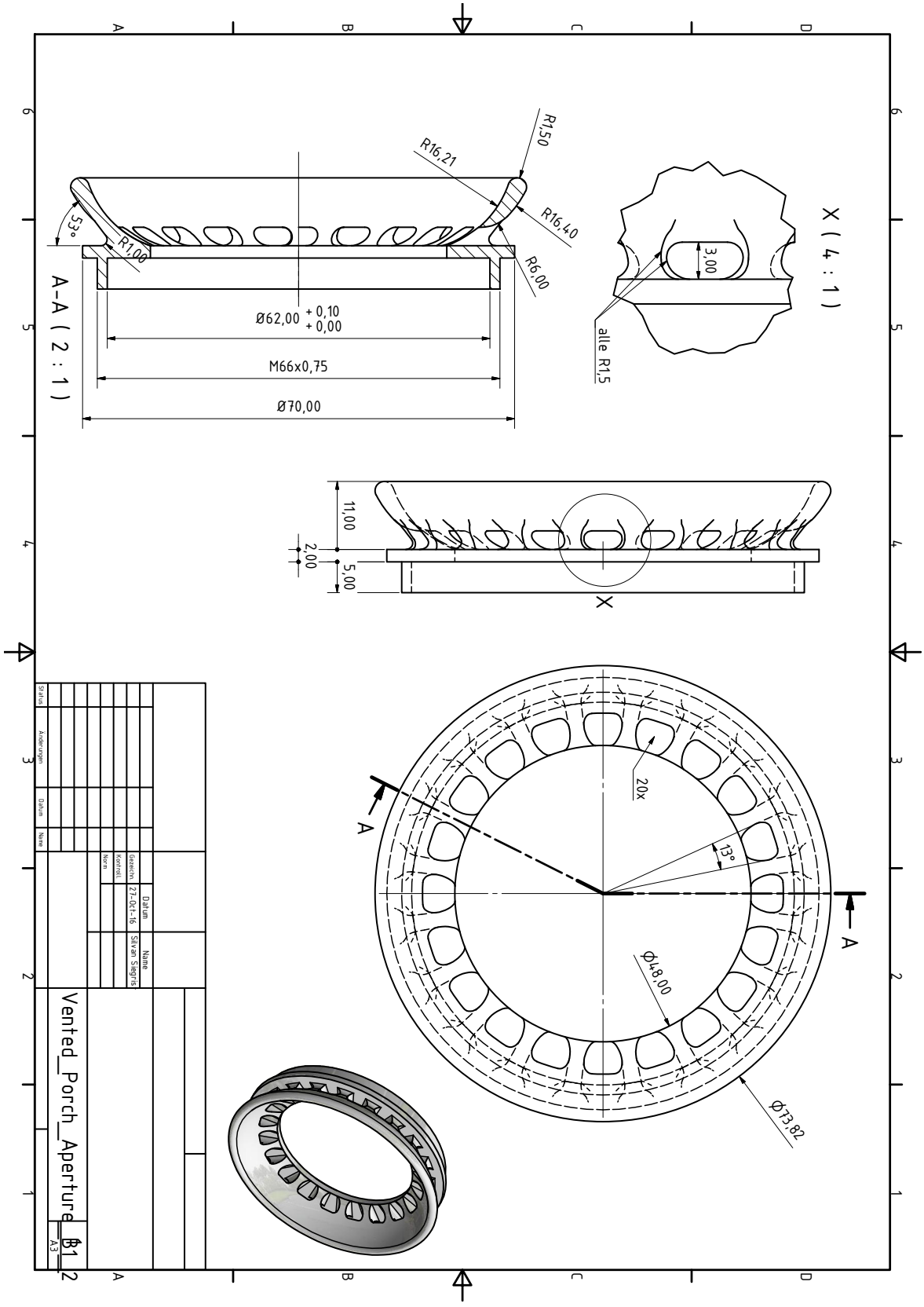

Figure A.6: Drawing of the aerodynamic porch.

B SST k-ω Turbulence Model

The fundamental equations for the SST k-ω model were introduced in Eqs. 2.7.10 and 2.7.11. Here, the implementation in OpenFOAM according to Menter et al. (2003) is shown. The transport equation for the turbulence kinetic energy k in Einstein notation is

$$\frac{\partial}{\partial t}(\rho k) + \frac{\partial}{\partial x_j}\left(\rho u_j k\right) = \min\left(P_k, c_1 \beta^\star \rho k \omega\right) - \beta^\star \rho k \omega + \frac{\partial}{\partial x_j}\left((\mu + \sigma_k \mu_\mathrm{t}) \frac{\partial}{\partial x_j} k\right) \tag{B.1}$$

and the transport equation for the specific turbulence kinetic energy dissipation ω in Einstein notation is

$$\begin{aligned}\frac{\partial}{\partial t}(\rho \omega) + \frac{\partial}{\partial x_j}\left(\rho u_j \omega\right) = &\frac{\gamma \rho}{\mu_\mathrm{t}} \min\left(P_k, c_1 \beta^\star \rho k \omega\right) - \beta \rho \omega^2 \\ &+ \frac{\partial}{\partial x_j}\left((\mu + \sigma_\omega \mu_\mathrm{t}) \frac{\partial}{\partial x_j} \omega\right) \\ &+ 2(1 - F_1) \frac{\rho \sigma_{\omega,2}}{\omega} \frac{\partial}{\partial x_j} k \frac{\partial}{\partial x_j} \omega\end{aligned} \tag{B.2}$$

where P_k is calculated according to the following formulas

$$P_k = \tau_{ij} \frac{\partial}{\partial x_j} u_i \tag{B.3}$$

$$\tau_{ij} = 2\mu_\mathrm{t}\left(s_{ij} - \frac{1}{3}\frac{\partial}{\partial x_l} u_l \delta_{ij}\right) - \frac{2}{3}\rho k \delta_{ij} \tag{B.4}$$

$$s_{ij} = \frac{1}{2}\left(\frac{\partial}{\partial x_j} u_i + \frac{\partial}{\partial x_i} u_j\right) \tag{B.5}$$

and F_1 is a blending function defined by

$$F_1 = \tanh\left(\left(\min\left(\max\left(\frac{k^{1/2}}{\beta^\star \omega y}, \frac{500\mu}{y^2 \rho \omega}\right), \frac{4\rho\sigma_{\omega,2} k}{D_{k\omega} y^2}\right)\right)^4\right) \tag{B.6}$$

where y is the distance normal to the wall and

$$D_{k\omega} = \max\left(\frac{2\rho\sigma_{\omega,2}}{\omega} \frac{\partial}{\partial x_j} k \frac{\partial}{\partial x_j} \omega, 10^{-10}\right) \tag{B.7}$$

The eddy viscosity is calculated as

$$\mu_\mathrm{t} = \frac{a_1 \rho k}{\max(a_1 \omega, S F_2)} \tag{B.8}$$

where S is the invariant of the strain rate and F_2 is another blending function defined as

$$F_2 = \tanh\left(\left(\max\left(\frac{2k^{1/2}}{\beta^\star \omega y}, \frac{500\mu}{y^2 \rho \omega}\right)\right)^2\right) \tag{B.9}$$

Table B.1: Standard constants used in the implementation of the SST k-ω turbulence model in OpenFOAM.

Constant	$\sigma_{k,1}$	$\sigma_{k,2}$	$\sigma_{\omega,1}$	$\sigma_{\omega,2}$	γ_1	γ_2	β_1	β_2	$\beta^\star$	a_1	b_1	c_1
Value	0.85	1	0.5	0.856	5/9	0.44	0.075	0.0828	0.09	0.31	1	10

The constants used in this model are given in Table B.1. The blend of the constants σ_ω, σ_k, γ and β of their inner (marked by 1) and outer (marked by 2) values is done via the following relationship

$$\begin{pmatrix} \sigma_\omega \\ \sigma_k \\ \gamma \\ \beta \end{pmatrix} = F_1 \begin{pmatrix} \sigma_{\omega,1} \\ \sigma_{k,1} \\ \gamma_1 \\ \beta_1 \end{pmatrix} + (1 - F_1) \begin{pmatrix} \sigma_{\omega,2} \\ \sigma_{k,2} \\ \gamma_2 \\ \beta_2 \end{pmatrix} \tag{B.10}$$

And finally, a turbulence Prandtl number is used to link the turbulent thermal diffusivity and the turbulent momentum diffusivity.

$$Pr_\mathrm{t} = \frac{\mu_\mathrm{t}}{\alpha_\mathrm{t}\rho} = 0.85 \tag{B.11}$$

C Boundary Conditions in OpenFOAM

Tables C.1 and C.2 give the precise names of the boundary conditions in OpenFOAM used in this work. For explanations please see Section 3.3.3.

Table C.1: Overview of the applied boundary conditions in the wind tunnel simulations with their corresponding names in OpenFOAM.

Wind tunnel	**U**	p	T	k	ω	ν_t	α_t
Inlet	fixed-Value	fixedFlux-Pressure	fixed-Value	turbulentIntensityKinet-icEnergyInlet	turbulentMixingLengthFre-quencyInlet	calculated	calculated
Outlet	zeroGra-dient	fixedValue	in-letOut-let	zeroGradient	zeroGradient	calculated	calculated
Cavity inside	noSlip	fixedFlux-Pressure	fixed-Value	kqRWallFunction	omegaWallFunction	nutkWall-Function	compressible::-alphatWallFunction
Tower	noSlip	fixedFlux-Pressure	fixed-Value	kqRWallFunction	omegaWallFunction	nutkWall-Function	compressible::-alphatWallFunction
Top	noSlip	fixedFlux-Pressure	fixed-Value	kqRWallFunction	omegaWallFunction	nutkWall-Function	compressible::-alphatWallFunction
Bottom	noSlip	fixedFlux-Pressure	fixed-Value	kqRWallFunction	omegaWallFunction	nutkWall-Function	compressible::-alphatWallFunction
Sides	noSlip	fixedFlux-Pressure	fixed-Value	kqRWallFunction	omegaWallFunction	nutkWall-Function	compressible::-alphatWallFunction

Table C.2: Overview of the applied boundary conditions in the original scale simulations with their corresponding names in OpenFOAM.

Original scale	**U**	p	T	k	ω	ν_t	α_t
Inlet	fixedValue	fixedFluxPressure	fixedValue	fixedValue	fixedValue	calculated	calculated
Outlet	pressureInletOutletVelocity	sfBuoyantTotalPressure	inletOutlet	inletOutlet	inletOutlet	calculated	calculated
Cavity inside	noSlip	fixedFluxPressure	uniformFixedValue	kqRWallFunction	omegaWallFunction	nutkWallFunction	compressible::alphatWallFunction
Tower	noSlip	fixedFluxPressure	zeroGradient	kqRWallFunction	omegaWallFunction	nutkWallFunction	compressible::alphatWallFunction
Top	slip	fixedFluxPressure	zeroGradient	zeroGradient	zeroGradient	calculated	calculated
Bottom	slip	fixedFluxPressure	zeroGradient	zeroGradient	zeroGradient	calculated	calculated
Sides	pressureInletOutletVelocity	sfBuoyantTotalPressure	inletOutlet	inletOutlet	inletOutlet	calculated	calculated

D Numerical Schemes in OpenFOAM

The below code was used to specify the discretization schemes for the CFD simulations in OpenFOAM. More information on the CFD simulations can be found in Section 3.3.
Wind tunnel simulations:

```
/*--------------------------------*- C++ -*----------------------------------*\
| =========                 |                                                 |
| \\      /  F ield         | OpenFOAM: The Open Source CFD Toolbox           |
|  \\    /   O peration     | Version:  4.x                                   |
|   \\  /    A nd           | Web:      www.OpenFOAM.org                      |
|    \\/     M anipulation  |                                                 |
\*---------------------------------------------------------------------------*/
FoamFile
{
    version     2.0;
    format      ascii;
    class       dictionary;
    location    "system";
    object      fvSchemes;
}
// * * * * * * * * * * * * * * * * * * * * * * * * * * * * * * * * * * * * * //

ddtSchemes
{
    default         steadyState;
}

gradSchemes
{
    default         cellLimited Gauss linear 1;
}

divSchemes
{
    default         none;
    div(phi,U)      bounded Gauss linearUpwindV grad(U);
    div(phi,K)      bounded Gauss linearUpwind grad(K);
    div(phi,h)      bounded Gauss linearUpwind grad(h);
    div(phi,k)      bounded Gauss upwind;
    div(phi,omega)  bounded Gauss upwind;
    div(((rho*nuEff)*dev2(T(grad(U))))) Gauss linear;
}

laplacianSchemes
{
    default         Gauss linear corrected;
}

interpolationSchemes
{
    default         linear;
}

snGradSchemes
{
    default         corrected;
}

wallDist
{
    method              meshWave;
}


// ************************************************************************* //
```

Original scale simulations:

```
/*--------------------------------*- C++ -*----------------------------------*\
| =========                 |                                                 |
| \\      /  F ield         | OpenFOAM: The Open Source CFD Toolbox           |
|  \\    /   O peration     | Version:  4.x                                   |
|   \\  /    A nd           | Web:      www.OpenFOAM.org                      |
|    \\/     M anipulation  |                                                 |
\*---------------------------------------------------------------------------*/
FoamFile
{
    version     2.0;
    format      ascii;
    class       dictionary;
    location    "system";
    object      fvSchemes;
}
// * * * * * * * * * * * * * * * * * * * * * * * * * * * * * * * * * * * * * //

ddtSchemes
{
    default         steadyState;
}

gradSchemes
{
    default         cellLimited Gauss linear 1;
}

divSchemes
{
    default         none;
    div(phi,U)      bounded Gauss vanLeerV;
    div(phi,K)      bounded Gauss vanLeer;
    div(phi,h)      bounded Gauss vanLeer;
    div(phi,k)      bounded Gauss upwind;
    div(phi,omega)  bounded Gauss upwind;
    div(((rho*nuEff)*dev2(T(grad(U))))) Gauss linear;
}

laplacianSchemes
{
    default         Gauss linear limited corrected 0.5;
}

interpolationSchemes
{
    default         linear;
}

snGradSchemes
{
    default         limited corrected 0.5;
}

wallDist
{
    method              meshWave;
}


// ************************************************************************* //
```

E Estimations of the Heat Dissipated in a Hot-Film Sensor

In the following sections, the heat dissipated from 1 sensor is calculated on the basis of conservative estimations. These estimations were used in Section 3.2.1.1. The sources of the formulas are given wherever needed.

E.1 Radiative Heat Dissipation

The radiative heat dissipation $\dot{Q}_{\mathrm{s,rad}}$ was estimated with Eq. 2.3.2 multiplied by the sensor area A_{s}. Assumptions were $\varepsilon = 1$, $T_{\mathrm{w}} = 400\,\mathrm{K}$, and that the heated sensor area is a full disk with radius $r_{\mathrm{s,out}}$. This gives

$$\dot{Q}_{\mathrm{s,rad}} = A_{\mathrm{s}} \sigma \varepsilon \left(T_{\mathrm{w}}^4 - T_{\infty}^4 \right) \approx 5.7 \cdot 10^{-4}\,\mathrm{W}. \tag{E.1}$$

E.2 Conductive Heat Dissipation to the Substrate

The conductive heat loss to the support material $\dot{Q}_{\mathrm{s,cond\to supp}}$ was calculated with an approach based on the shape factor S. The formula is given in Bergman et al. (2011) as

$$\dot{Q}_{\mathrm{s,cond\to supp}} = k_{\mathrm{POM}} S \left(T_{\mathrm{w}} - T_{\infty} \right) \approx 5.1 \cdot 10^{-2}\,\mathrm{W}, \tag{E.2}$$

where $S = 4 r_{\mathrm{s,out}}$ and $k_{\mathrm{POM}} = 0.3\,\mathrm{W\,m^{-1}\,K^{-1}}$. Here, the heated area is assumed to be a full disk with radius $r_{\mathrm{s,out}}$.

E.3 Conductive Heat Dissipation to the Leads

The conductive heat loss to the leads $\dot{Q}_{\mathrm{s,cond\to lead}}$ was estimated with the formula defined in Bruun (1995) as

$$\dot{Q}_{\mathrm{s,cond\to lead}} = 2 k_{\mathrm{Ni}} A_{\mathrm{cross}} \frac{T_{\mathrm{w}} - T_{\infty}}{l_{\mathrm{c}}} \tanh\left(\frac{l}{2 l_{\mathrm{c}}} \right) \approx 2 \cdot 10^{-6}\,\mathrm{W}, \tag{E.3}$$

where $k_{\mathrm{Ni}} = 85\,\mathrm{W\,m^{-1}\,K^{-1}}$ and $A_{\mathrm{cross}} = \left(r_{\mathrm{s,out}} - r_{\mathrm{s,in}} \right) t_{\mathrm{s}} = 2 \cdot 10^{-11}\,\mathrm{m}$.

E.4 Natural Convective Heat Dissipation

The natural convective heat loss $\dot{Q}_{\mathrm{s,conv,free}}$ is estimated under the assumption of an isothermal vertical plate with height equal to the cavity diameter. The resulting heat transfer coefficient is then used to calculate the natural convective heat transfer from each sensor. Used formulas are taken from VDI (2010).

$$Ra \approx 3.27 \cdot 10^{9} \tag{E.4}$$

$$Pr \approx 0.73 \tag{E.5}$$

$$f_1(Pr) = \left(1 + \left(\frac{0.492}{Pr} \right)^{9/16} \right)^{-16/9} \approx 0.351 \tag{E.6}$$

$$Nu = \left(0.825 + 0.387 \left(Ra\, f_1(Pr) \right)^{1/6} \right)^2 \approx 178 \tag{E.7}$$

$$h = \frac{Nu\, k_{\mathrm{air}}}{d_{\mathrm{cav}}} \approx 95.0\,\mathrm{W\,m^{-2}\,K^{-1}} \tag{E.8}$$

$$\dot{Q}_{\mathrm{s,conv,free}} = h A_{\mathrm{s}} \left(T_{\mathrm{w}} - T_{\infty} \right) \approx 5.4 \cdot 10^{-3} \tag{E.9}$$

Here, the heated sensor area is assumed to be a full disk with radius $r_{\mathrm{s,out}}$.